

Chiral Weyl-Kondo semimetals and hexagonal heavy fermion systems

Kuan-Sen Lin^{1,†}, Yuan Fang^{1,†}, Henrique Fabrelli^{2,†}, Runhan Li^{3,4,†}, Andrey Prokofiev², Fang Xie¹, Jennifer Cano^{5,6}, Maia G. Vergniory^{3,4,7}, Silke Paschen^{2,1}, Qimiao Si^{1,*}

¹*Department of Physics and Astronomy, Extreme Quantum Materials Alliance, Smalley-Curl Institute, Rice University, Houston, Texas, 77005, USA*

²*Institute of Solid State Physics, TU Wien, Wiedner Hauptstr. 8-10, 1040 Vienna, Austria*

³*Département de Physique et Institut Quantique, Université de Sherbrooke, Sherbrooke, J1K 2R1, Québec, Canada.*

⁴*Regroupement Québécois sur les Matériaux de Pointe (RQMP), Quebec H3T 3J7, Canada*

⁵*Department of Physics and Astronomy, Stony Brook University, Stony Brook, NY 11794, USA*

⁶*Center for Computational Quantum Physics, Flatiron Institute, New York, NY 10010, USA*

⁷*Donostia International Physics Center, P. Manuel de Lardizabal 4, 20018 Donostia-San Sebastian, Spain*

Strong correlation, in concert with symmetry and topology, engenders novel gapless phases of matter, though only a tip of the iceberg has been seen. An exemplary framework is provided by Weyl-Kondo semimetals, in which Weyl fermions develop through crystalline symmetry constraints on the emergent low-energy heavy-fermion excitations. This paradigm has opened up new opportunities to explore correlated topologies without a non-interacting counterpart, but fully realizing this potential requires a large base of candidate materials. Here we confront the challenge on both fronts by studying heavy fermion systems with hexagonal space groups. This family contains a large number of chiral nonsymmorphic crystal structures that promote Weyl degeneracies and, in addition, feature geometric frustration in the f -electron magnetism. Our calculations for the heavy fermion states identify Weyl-Kondo semimetals with chiral or achiral Weyl nodes in the respective structural classes. We also develop a new search strategy for the difficult case of strongly correlated materials, using a combination of materials database, symmetry classification and experiments, and propose as candidate topological heavy fermion systems the chiral CePt₂B and achiral Ce₂NiGe₃ and Ce₆Co_{2- δ} Si₃. Our findings raise the prospect for strongly correlated metallic topology in the unusual setting of exotic quantum magnetism.

Main

In quantum materials, strong correlations agitate the electrons and, thus, enhance their physical responses^{1,2}, whereas topology protects the robustness in their properties. Accordingly, strongly correlated topological matter promises to exhibit the best features from both worlds. Topological materials with Weyl nodes in the noninteracting electron excitation spectrum are broadly referred to as Weyl semimetals^{3,4}. They can be characterized by topological invariants, *e.g.* quantized Berry phases associated with the Weyl nodes. In weakly interacting cases, Weyl semimetals have a variety of properties, including topologically-protected surface states and anomalous Hall effects that have received relatively comprehensive theoretical understandings and extensive experimental evidences³⁻⁹. By contrast, the investigation of strongly correlated metallic topology represents an outstanding challenge and is currently at the forefront in quantum materials research.

Weyl-Kondo semimetals (WKSMs) represent a class of strongly correlated gapless topological states. First advanced in the theoretical study of Kondo lattice models with nonsymmorphic symmetries¹⁰⁻¹² and, concurrently, in the experimental investigations of heavy fermion semimetals^{13,14}, WKSMs develop because space group (SG) symmetries constrain the low-energy electronic excitations pinned to the Fermi energy. Thus far, WKSMs have been studied in cubic and square-net crystals in various models^{10,11,15} as well as in candidate materials such as $\text{Ce}_3\text{Bi}_4\text{Pd}_3$ ^{13,14} and $\text{Ce}_2\text{Au}_3\text{In}_5$ ¹⁵. Because they operate in the extreme correlation regime, the landscape of WKSMs is expected to be exceedingly rich. Notwithstanding recent advances of topological semimetals lacking any noninteracting counterpart in the case of quantum critical phase¹⁶ and near a quantum critical point¹⁷, this potential remains under-tapped. One roadblock is that the material base for strongly correlated metallic topology is still small.

Here, we confront this overarching challenge by addressing heavy fermion systems with chiral crystalline structure¹⁸⁻²⁰. In chiral crystals, nonsymmorphic symmetry groups can enforce Weyl nodes²¹. Due to the absence of inversion, mirror, and roto-inversion symmetries, the Weyl and anti-Weyl points that carry opposite chiral charges in a chiral crystal generally are not located at the same energy. This makes a Weyl semimetal with a chiral crystal structure an ideal platform for certain special properties. For example, it provides one of the rare quantization in measurable properties such as circular photogalvanic effect (CPGE)²²⁻²⁶. It has been suggested that interactions, even perturbatively, have an important effect on this quantization^{27,28}. It therefore is particularly timely to study chiral Weyl semimetals in the extreme correlation regime, for which the search for material candidates becomes pivotal²⁹.

With these considerations in mind, we focus on hexagonal heavy fermion materials. The reason is the following. Among the hexagonal crystal structures [Fig. 1(a,b)] with band crossings enforced by nonsymmorphic symmetry in the presence of time-reversal symmetry and spin-orbit coupling, the majority (10 out of 13) are chiral³⁰. Furthermore, the Ce-ions in these systems often occupy lattices with geometrical frustration (see Supplementary Note 16), which promotes highly entangled quantum magnetism³¹. Specifically, in Kondo lattice models, we demonstrate chiral WKSM phases [Fig. 1(c)] in the chiral hexagonal SGs no. 173 ($P6_3$) and no. 180 ($P6_22$). As a comparison, topological Kondo semimetal phases are also advanced in several achiral hexagonal SGs. Our investigation is based on the Anderson/Kondo lattice models solved by parton saddle-point calculations. Furthermore, we have developed a search procedure for strongly correlated materials. In sharp contrast with the more familiar cases for weakly correlated compounds, the procedure combines database search, symmetry classification and *identification of experimental signatures of desired properties*. In this way, out of 282 compounds from the database, we identify several candidate nonsymmorphic hexagonal materials for the proposed correlated Kondo semimetal phases. Throughout this work, we refer to the SGs of hexagonal crystal systems as hexagonal SGs.

Hexagonal space groups Among the hexagonal SGs with nonsymmorphic band crossings³⁰, we find that SGs no. 173 ($P6_3$), no. 176 ($P6_3/m$), no. 180 ($P6_22$), and no. 190 ($P\bar{6}2c$) have relatively abundant cerium-, uranium-, and ytterbium-based compounds in the Inorganic Crystal Structure Database (ICSD) (see the Supplementary Note 11 for the statistics). Hence, our study of topological Kondo semimetals will be centered around these SGs. Specifically, SGs $P6_3$ and $P6_22$ are chiral, while SGs $P6_3/m$ and $P\bar{6}2c$ are achiral. We focus on band-crossing features of hexagonal crystal systems in the presence of time-reversal symmetry and spin-orbit coupling.

We now demonstrate the topological Kondo semimetal phases realized in the paramagnetic states of our hexagonal periodic Anderson models for the aforementioned SGs. The model details are provided in Methods and in the Supplementary Notes 1-6. The numerical details on the evaluation of topological chiral charges of Weyl points are provided in the Supplementary Note 7.

Chiral topological Kondo semimetals Due to the simpler space-group structure, we begin our demonstration of chiral WKSMs from a model calculation in the case of SG no. 173 ($P6_3$). The excitation spectrum of the hexagonal periodic Anderson model with this SG is shown in [Fig. 2(c)]. In the low-energy heavy-fermion sector, the excitations have a predominant f -electron character. Specifically, there are hourglass-type band crossings along $\Gamma - A$ and $M - L$ high-

symmetry lines [Fig. 2(e)], indicating the heavy-fermion Weyl points. In Supplementary Note 3, we show the distribution of the hourglass-type Weyl points in the Brillouin zone (BZ) [Fig. 1(b)] and their corresponding topological charges. Interestingly, the Weyl point along $\Gamma - A$ exhibits a high topological charge of $+3$ (Ref. ³²), while the Weyl point along $M - L$ has a topological charge of -1 . Furthermore, the Weyl points with topological charges $+3$ and -1 are not at the same energies as they are not related by symmetries. We hence demonstrate the chiral WKSM phase in the paramagnetic state of a system with this hexagonal SG.

In addition, since the SG describes chiral crystal structures, in the presence of time-reversal symmetry and spin-orbit coupling it could host Kramers-Weyl fermions at time-reversal-invariant momenta²¹. For example, in Fig. 2(e), at the energetically-lowest Kramers degeneracy at Γ and M there are Kramers-Weyl fermions with topological charge -1 and $+1$, respectively. In other words, the chiral WKSM phase hosts both hourglass-type Weyl points and Kramers-Weyl fermions.

The excitation spectrum of the periodic Anderson model with SG no. 180 ($P6_222$) is shown in Fig. 2(d). Along $\Gamma - A$ [Fig. 2(f)], we verify that there exist Weyl points with chiral charges of magnitude 2 (Ref. ^{30,32}). Considering all the (symmetry-related) Weyl points, the summation of the chiral charges is zero, consistent with the Nielsen-Ninomiya theorem^{33,34}.

Achiral topological Kondo semimetals We now consider the model for the achiral hexagonal SGs for comparison. Further details of the model calculations are given in Supplementary Notes 5 and 6.

The achiral hexagonal SG no. 176 $P6_3/m$ contains the screw rotation symmetry $\{C_{6z}|0, 0, 1/2\}$ and inversion symmetry \mathcal{I} . It is related to $P6_3$ by $P6_3/m = (P6_3) \cup (\mathcal{I}P6_3)$. Hence, breaking the inversion symmetry reduces $P6_3/m$ to $P6_3$. Symmetry analysis shows that there are symmetry enforced four-fold degenerate Dirac nodal lines in $P6_3/m$. These Dirac nodal lines carry quantized non-Abelian Berry phases, which give rise to non-trivial drumhead surface states according to bulk-boundary correspondence. For detailed analysis, see Supplementary Note 8 and 9.

The achiral hexagonal SG no. 190 $P\bar{6}2c$ contains the screw rotation symmetry $\{C_{6z}|0, 0, 1/3\}$ and glide symmetry $\{m_z|0, 0, 1/2\}$. There are symmetry enforced Weyl nodal lines in $P\bar{6}2c$, which is characterized by quantized Abelian Berry phase and drumhead surface states^{35,36}.

Candidate materials We next turn to the search for candidate materials. For this purpose, we develop a search procedure as illustrated in Fig. 3(a). We start with the compounds in ICSD followed by a literature search and measurements on the physical properties. The desired properties include electrical resistivity indicating non-insulating behavior; an enhanced Sommerfeld

coefficient γ determined from specific heat measurements indicating strong correlations (related to Kondo physics); and materials without magnetic transitions or low magnetic transition temperatures. In Table I we summarize the physical properties of the primary candidate materials. The details of the materials properties, as well as other candidate materials, are provided in the Supplementary Notes 12-15.

We succeeded in our search procedure for materials in the chiral SG no. 180 ($P6_222$). The primary candidate material is CePt_2B , which is reported to have a magnetic transition with a relatively low transition temperature^{37,38}. Above the magnetic transition temperature and around the characteristic temperature T_K , the paramagnetic phase of CePt_2B could realize a chiral WKSM phase with Kondo-driven Weyl points located along $\Gamma - A$, together with a second-order anomalous Hall response ($j_\mu \propto \sigma_{\mu\alpha\beta} E_\alpha E_\beta$) induced by the Berry curvature. This chiral WKSM phase also serves as a platform to investigate CPGE. If the time-reversal symmetry is broken, *e.g.* via the Zeeman effect, while the space-group symmetries of $P6_222$ are all preserved, CePt_2B would still host a second-order spontaneous Hall response induced by the Berry curvature.

For the achiral SG no. 190 ($P\bar{6}2c$), the primary candidate materials include Ce_2NiGe_3 ³⁹ and Ce_2RhSi_3 ^{40,41}, which are both reported to have a magnetic transition. Above the magnetic transition and in the paramagnetic phase, these heavy fermion compounds host Kondo-driven Weyl nodal lines on the BZ boundary, together with a fourth-order anomalous Hall response ($j_\mu \propto \sigma_{\mu\alpha\beta\gamma\delta} E_\alpha E_\beta E_\gamma E_\delta$) as the leading order response induced by the Berry curvature. On the other hand, if the time-reversal symmetry is broken, the Kondo state of Ce_2NiGe_3 and Ce_2RhSi_3 with SG no. 190 ($P\bar{6}2c$) would carry instead a Berry-curvature-induced third-order anomalous Hall effect ($j_\mu \propto \sigma_{\mu\alpha\beta\gamma} E_\alpha E_\beta E_\gamma$) as the leading order response.

Because of the reported possibility that Ce_2NiGe_3 ⁴² and Ce_2RhSi_3 ⁴³⁻⁴⁶ may crystallize in other forms, we perform new experiments on Ce_2NiGe_3 and present our results in Supplementary Note 15 and Supplementary Figs. 24–27. We confirm that Ce_2NiGe_3 has the achiral SG no. 190 ($P\bar{6}2c$), has a magnetic transition, and has a semimetallic-type resistivity. We further present new results for Ce_2NiGe_3 on the magnetoresistivity and anomalous Hall conductivity, which confirm the Kondo physics and establish that the anomalous Hall effect is dominated by the intrinsic contribution.

For the achiral SG no. 176 ($P6_3/m$), the primary candidate materials include $\text{Ce}_6\text{Rh}_{32}\text{P}_{17}$ ⁴⁷ and $\text{Ce}_6\text{Co}_{2-\delta}\text{Si}_3$ ^{48,49}. If the time-reversal symmetry is broken, the Kondo state with SG no. 176 ($P6_3/m$) would carry a first-order anomalous Hall effect ($j_\mu \propto \sigma_{\mu\alpha} E_\alpha$) as the leading order

response from the Berry curvature.

Density functional theory calculations for CePt₂B and Ce₂NiGe₃ Fig. 3(b) provides the DFT band structure of CePt₂B within an *f*-core calculation that includes the effect of spin-orbit couplings. The degeneracies and nodal lines are consistent with our symmetry analysis. Fig. 3(c) shows a zoomed-in plot of the Weyl points along $\Gamma - A$ direction and their irreducible representations, from which we determine Weyl charges for some representative Weyl points based on symmetry indicators³². The detailed analysis can be found in Supplementary Note 7. In Supplementary Note 10, we also show the DFT band structure of Ce₂NiGe₃ in SG 190 where symmetry enforced Weyl nodal lines are identified. The consistency of the *f*-core band structure with our symmetry analysis provides confidence that the heavy fermion electronic states of these materials, which develop near the Fermi energy, will feature the type of Weyl-Kondo degeneracies advanced in our model calculations.

Conclusion and outlook In this work, we identify hexagonal topological Kondo semimetals and theoretically realize chiral Weyl-Kondo semimetals. We formulate our theory in terms of periodic Anderson models, which contain a hybridization between the localized *f* electron moments and itinerant *spd* electrons together with the Coulomb repulsion for the *f* electrons. Solving for the heavy fermion state, we identify nodes of chiral Weyl semimetal types in the Kondo-driven low-energy excitations. The findings set the stage for our development of a new materials search procedure that overcomes the typical limitations for strongly correlated settings; while currently labor-intensive, the procedure is apt for further empowerment by artificial-intelligence methods. Already, with our theoretical results providing the basis, we have applied the procedure to identify a candidate chiral Weyl-Kondo semimetal CePt₂B as well as its achiral counterparts Ce₂NiGe₃ and Ce₆Co_{2- δ} Si₃. The chiral Weyl Kondo semimetals advanced here serve as a platform for novel electronic transport properties, including the spontaneous Hall response and CPGE. Furthermore, the hexagonal crystals contain magnetic correlations that are geometrically frustrated, where in the ground state the magnetic moments of the localized electrons could have extremely enhanced quantum fluctuations. Thus, our work raises the prospect to realize novel Kondo-driven topological metals in the setting of exotic quantum magnetism, thereby opening a new frontier in quantum materials research.

Methods

Periodic Anderson models We base our investigation of correlated topological semimetals on the Anderson/Kondo-lattice models. The Anderson lattice model contains n_{sub} sub-lattices per

unit cell, which could be related to each other by the nonsymmorphic operation with a fractional Bravais lattice translation. On each sub-lattice, we place spin-1/2 itinerant c electrons and localized f electrons. Hence, there are $4n_{sub}$ basis states per unit cell. We denote the fermionic annihilation and creation operators for c [f] electrons as $c_{\mathbf{R},\alpha,\sigma}$ and $c_{\mathbf{R},\alpha,\sigma}^\dagger$ [$f_{\mathbf{R},\alpha,\sigma}$ and $f_{\mathbf{R},\alpha,\sigma}^\dagger$], where \mathbf{R} indicates the unit cell (integer linear combination of \mathbf{a}_1 , \mathbf{a}_2 , and \mathbf{a}_3), α indicates the sub-lattice, and σ indicates the spin (\uparrow or \downarrow). The Hamiltonian is given by⁵⁰

$$\begin{aligned}
H = & \sum_{\mathbf{R},\mathbf{R}',\alpha,\sigma,\alpha',\sigma'} c_{\mathbf{R}'+\mathbf{R},\alpha,\sigma}^\dagger t_{(\alpha,\sigma)\leftarrow(\alpha',\sigma')}^c(\mathbf{R}) c_{\mathbf{R}',\alpha',\sigma'} \\
& + E_f \sum_{\mathbf{R},\alpha,\sigma} n_{\mathbf{R},\alpha,\sigma}^f - \mu \sum_{\mathbf{R},\alpha,\sigma} \left(n_{\mathbf{R},\alpha,\sigma}^c + n_{\mathbf{R},\alpha,\sigma}^f \right) \\
& + V \sum_{\mathbf{R},\alpha,\sigma} \left(c_{\mathbf{R},\alpha,\sigma}^\dagger f_{\mathbf{R},\alpha,\sigma} + f_{\mathbf{R},\alpha,\sigma}^\dagger c_{\mathbf{R},\alpha,\sigma} \right) \\
& + U \sum_{\mathbf{R},\alpha} n_{\mathbf{R},\alpha,\uparrow}^f n_{\mathbf{R},\alpha,\downarrow}^f, \tag{1}
\end{aligned}$$

where $n_{\mathbf{R},\alpha,\sigma}^c \equiv c_{\mathbf{R},\alpha,\sigma}^\dagger c_{\mathbf{R},\alpha,\sigma}$ and $n_{\mathbf{R},\alpha,\sigma}^f \equiv f_{\mathbf{R},\alpha,\sigma}^\dagger f_{\mathbf{R},\alpha,\sigma}$. $t_{(\alpha,\sigma)\leftarrow(\alpha',\sigma')}^c(\mathbf{R}) \in \mathbb{C}$ is the hopping strength for a c electron from sub-lattice α' with spin σ' in an arbitrary unit cell \mathbf{R}' to sub-lattice α with spin σ in the unit cell $\mathbf{R}' + \mathbf{R}$. Through the hopping strengths, the c electrons form dispersive energy bands and Bloch states. E_f is the on-site energy of the localized f electrons, which in our study will be chosen to be much lower than the energy bands of the itinerant c electrons. μ is the chemical potential which controls the total number of electrons, *i.e.* filling, of our system. Our approach highlights the role of space-group symmetry. We consider the on-site Hubbard interaction with a strength $U > 0$ for the localized f electrons. For each nonsymmorphic hexagonal SG, the parameters of H are chosen to respect the space-group symmetry as well as the spin-1/2 time-reversal symmetry. A schematic representation of our model for $n_{sub} = 2$ with sub-lattices located at $(0, 0, 0)$ and $(0, 0, 1/2)$ within the unit cell is provided in Fig. 1(d). Through the Kondo effect, the localized f moments are screened by the itinerant c electrons, inducing Kondo singlets of the form $\frac{1}{\sqrt{2}} (|\uparrow\rangle_f |\downarrow\rangle_c - |\downarrow\rangle_f |\uparrow\rangle_c)$ [Fig. 1(d)]. A demonstration of our hexagonal periodic Anderson model with the formation of Kondo singlets is shown in Fig. 1(d), which leads to a paramagnetic phase with heavy-fermion excitations. Without a loss of generality for the heavy fermion state, we obtain the excitation spectrum of this interacting Hamiltonian in the infinite- U limit using the parton saddle-point calculation by introducing an auxiliary boson field b that characterizes the valence fluctuations ($f^1 \rightleftharpoons f^0 + e^-$) of f electrons. We provide details of the numerical implementation of the parton saddle-point calculation in Supplementary Note 2⁵⁰⁻⁵³.

Density functional theory calculations In order to validate the symmetry analysis encoded in our model calculation, we performed density functional theory (DFT) calculations. First-principles calculations for CePt₂B and Ce₂NiGe₃ were carried out in the framework of the Perdew–Burke–Ernzerhof type generalized gradient approximation of the density functional theory⁵⁴. The projector augmented-wave (PAW) method was employed as implemented in the Vienna *ab initio* simulation package (VASP)^{55–58}. A plane-wave cutoff energy of 500 eV was used throughout the calculations. The BZ was sampled using a $9 \times 9 \times 4$ *k*-point mesh for CePt₂B and a $5 \times 5 \times 4$ *k*-point mesh for Ce₂NiGe₃. The irreducible representations of the electronic bands were calculated using the Irvsp program⁵⁹.

Data availability

The data that support the findings of this study are available from the corresponding author upon request.

Code availability

The computer codes that were used to generate the data that support the findings of this study are available from the corresponding author upon request.

† These authors contributed equally.

-
1. Keimer, B. & Moore, J. E. The physics of quantum materials. *Nature Physics* **13**, 1045–1055 (2017). URL <https://www.nature.com/articles/nphys4302>.
 2. Paschen, S. & Si, Q. Quantum phases driven by strong correlations. *Nature Reviews Physics* **3**, 9–26 (2021). URL <https://www.nature.com/articles/s42254-020-00262-6>.
 3. Armitage, N. P., Mele, E. J. & Vishwanath, A. Weyl and dirac semimetals in three-dimensional solids. *Rev. Mod. Phys.* **90**, 015001 (2018). URL <https://link.aps.org/doi/10.1103/RevModPhys.90.015001>.
 4. Hu, J., Xu, S.-Y., Ni, N. & Mao, Z. Transport of topological semimetals. *Annual Review of Materials Research* **49**, 207–252 (2019). URL <https://www.annualreviews.org/content/journals/10.1146/annurev-matsci-070218-010023>.
 5. Cano, J. & Bradlyn, B. Band representations and topological quantum chemistry. *Annu. Rev. Condens.*

- Matter Phys.* **12**, 225–246 (2021).
6. Son, D. T. & Spivak, B. Z. Chiral anomaly and classical negative magnetoresistance of weyl metals. *Phys. Rev. B* **88**, 104412 (2013). URL <https://link.aps.org/doi/10.1103/PhysRevB.88.104412>.
 7. Hosur, P. & Qi, X. Recent developments in transport phenomena in weyl semimetals. *Comptes Rendus Physique* **14**, 857–870 (2013). URL <https://www.sciencedirect.com/science/article/pii/S1631070513001710>. Topological insulators / Isolants topologiques.
 8. Zyuzin, A. A. & Burkov, A. A. Topological response in weyl semimetals and the chiral anomaly. *Phys. Rev. B* **86**, 115133 (2012). URL <https://link.aps.org/doi/10.1103/PhysRevB.86.115133>.
 9. Huang, Z.-M., Zhou, J. & Shen, S.-Q. Topological responses from chiral anomaly in multi-weyl semimetals. *Phys. Rev. B* **96**, 085201 (2017). URL <https://link.aps.org/doi/10.1103/PhysRevB.96.085201>.
 10. Lai, H.-H., Grefe, S. E., Paschen, S. & Si, Q. Weyl-kondo semimetal in heavy-fermion systems. *Proceedings of the National Academy of Sciences* **115**, 93–97 (2018). URL <https://www.pnas.org/doi/abs/10.1073/pnas.1715851115>. <https://www.pnas.org/doi/pdf/10.1073/pnas.1715851115>.
 11. Grefe, S. E., Lai, H.-H., Paschen, S. & Si, Q. Weyl-kondo semimetals in nonsymmorphic systems. *Phys. Rev. B* **101**, 075138 (2020). URL <https://link.aps.org/doi/10.1103/PhysRevB.101.075138>.
 12. Fang, Y., Chen, L., Prokofiev, A., Robredo, I., Cano, J., Vergniory, M. G., Paschen, S. & Si, Q. Magnetic weyl-kondo semimetals induced by quantum fluctuations (2024). URL <https://arxiv.org/abs/2403.02295>. 2403.02295.
 13. Dzsaber, S., Prochaska, L., Sidorenko, A., Eguchi, G., Svagera, R., Waas, M., Prokofiev, A., Si, Q. & Paschen, S. Kondo insulator to semimetal transformation tuned by spin-orbit coupling. *Phys. Rev. Lett.* **118**, 246601 (2017). URL <https://link.aps.org/doi/10.1103/PhysRevLett.118.246601>.
 14. Dzsaber, S., Yan, X., Taupin, M., Eguchi, G., Prokofiev, A., Shiroka, T., Blaha, P., Rubel, O., Grefe, S. E., Lai, H.-H., Si, Q. & Paschen, S. Giant spontaneous hall effect in a nonmagnetic weyl-kondo semimetal. *Proceedings of the National Academy of Sciences* **118**, e2013386118 (2021). URL <https://www.pnas.org/doi/abs/10.1073/pnas>.

2013386118. <https://www.pnas.org/doi/pdf/10.1073/pnas.2013386118>.
15. Chen, L., Setty, C., Hu, H., Vergniory, M. G., Grefe, S. E., Fischer, L., Yan, X., Eguchi, G., Prokofiev, A., Paschen, S., Cano, J. & Si, Q. Topological semimetal driven by strong correlations and crystalline symmetry. *Nature Physics* **18**, 1341–1346 (2022). URL <https://doi.org/10.1038/s41567-022-01743-4>.
 16. Hu, H., Chen, L., Setty, C., Garcia-Diez, M., Grefe, S. E., Prokofiev, A., Kirchner, S., Vergniory, M. G., Paschen, S., Cano, J. & Si, Q. Topological semimetals without quasiparticles. *arXiv e-prints arXiv:2110.06182* (2021). 2110.06182.
 17. Kirschbaum, D. M., Chen, L., Zocco, D. A., Hu, H., Mazza, F., Karlich, M., Lužnik, M., Nguyen, D. H., Larrea Jiménez, J., Strydom, A. M., Adroja, D., Yan, X., Prokofiev, A., Si, Q. & Paschen, S. Emergent topological semimetal from quantum criticality. *Nature Physics* **22**, 218–224 (2026). URL <https://doi.org/10.1038/s41567-025-03135-w>.
 18. Flack, H. D. Chiral and achiral crystal structures. *Helvetica Chimica Acta* **86**, 905–921 (2003). URL <https://onlinelibrary.wiley.com/doi/abs/10.1002/hlca.200390109>. <https://onlinelibrary.wiley.com/doi/pdf/10.1002/hlca.200390109>.
 19. Fecher, G. H., Kübler, J. & Felser, C. Chirality in the solid state: Chiral crystal structures in chiral and achiral space groups. *Materials* **15** (2022). URL <https://www.mdpi.com/1996-1944/15/17/5812>.
 20. Wang, X., Yi, C. & Felser, C. Chiral quantum materials: When chemistry meets physics. *Advanced Materials* **36**, 2308746 (2024). URL <https://advanced.onlinelibrary.wiley.com/doi/abs/10.1002/adma.202308746>. <https://advanced.onlinelibrary.wiley.com/doi/pdf/10.1002/adma.202308746>.
 21. Chang, G., Wieder, B. J., Schindler, F., Sanchez, D. S., Belopolski, I., Huang, S.-M., Singh, B., Wu, D., Chang, T.-R., Neupert, T., Xu, S.-Y., Lin, H. & Hasan, M. Z. Topological quantum properties of chiral crystals. *Nature Materials* **17**, 978–985 (2018). URL <https://doi.org/10.1038/s41563-018-0169-3>.
 22. de Juan, F., Grushin, A. G., Morimoto, T. & Moore, J. E. Quantized circular photogalvanic effect in weyl semimetals. *Nature Communications* **8**, 15995 (2017). URL <https://doi.org/10.1038/ncomms15995>.
 23. Vazifeh, M. M. & Franz, M. Electromagnetic response of weyl semimetals. *Phys. Rev. Lett.* **111**, 027201 (2013). URL <https://link.aps.org/doi/10.1103/PhysRevLett.111.027201>.

027201.

24. Sipe, J. E. & Shkrebtii, A. I. Second-order optical response in semiconductors. *Phys. Rev. B* **61**, 5337–5352 (2000). URL <https://link.aps.org/doi/10.1103/PhysRevB.61.5337>.
25. Golub, L. E., Ivchenko, E. L. & Spivak, B. Semiclassical theory of the circular photogalvanic effect in gyrotropic systems. *Phys. Rev. B* **102**, 085202 (2020). URL <https://link.aps.org/doi/10.1103/PhysRevB.102.085202>.
26. Morimoto, T. & Nagaosa, N. Topological nature of nonlinear optical effects in solids. *Science Advances* **2**, e1501524 (2016). URL <https://www.science.org/doi/abs/10.1126/sciadv.1501524>. <https://www.science.org/doi/pdf/10.1126/sciadv.1501524>.
27. Avdoshkin, A., Kozii, V. & Moore, J. E. Interactions remove the quantization of the chiral photocurrent at weyl points. *Phys. Rev. Lett.* **124**, 196603 (2020). URL <https://link.aps.org/doi/10.1103/PhysRevLett.124.196603>.
28. Wu, A.-K., Guerci, D., Fu, Y., Wilson, J. H. & Pixley, J. H. Absence of quantization in the circular photogalvanic effect in disordered chiral weyl semimetals. *Phys. Rev. B* **110**, 014201 (2024). URL <https://link.aps.org/doi/10.1103/PhysRevB.110.014201>.
29. Iwasa, K., Suyama, K., Ohira-Kawamura, S., Nakajima, K., Raymond, S., Steffens, P., Yamada, A., Matsuda, T. D., Aoki, Y., Kawasaki, I., Fujimori, S.-i., Yamagami, H. & Yokoyama, M. Weyl–kondo semimetal behavior in the chiral structure phase of $\text{Ce}_3\text{Rh}_4\text{Sn}_{13}$. *Phys. Rev. Mater.* **7**, 014201 (2023). URL <https://link.aps.org/doi/10.1103/PhysRevMaterials.7.014201>.
30. Zhang, J., Chan, Y.-H., Chiu, C.-K., Vergniory, M. G., Schoop, L. M. & Schnyder, A. P. Topological band crossings in hexagonal materials. *Phys. Rev. Mater.* **2**, 074201 (2018). URL <https://link.aps.org/doi/10.1103/PhysRevMaterials.2.074201>.
31. Broholm, C., Cava, R. J., Kivelson, S. A., Nocera, D. G., Norman, M. R. & Senthil, T. Quantum spin liquids. *Science* **367**, eaay0668 (2020). URL <https://www.science.org/doi/abs/10.1126/science.aay0668>. <https://www.science.org/doi/pdf/10.1126/science.aay0668>.
32. Tsirkin, S. S., Souza, I. & Vanderbilt, D. Composite weyl nodes stabilized by screw symmetry with and without time-reversal invariance. *Phys. Rev. B* **96**, 045102 (2017). URL <https://link.aps.org/doi/10.1103/PhysRevB.96.045102>.
33. Nielsen, H. B. & Ninomiya, M. Absence of neutrinos on a lattice:(i). proof by homotopy theory. *Nuclear Physics B* **185**, 20–40 (1981). URL [https://doi.org/10.1016/0550-3213\(81\)90361-8](https://doi.org/10.1016/0550-3213(81)90361-8).

34. Nielsen, H. B. & Ninomiya, M. Absence of neutrinos on a lattice:(ii). intuitive topological proof. *Nuclear Physics B* **193**, 173–194 (1981). URL [https://doi.org/10.1016/0550-3213\(81\)90524-1](https://doi.org/10.1016/0550-3213(81)90524-1).
35. Chan, Y.-H., Chiu, C.-K., Chou, M. Y. & Schnyder, A. P. ca_3p_2 and other topological semimetals with line nodes and drumhead surface states. *Phys. Rev. B* **93**, 205132 (2016). URL <https://link.aps.org/doi/10.1103/PhysRevB.93.205132>.
36. Muechler, L., Topp, A., Queiroz, R., Krivenkov, M., Varykhalov, A., Cano, J., Ast, C. R. & Schoop, L. M. Modular arithmetic with nodal lines: Drumhead surface states in zr_2si_2 . *Phys. Rev. X* **10**, 011026 (2020). URL <https://link.aps.org/doi/10.1103/PhysRevX.10.011026>.
37. Sologub, O., Salamakha, P., Noël, H., Potel, M., Almeida, M. & Godart, C. New structure type of ternary intermetallic borides ce_2b . *Journal of Alloys and Compounds* **307**, 40–44 (2000). URL <https://www.sciencedirect.com/science/article/pii/S0925838800008252>.
38. Lackner, R., Sieberer, M., Michor, H., Hilscher, G., Bauer, E., Salamakha, P. S., Sologub, O. L. & Hiebl, K. Low temperature properties of the ternary compounds ce_2b and ce_3b . *Journal of Physics: Condensed Matter* **17**, S905 (2005). URL <https://doi.org/10.1088/0953-8984/17/11/022>.
39. Kalsi, D., Rayaprol, S., Siruguri, V. & Peter, S. C. Neutron diffraction studies on structural and magnetic properties of re_2nig_3 ($re=la, ce$). *Journal of Solid State Chemistry* **217**, 113–119 (2014). URL <https://www.sciencedirect.com/science/article/pii/S0022459614002266>.
40. Szytuła, A., Leciejewicz, J. & Małetka, K. Neutron diffraction study of ce_2rhsi_3 , nd_2rhsi_3 and tb_2rhsi_3 . *Journal of Magnetism and Magnetic Materials* **118**, 302–306 (1993). URL <https://www.sciencedirect.com/science/article/pii/030488539390430A>.
41. Leciejewicz, J., Stüsser, N., Szytuła, A. & Zygmunt, A. Antiferromagnetic ordering in ce_2rhsi_3 . *Journal of Magnetism and Magnetic Materials* **147**, 45–48 (1995). URL <https://www.sciencedirect.com/science/article/pii/0304885394017026>.
42. Huo, D., Sakurai, J., Kuwai, T., Isikawa, Y. & Lu, Q. Electric, magnetic, and thermal properties of ce_2nig_3 : a kondo lattice compound showing spin glass behavior. *Phys. Rev. B* **64**, 224405 (2001). URL <https://link.aps.org/doi/10.1103/PhysRevB.64.224405>.
43. Chevalier, B., Lejay, P., Etourneau, J. & Hagenmuller, P. A new family of rare earth compounds,

- the ternary silicides re_2rhsi_3 (re = y, la, ce, nd, sm, gd, tb, dy, ho, er) - crystal structure electrical and magnetic properties. *Solid State Communications* **49**, 753–760 (1984). URL <https://www.sciencedirect.com/science/article/pii/0038109884900735>.
44. Das, I. & Sampathkumaran, E. Magnetic ordering in ce_2rhsi_3 . *Journal of Magnetism and Magnetic Materials* **137**, L239–L242 (1994). URL <https://www.sciencedirect.com/science/article/pii/0304885394907072>.
45. Kase, N., Muranaka, T. & Akimitsu, J. Antiferromagnetic kondo-lattice system ce_2rhsi_3 with moderate heavy-fermion behavior. *Journal of Magnetism and Magnetic Materials* **321**, 3380–3383 (2009). URL <https://www.sciencedirect.com/science/article/pii/S0304885309006416>.
46. Szlawska, M., Kaczorowski, D., Ślebarski, A., Gulay, L. & Stępień-Damm, J. Antiferromagnetic order and kondo-lattice behavior in single-crystalline ce_2rhsi_3 . *Phys. Rev. B* **79**, 134435 (2009). URL <https://link.aps.org/doi/10.1103/PhysRevB.79.134435>.
47. Pivan, J.-Y., Guérin, R., Pena, O., Padiou, J. & Sergent, M. Crystal structures and properties of new rare earth rhodium phosphides : $\text{La}_6\text{rh}_{32}\text{p}_{17}$ and $\text{ce}_6\text{rh}_{32}\text{p}_{17}$. *Materials Research Bulletin* **23**, 513–520 (1988). URL <https://www.sciencedirect.com/science/article/pii/0025540888901596>.
48. Gaudin, E. & Chevalier, B. On the structural and magnetic properties of the ternary silicides $\text{ce}_6\text{m}_{1.67}\text{si}_3$ (m=co, ni) and $\text{ce}_5\text{ni}_{1.85}\text{si}_3$. *Journal of Solid State Chemistry* **180**, 1397–1409 (2007). URL <https://www.sciencedirect.com/science/article/pii/S0022459607000631>.
49. Chevalier, B., Gaudin, E. & Weill, F. The new ternary silicides $\text{re}_6\text{co}_{1.67}\text{si}_3$ (re=ce, nd, gd, tb, dy) investigated by x-ray diffraction and magnetization measurements. *Journal of Alloys and Compounds* **442**, 149–151 (2007). URL <https://www.sciencedirect.com/science/article/pii/S0925838807002599>. Proceedings of the 15th International Conference on Solid Compounds of Transition Elements.
50. Hewson, A. C. *The Kondo problem to heavy fermions* (Cambridge university press, 1997). URL <https://doi.org/10.1017/CBO9780511470752>.
51. Coh, S. & Vanderbilt, D. Python tight binding (pythtb) (2022). URL <https://doi.org/10.5281/zenodo.12721316>.
52. Po, H. C., Vishwanath, A. & Watanabe, H. Symmetry-based indicators of band topology in the

- 230 space groups. *Nature Communications* **8**, 50 (2017). URL <https://doi.org/10.1038/s41467-017-00133-2>.
53. Bradlyn, B., Wang, Z., Cano, J. & Bernevig, B. A. Disconnected elementary band representations, fragile topology, and wilson loops as topological indices: An example on the triangular lattice. *Phys. Rev. B* **99**, 045140 (2019). URL <https://link.aps.org/doi/10.1103/PhysRevB.99.045140>.
54. Perdew, J. P., Burke, K. & Ernzerhof, M. Generalized gradient approximation made simple. *Phys. Rev. Lett.* **77**, 3865–3868 (1996).
55. Kresse, G. & Hafner, J. Ab initio molecular dynamics for liquid metals. *Phys. Rev. B* **47**, 558–561 (1993).
56. Kresse, G. & Furthmüller, J. Efficiency of ab-initio total energy calculations for metals and semiconductors using a plane-wave basis set. *Comput. Mater. Sci.* **6**, 15–50 (1996).
57. Kresse, G. & Furthmüller, J. Efficient iterative schemes for ab initio total-energy calculations using a plane-wave basis set. *Phys. Rev. B* **54**, 11169–11186 (1996).
58. Kresse, G. & Joubert, D. From ultrasoft pseudopotentials to the projector augmented-wave method. *Phys. Rev. B* **59**, 1758–1775 (1999).
59. Gao, J., Wu, Q., Persson, C. & Wang, Z. Irvsp: To obtain irreducible representations of electronic states in the VASP. *Comput. Phys. Commun.* **261**, 107760 (2021).
60. Mugiraneza, S. & Hallas, A. M. Tutorial: a beginner’s guide to interpreting magnetic susceptibility data with the curie-weiss law. *Communications Physics* **5**, 95 (2022). URL <https://doi.org/10.1038/s42005-022-00853-y>.
61. Schlottmann, P. Bethe-ansatz solution of the ground-state of the su (2j+1) kondo (coqblin-schrieffer) model: Magnetization, magnetoresistance and universality. *Zeitschrift für Physik B Condensed Matter* **51**, 223–235 (1983). URL <https://doi.org/10.1007/BF01307678>.
62. Lee, B. K., Ryu, D. H., Kim, D. Y., Hong, J. B., Jung, M. H., Kitazawa, H., Suzuki, O., Kimura, S. & Kwon, Y. S. Magnetic ordering in frustrated $\text{ce}_5\text{ni}_2\text{si}_3$. *Phys. Rev. B* **70**, 224409 (2004). URL <https://link.aps.org/doi/10.1103/PhysRevB.70.224409>.
63. Ryu, D., Jung, M. & Kwon, Y. Magnetic ordering in frustrated $\text{ce}_5\text{ni}_2\text{si}_3$. *Physica B: Condensed Matter* **359-361**, 305–307 (2005). URL <https://www.sciencedirect.com/science/article/pii/S0921452605001201>. Proceedings of the International Conference on Strongly Correlated Electron Systems.

64. Babizhetskyy, V., Le Sénéchal, C., Guérin, R., Isnard, O. & Hiebl, K. Ternary rare-earth nickel arsenides of $\text{sm}_{20}\text{ni}_{42}\text{p}_{31}$ -type structure: Structural chemistry and physical properties. *Phys. Rev. B* **66**, 014102 (2002). URL <https://link.aps.org/doi/10.1103/PhysRevB.66.014102>.
65. Babizhetskyy, V., Weitzer, F. & Hiebl, K. Structural chemistry, magnetic and electrical properties of ternary rare-earth nickel phosphides, $\text{r}_{20}\text{ni}_{42}\text{p}_{30}$ ($\text{r}=\text{ce}$, sm). *Journal of Alloys and Compounds* **317-318**, 250–253 (2001). URL <https://www.sciencedirect.com/science/article/pii/S0925838800013426>. The 13th International Conference on Solid Compounds of Transition Elements.
66. Babizhetskyy, V., Isnard, O. & Hiebl, K. Intermediate valence behaviour of the ternary cerium–nickel–phosphide $\text{ce}_{20}\text{ni}_{42}\text{p}_{30}$. *Physica B: Condensed Matter* **352**, 42–47 (2004). URL <https://www.sciencedirect.com/science/article/pii/S0921452604007446>.
67. Gulay, L. & Olekseyuk, I. Crystal structures of the $\text{r}_3\text{cusnse}_7$ ($\text{r} = \text{la}$, ce , pr , nd , sm , gd , tb and dy) compounds. *Journal of Alloys and Compounds* **388**, 274–278 (2005). URL <https://www.sciencedirect.com/science/article/pii/S0925838804009636>.
68. Gulay, L., Kaczorowski, D. & Pietraszko, A. Crystal structure and magnetic properties of $\text{ce}_3\text{cusnse}_7$. *Journal of Alloys and Compounds* **403**, 49–52 (2005). URL <https://www.sciencedirect.com/science/article/pii/S0925838805010558>.
69. Daszkiewicz, M., Strok, O., Gulay, L. & Kaczorowski, D. Crystal structure of $\text{r}_3\text{ge}_1+\text{xse}_7$ ($\text{r}=\text{la}$, ce , pr , sm , gd and tb , $\text{x}=0.43\text{--}0.49$) and magnetic properties of $\text{ce}_3\text{ge}_1.47\text{se}_7$. *Journal of Alloys and Compounds* **508**, 258–261 (2010). URL <https://www.sciencedirect.com/science/article/pii/S0925838810021171>.
70. King, A. A., Breton, L. S., Morrison, G., Smith, M. D., Liang, M., Halasyamani, P. S. & zur Loye, H.-C. Crystal structures and property measurements of rare earth magnesium thiosilicates synthesized via flux crystal growth utilizing the boron chalcogen mixture (bcm) method. *Inorganic Chemistry* **62**, 7446–7452 (2023). URL <https://doi.org/10.1021/acs.inorgchem.3c00708>. PMID: 37137155, <https://doi.org/10.1021/acs.inorgchem.3c00708>.
71. Abeysinghe, D., Smith, M. D., Yeon, J., Tran, T. T., Paria Sena, R., Hadermann, J., Halasyamani, P. S. & zur Loye, H.-C. Crystal growth and structure analysis of $\text{ce}_{18}\text{w}_{10}\text{o}_{57}$: A complex oxide containing tungsten in an unusual trigonal prismatic coordination environment. *Inorganic Chemistry* **56**, 2566–2575 (2017). URL <https://doi.org/10.1021/acs.inorgchem.6b02710>. PMID:

- 28199086, <https://doi.org/10.1021/acs.inorgchem.6b02710>.
72. Daoudi, A., Lamire, M., Levet, J. & Noël, H. New ternary uranium copper chalcogenides $\text{Cu}_2\text{U}_3\text{S}_7$ and $\text{Cu}_2\text{U}_3\text{Se}_7$: Crystal structure and magnetic properties. *Journal of Solid State Chemistry* **123**, 331–336 (1996). URL <https://www.sciencedirect.com/science/article/pii/S0022459696901887>.
73. Troć, R., Kaczorowski, D., Noël, H. & Le Bihan, T. Crystal structure of $\text{U}_6\text{Ni}_{20}\text{P}_{13}$ and $\text{U}_6\text{Ni}_{20}\text{As}_{13}$. *Journal of Alloys and Compounds* **184**, L27–L31 (1992). URL <https://www.sciencedirect.com/science/article/pii/092583889290492R>.
74. Ebel, T., Albering, J. H. & Jeitschko, W. Preparation, crystal structure and magnetic properties of the uranium nickel phosphides $\text{U}_3\text{Ni}_2\text{P}$, $\text{U}_4\text{Ni}_2\text{P}$, $\text{U}_6\text{Ni}_{20}\text{P}_{13}$ and $\text{U}_2\text{Ni}_{12}\text{P}_7$. *Journal of Alloys and Compounds* **266**, 71–76 (1998). URL <https://www.sciencedirect.com/science/article/pii/S0925838897005136>.
75. Breeze, E. & Brett, N. The crystal structure of U_7Te_{12} and $\text{U}_2\text{O}_2\text{Te}$. *Journal of Nuclear Materials* **40**, 113–115 (1971). URL <https://www.sciencedirect.com/science/article/pii/002231157190122X>.
76. Breeze, E., Brett, N. & White, J. An investigation of solid state relationships in the system $\text{U}-\text{Te}-\text{C}$. *Journal of Nuclear Materials* **39**, 157–165 (1971). URL <https://www.sciencedirect.com/science/article/pii/0022311571900201>.
77. Suski, W. Magnetic properties of U_2Te and U_7Te_{12} . *physica status solidi (a)* **13**, 675–680 (1972). URL <https://onlinelibrary.wiley.com/doi/abs/10.1002/pssa.2210130241>. <https://onlinelibrary.wiley.com/doi/pdf/10.1002/pssa.2210130241>.
78. Tougait, O., Potel, M. & Noël, H. Characterization of the binary uranium and thorium tellurides U_7Te_{12} and $\text{Th}_7\text{Te}_{12}$. *Inorganic Chemistry* **37**, 5088–5091 (1998). URL <https://doi.org/10.1021/ic9802808>. <https://doi.org/10.1021/ic9802808>.
79. Opletal, P., Sakai, H., Haga, Y., Tokiwa, Y., Yamamoto, E., Kambe, S. & Tokunaga, Y. Ferromagnetic crossover within the ferromagnetic order of U_7Te_{12} . *Journal of the Physical Society of Japan* **92**, 034704 (2023). URL <https://doi.org/10.7566/JPSJ.92.034704>. <https://doi.org/10.7566/JPSJ.92.034704>.
80. Khatua, J., Pregelj, M., Elghandour, A., Jagličić, Z., Klingeler, R., Zorko, A. & Khuntia, P. Magnetic properties of the triangular-lattice antiferromagnets $\text{Ba}_3\text{RB}_9\text{O}_{18}$ ($r = \text{Yb}, \text{Er}$). *Phys. Rev. B* **106**, 104408 (2022). URL <https://link.aps.org/doi/10.1103/PhysRevB.106.104408>.

81. Somesh, K., Islam, S. S., Mohanty, S., Simutis, G., Guguchia, Z., Wang, C., Sichelschmidt, J., Baenitz, M. & Nath, R. Absence of magnetic order and emergence of unconventional fluctuations in the $J_{\text{eff}} = \frac{1}{2}$ triangular-lattice antiferromagnet YbBO_3 . *Phys. Rev. B* **107**, 064421 (2023). URL <https://link.aps.org/doi/10.1103/PhysRevB.107.064421>.
82. Nagaosa, N., Sinova, J., Onoda, S., MacDonald, A. H. & Ong, N. P. Anomalous Hall effect. *Rev. Mod. Phys.* **82**, 1539–1592 (2010). URL <https://link.aps.org/doi/10.1103/RevModPhys.82.1539>.
83. Lee, W.-L., Watauchi, S., Miller, V. L., Cava, R. J. & Ong, N. P. Dissipationless anomalous Hall current in the ferromagnetic spinel $\text{CuCr}_2\text{Se}_{4-x}\text{Br}_x$. *Sci.* **303**, 1647–1649 (2004). URL <https://www.science.org/doi/abs/10.1126/science.1094383>.
84. Suzuki, T., Chisnell, R., Devarakonda, A., Liu, Y.-T., Feng, W., Xiao, D., Lynn, J. W. & Checkelsky, J. G. Large anomalous Hall effect in a half-Heusler antiferromagnet. *Nat. Phys.* **12**, 1119–1123 (2016). URL <https://doi.org/10.1038/nphys3831>.
85. Takahashi, K. S., Ishizuka, H., Murata, T., Wang, Q. Y., Tokura, Y., Nagaosa, N. & Kawasaki, M. Anomalous Hall effect derived from multiple Weyl nodes in high-mobility EuTiO_3 films. *Sci. Adv.* **4**, eaar7880 (2018). URL <https://www.science.org/doi/abs/10.1126/sciadv.aar7880>.
86. Liu, E., Sun, Y., Kumar, N., Muechler, L., Sun, A., Jiao, L., Yang, S.-Y., Liu, D., Liang, A., Xu, Q., Kroder, J., Süß, V., Borrmann, H., Shekhar, C., Wang, Z., Xi, C., Wang, W., Schnelle, W., Wirth, S., Chen, Y., Goennenwein, S. T. B. & Felser, C. Giant anomalous Hall effect in a ferromagnetic kagome-lattice semimetal. *Nat. Phys.* **14**, 1125–1131 (2018). URL <https://doi.org/10.1038/s41567-018-0234-5>.
87. Miyasato, T., Abe, N., Fujii, T., Asamitsu, A., Onoda, S., Onose, Y., Nagaosa, N. & Tokura, Y. Crossover behavior of the anomalous Hall effect and anomalous Nernst effect in itinerant ferromagnets. *Phys. Rev. Lett.* **99**, 086602 (2007). URL <https://doi.org/10.1103/PhysRevLett.99.086602>.
88. Fujishiro, Y., Kanazawa, N., Kurihara, R., Ishizuka, H., Hori, T., Yasin, F. S., Yu, X., Tsukazaki, A., Ichikawa, M., Kawasaki, M., Nagaosa, N., Tokunaga, M. & Tokura, Y. Giant anomalous Hall effect from spin-chirality scattering in a chiral magnet. *Nat. Commun.* **12**, 317 (2021). URL <https://doi.org/10.1038/s41467-020-20384-w>.
89. Yu, Z., You, H., Luo, X., Han, Y., Zhong, R., Luo, Q., Yang, H., Wu, H., Chen, C., Fang, C., Ren,

- W. & Ma, S. Large anomalous Hall effect induced by skew scattering in the hexagonal ferromagnet PrCrGe₃. *Phys. Rev. B* **111**, 125112 (2025). URL <https://doi.org/10.1103/PhysRevB.111.125112>.
90. Chen, J., Yang, X., Zhou, F., Lau, Y.-C., Feng, W., Yao, Y., Li, Y., Jiang, Y. & Wang, W. Colossal anomalous Hall effect in the layered antiferromagnetic EuAl₂Si₂ compound. *Mater. Horiz.* **11**, 4665–4673 (2024). URL <https://doi.org/10.1039/D4MH00480A>.
91. Yang, S.-Y., Wang, Y., Ortiz, B. R., Liu, D., Gayles, J., Derunova, E., Gonzalez-Hernandez, R., Šmejkal, L., Chen, Y., Parkin, S. S. P., Wilson, S. D., Toberer, E. S., McQueen, T. & Ali, M. N. Giant, unconventional anomalous Hall effect in the metallic frustrated magnet candidate, KV₃Sb₅. *Sci. Adv.* **6**, eabb6003 (2020). URL <https://www.science.org/doi/10.1126/sciadv.abb6003>.
92. Assoud, A., Sankar, C. R. & Kleinke, H. Synthesis, crystal structure, electronic structure and electrical conductivity of La₃GeSb_{0.31}Se₇ and La₃SnFe_{0.61}Se₇. *Solid State Sci.* **38**, 124–128 (2014).
93. Pramanik, M. & Islam, D. The Mott $T^{-1/4}$ law from the rate equation formalism. *J. Non-Cryst. Solids* **45**, 325–333 (1981). URL <https://www.sciencedirect.com/science/article/pii/0022309381900533>.
94. Nguyen, V. L. & Dang, D.-T. Variable range hopping in finite one-dimensional and anisotropic two-dimensional systems. *Phys. B Condens. Matter* **334**, 88–97 (2003). URL <https://www.sciencedirect.com/science/article/pii/S0921452603000218>.
95. Essaleh, L., Wasim, S. M., Marín, G., Rincón, C., Amhil, S. & Galibert, J. Mott type variable range hopping conduction and magnetoresistance in p-type CuIn₃Te₅ semiconductor compound. *J. Appl. Phys.* **122**, 015702 (2017). URL <https://doi.org/10.1063/1.4991004>.
96. Daszkiewicz, M., Gulay, L., Lychmanyuk, O. & Pietraszko, A. Crystal structures of the R₃Ag_{1-δ}TSe₇ (R=La–Nd, Sm, Gd–Dy, δ=0–0.30; T=Ge, Si) compounds. *J. Alloys Compd.* **467**, 168–172 (2009).
97. Iyer, A. K., Yin, W., Rudyk, B. W., Lin, X., Nilges, T. & Mar, A. Metal ion displacements in noncentrosymmetric chalcogenides La₃Ga_{1.67}S₇, La₃Ag_{0.6}GaCh₇ (Ch=S, Se), and La₃MGaSe₇ (M=Zn, Cd). *J. Solid State Chem.* **243**, 221–231 (2016).
98. Iyer, A. K., Yin, W., Lee, E. J., Bernard, G. M., Michaelis, V. K. & Mar, A. Quaternary chalcogenides La₃Sn_{0.5}InS₇ and La₃Sn_{0.5}InSe₇. *Z. Anorg. Allg. Chem.* **643**, 1867–1873 (2017).
99. Guo, S., Guo, G. & Huang, J. Syntheses, structures and properties of five chiral quaternary sulfides,

- $\text{Al}_x\text{Ln}_3(\text{Si}_y\text{Al}_{1-y})\text{S}_7$ ($\text{Ln} = \text{Y, Gd, Dy}$) and $\text{In}_{0.33}\text{Sm}_3\text{SiS}_7$. *Sci. China, Ser. B: Chem.* **52**, 1609–1615 (2009).
100. Daszkiewicz, M., Gulay, L., Pietraszko, A. & Shemet, V. Crystal structures of the $\text{La}_3\text{AgSnSe}_7$ and $R_3\text{Ag}_{1-\delta}\text{SnS}_7$ ($R=\text{La, Ce}$; $\delta=0.18-0.19$) compounds. *J. Solid State Chem.* **180**, 2053–2060 (2007).
101. Akopov, G., Hewage, N. W., Yox, P., Viswanathan, G., Lee, S. J., Hulsebosch, L. P., Cady, S. D., Paterson, A. L., Perras, F. A., Xu, W., Wu, K., Mudryk, Y. & Kovnir, K. Synthesis-enabled exploration of chiral and polar multivalent quaternary sulfides. *Chem. Sci.* **12**, 14718–14730 (2021).

Acknowledgment: We thank Mounica Mahankali, Shouvik Sur, Eric Bauer, Lei Chen, Adolfo Grushin, and Joel Moore for useful discussions. Work at Rice has been supported by the National Science Foundation under Grant No. DMR-2220603 (K.-S.L., Y.F. and F.X.), and by the Robert A. Welch Foundation Grant No. C-1411 and the Vannevar Bush Faculty Fellowship ONR-VB N00014-23-1-2870 (Q.S.). K.-S.L. acknowledges the Carl and Lillian Illig Postdoctoral Fellowship from the Smalley-Curl Institute at Rice University. The majority of the computational calculations have been performed on the Shared University Grid at Rice funded by NSF under Grant EIA-0216467, a partnership between Rice University, Sun Microsystems, and Sigma Solutions, Inc., the Big-Data Private-Cloud Research Cyberinfrastructure MRI-award funded by NSF under Grant No. CNS-1338099, and the Extreme Science and Engineering Discovery Environment (XSEDE) by NSF under Grant No. DMR170109. H.F., A.P. and S.P. acknowledge funding by the European Union (ERC, CorMeTop, project 101055088). R. L. and M.G.V. acknowledge support to the Spanish Ministerio de Ciencia e Innovacion (grant PID2022-142008NB-I00), partial support from European Research Council (ERC) grant agreement no. 101020833 and the European Union NextGenerationEU/PRTR-C17.I1, as well as by the IKUR Strategy under the collaboration agreement between Ikerbasque Foundation and DIPC on behalf of the Department of Education of the Basque Government and the Ministry for Digital Transformation and of Civil Service of the Spanish Government through the QUANTUM ENIA project call - Quantum Spain project, and by the European Union through the Recovery, Transformation and Resilience Plan - NextGenerationEU within the framework of the Digital Spain 2026 Agenda. M.G.V. and S.P. acknowledge funding from the Deutsche Forschungsgemeinschaft (DFG, German Research Foundation) and the Austrian Science Fund (FWF) through the project FOR 5249 (QUAST). M.G.V. received financial support from the Canada Excellence Research Chairs Program for Topological Quantum Materials. J.C. acknowledges the support of the National Science Foundation under Grant No. DMR-1942447, support from the Alfred P. Sloan Foundation through a Sloan Research Fellowship and the support of the Flatiron Institute, a division of the Simons Foundation. J.C. and Q.S. acknowledge the hospitality of the Aspen Center for Physics, which is supported by the National Science Foundation under Grant No. PHY-2210452.

Author contributions

Q.S. and J.C. conceived the research. K.-S.L., Y.F., F.X., J.C. and Q.S. carried out theoretical model studies. R.L. and M.G.V. performed DFT calculations. K.-S.L., Y.F., H.F., A.P., S.P.,

Q.S. developed the new procedure for correlated topological materials search and applied it to identify candidate materials for the proposed correlated topological semimetals. H.F., A.P., S.P. synthesized the materials and performed the physical properties measurements. K.-S.L., Y.F., and Q.S. wrote the manuscript, with inputs from all authors.

Competing interests

The authors declare no competing interests.

Additional information

Correspondence and requests for materials should be addressed to Q.S. (qmsi@rice.edu).

Primary candidate heavy fermion material							
Material	SG #	SG	T_N	T_K	Resistivity	Sommerfeld coefficient	Crossing
Chiral heavy fermion material							
CePt ₂ B	180	$P6_222$	2.1K	3.5 – 5K	Metallic	Large C_p/T	WP
Achiral heavy fermion material							
Ce ₂ NiGe ₃	190	$P\bar{6}2c$	3.2K		Semimetallic	25 mJ/K ² Ce-mol	WNL
Ce ₂ RhSi ₃	190	$P\bar{6}2c$	4.5 – 6.8K	9 – 12K	Semimetallic	Large	WNL
Ce ₆ Co _{2-δ} Si ₃	176	$P6_3/m$	\times			162 mJ/K ² Ce-mol	DNL
Ce ₆ Rh ₃₂ P ₁₇	176	$P6_3/m$	\times		Semimetallic		DNL

TABLE I. Summary of the physical properties of the primary candidate materials Ce₆Rh₃₂P₁₇⁴⁷, Ce₆Co_{2- δ} Si₃^{48,49}, CePt₂B^{37,38}, Ce₂NiGe₃^{39,42}, and Ce₂RhSi₃^{40,41,43-46}. “SG” means “space group”. T_N denotes the anti-ferromagnetic transition temperature. A “ \times ” mark in T_N means no magnetic transition is reported. T_K denotes the Kondo temperature. C_p denotes the specific heat. A blank entry means the physical property is not reported. “DNL” means “Dirac nodal line”, “WP” means “Weyl point”, and “WNL” means “Weyl nodal line”. We note that in addition to SG no. 190 ($P\bar{6}2c$)³⁹⁻⁴¹, Ce₂NiGe₃⁴² and Ce₂RhSi₃⁴³⁻⁴⁶ may crystallize in other forms. We also note that the chemical formula for Ce₆Co_{2- δ} Si₃ is Ce₆Co_{1.67}Si₃, corresponding to $\delta = 0.33$ ^{48,49}. We refer readers to Supplementary Note 12 for a detailed description of the primary candidate materials, such as how different physical properties are determined. In Supplementary Note 15 we present the results of our new experiments on Ce₂NiGe₃, which not only confirm properties reported in the literature, such as the SG no. 190 ($P\bar{6}2c$), but also provide new experimental data such as magnetoresistivity and anomalous Hall conductivity. We have also confirmed the presence of Weyl points and Weyl nodal lines in CePt₂B [Fig. 3] and Ce₂NiGe₃ [Supplementary Fig. S14], respectively, based on DFT calculations.

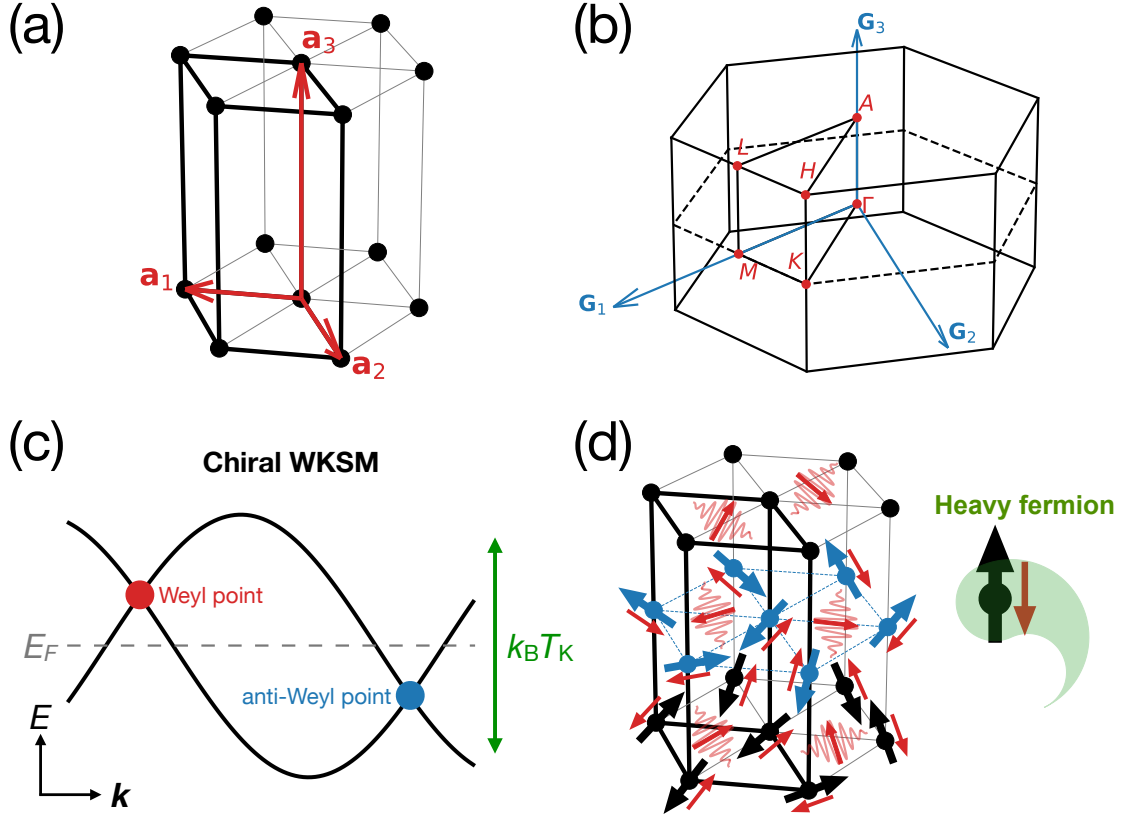


FIG. 1. (a) Hexagonal Bravais lattice in three dimensions in which the primitive unit cell is denoted by thick black lines. The three Bravais lattice vectors \mathbf{a}_i ($i = 1, 2, 3$) are also shown. (b) Brillouin zone (BZ) and the high-symmetry points of hexagonal crystal systems. The three reciprocal lattice vectors \mathbf{G}_i ($i = 1, 2, 3$) are also shown. Throughout this work, we refer to the top (or bottom) BZ boundary as $\mathbf{k} = k_1\mathbf{G}_1 + k_2\mathbf{G}_2 + k_3\mathbf{G}_3$ with $k_3 = 1/2$ (or $k_3 = -1/2$). (c) Schematic representation of the chiral WKSM phase, where the Kondo-driven Weyl point and anti-Weyl point that carry opposite chiral charges are located at different energies. The heavy-fermion energy scale is set by the Kondo scale $k_B T_K$. The Fermi energy is denoted as E_F . (d) The crystal structure of a periodic Anderson model on a hexagonal crystal system with two sub-lattices per unit cell. The sub-lattice at $(0, 0, 0)$ is denoted by black filled circles, and the sub-lattice at $(0, 0, 1/2)$ is denoted by blue filled circles. The itinerant c electrons are denoted by wave packets with their electron spins represented by arrows. The f electrons are localized on the sub-lattices $(0, 0, 0)$ and $(0, 0, 1/2)$, and we also use arrows to indicate their fluctuating magnetic moments. The Kondo singlet emerges through the antiferromagnetic Kondo interaction between the localized f electron and the itinerant c electron. This leads to the paramagnetic phase of the periodic Anderson model with heavy-fermion excitations.

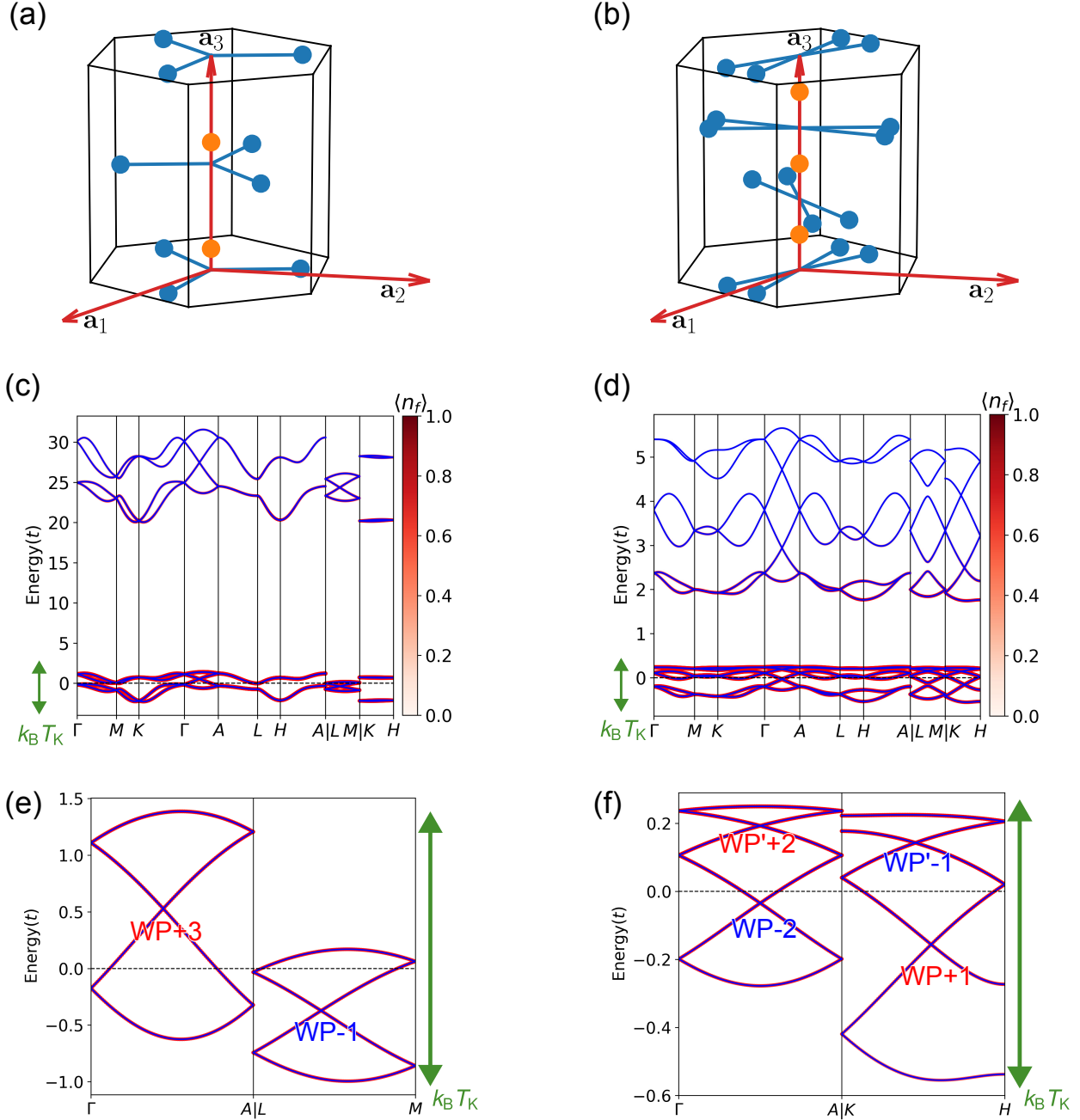


FIG. 2. (a) Unit cell of a chiral crystal in space group no. 173. (b) Unit cell of a chiral crystal in space group no. 180. (c) The excitation spectrum of the hexagonal periodic Anderson model with chiral space group no. 173 ($P6_3$) and (d) with chiral space group no. 180 ($P6_222$). The color map indicates the portion of the f electron for a given excitation. The energies are in unit of nearest hopping amplitude t . In (e) and (f), we show the enlarged view of the band crossings demonstrating the low-energy heavy Weyl fermions in (c) and (d), respectively. In (e) and (f) we also label the chiral charge of each Weyl point. The Kondo energy scale is denoted as $k_B T_K$.

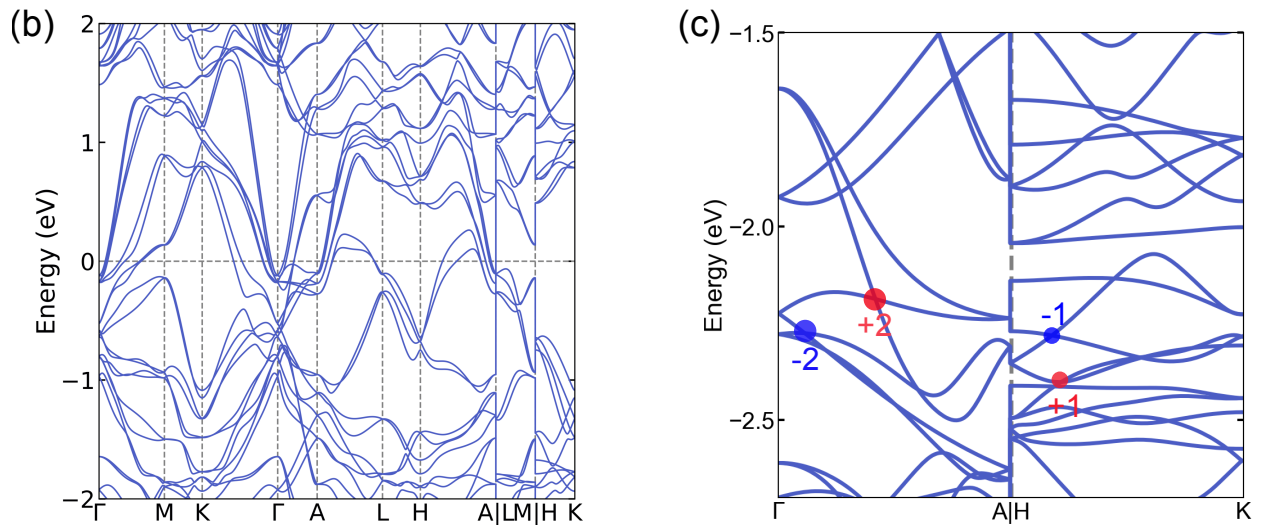
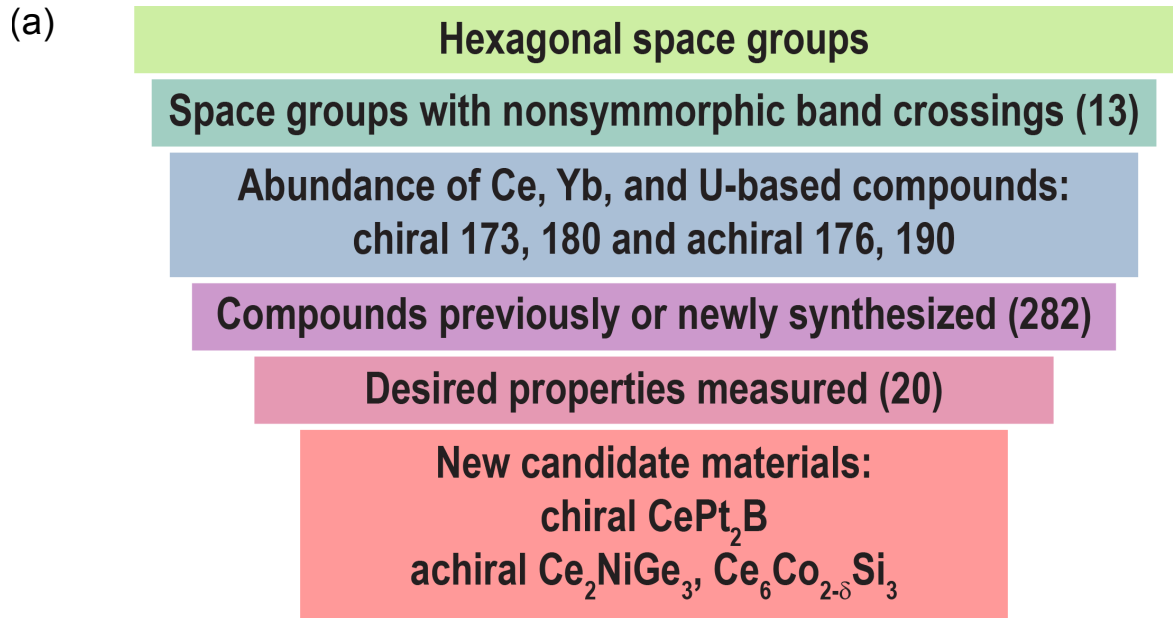


FIG. 3. (a) Schematic illustration of the materials searching procedure for hexagonal crystal systems. Starting from compounds crystallizing in hexagonal structures, we identify space groups hosting nonsymmorphic band crossings. We further focus on Ce-, Yb-, and U-based compounds that have been previously or newly synthesized and experimentally characterized. This screening process leads to the identification of new candidate materials for chiral and achiral WKSMS. (b) DFT band structures (with spin-orbit couplings) of CePt_2B with chiral space group no. 180 ($P6_222$). (c) The corresponding zoomed-in band structure along $\Gamma - A$ and $K - H$. The symmetry enforced Weyl points are marked with their topological charges.

Supplementary information for: Chiral Weyl-Kondo semimetals and hexagonal heavy fermion systems

CONTENTS

References	8
Supplementary Note 1. Details of the tight-binding models	28
Supplementary Note 2. Parton formalism	30
Supplementary Note 3. Extended result for the Anderson lattice model with the chiral space group no. 173	36
Supplementary Note 4. Extended result for the Anderson lattice model with the chiral space group no. 180	36
Supplementary Note 5. Anderson lattice model with the achiral topological Kondo semimetals for the achiral space group no. 176	39
Supplementary Note 6. Achiral topological Kondo semimetals for the achiral space group no. 190 ($P\bar{6}2c$)	42
Supplementary Note 7. Numerical methods for computing topological charges of Weyl points	44
1. Discrete jump of Chern number	44
2. Direct computation of Berry flux	44
3. Symmetry indicator for chiral charges	46
Supplementary Note 8. Quantized non-Abelian Berry phases in space group no. 176 ($P6_3/m$) with spin-1/2 time-reversal symmetry	47
1. Derivation of quantized non-Abelian Berry phases	48
2. Surface states from Wannier centers	54
Supplementary Note 9. Implication of $\{C_{2z}\mathcal{T} 0, 0, 1/2\}$ symmetry in space group no. 173 ($P6_3$) with spin-1/2 \mathcal{T} symmetry	55

Supplementary Note 10. DFT results for Ce_2NiGe_3	56
Supplementary Note 11. Procedure for searching candidate materials	57
Supplementary Note 12. Primary candidate materials	59
1. CePt_2B	59
2. $\text{Ce}_6\text{Rh}_{32}\text{P}_{17}$	60
3. $\text{Ce}_6\text{Co}_{2-\delta}\text{Si}_3$ ($\delta = 0.33$)	62
4. Ce_2NiGe_3	63
5. Ce_2RhSi_3	65
Supplementary Note 13. Additional candidate materials	66
1. $\text{Ce}_6\text{Ni}_{2-\delta}\text{Si}_3$ ($\delta = 0.33$)	67
2. $\text{Ce}_5\text{Ni}_{2-\delta}\text{Si}_3$ ($\delta = 0.15$)	70
3. $\text{Ce}_5\text{Ni}_2\text{Si}_3$	71
4. $\text{Ce}_{20}\text{Ni}_{42}\text{As}_{31}$	71
5. $\text{Ce}_{20}\text{Ni}_{42}\text{P}_{30}$	72
Supplementary Note 14. Other candidate materials	72
1. $\text{Ce}_3\text{CuSnSe}_7$	74
2. $\text{Ce}_3\text{Ge}_{1.47}\text{Se}_7$	74
3. $\text{Ce}_3\text{Mg}_{0.5}\text{SiS}_7$	74
4. $\text{Ce}_{18}\text{W}_{10}\text{O}_{57}$	74
5. $\text{Cu}_2\text{U}_3\text{S}_7$	75
6. $\text{Cu}_2\text{U}_3\text{Se}_7$	75
7. $\text{U}_6\text{Ni}_{20}\text{P}_{13}$	75
8. U_7Te_{12}	75
9. $\text{Ba}_3\text{YbB}_9\text{O}_{18}$	76
10. YbBO_3	76
Supplementary Note 15. New experiments on candidate materials	76
1. Ce_2NiGe_3	77
2. $\text{Ce}_3\text{CuSnSe}_7$	78

Supplementary Note 1. DETAILS OF THE TIGHT-BINDING MODELS

In this section, we provide the details of our tight-binding models. Our models are partly constructed using the open-source Python Tight Binding (PythTB) software package⁵¹.

Hexagonal crystal systems describe crystal structures with a hexagonal Bravais lattice and a sixfold rotation (or roto-inversion) axis. The Bravais lattice vectors of the hexagonal crystal system are $\mathbf{a}_1 = (a, 0, 0)$, $\mathbf{a}_2 = (-a/2, \sqrt{3}a/2, 0)$, and $\mathbf{a}_3 = (0, 0, c)$, where a and c are the hexagonal lattice constants. Throughout our studies, all the position-space vectors are represented in the reduced coordinate, which means (x_1, x_2, x_3) represents $x_1\mathbf{a}_1 + x_2\mathbf{a}_2 + x_3\mathbf{a}_3$.

The hopping strength $t_{(\alpha,\sigma)\leftarrow(\alpha',\sigma')}^c(\mathbf{R}) \in \mathbb{C}$ for the c electrons can be represented as a 2×2 matrix $[t_{\alpha\leftarrow\alpha'}^c(\mathbf{R})]$ whose matrix element $[t_{\alpha\leftarrow\alpha'}^c(\mathbf{R})]_{\sigma,\sigma'} \equiv t_{(\alpha,\sigma)\leftarrow(\alpha',\sigma')}^c(\mathbf{R})$. Specifically, when $[t_{\alpha\leftarrow\alpha'}^c(\mathbf{R})]$ does not represent an on-site potential, we require that $[t_{\alpha\leftarrow\alpha'}^c(\mathbf{R})]$ takes the following form^{52,53}

$$t_0\sigma_0 + i\vec{t} \cdot \vec{\sigma} = t_0\sigma_0 + i(t_1\sigma_1 + t_2\sigma_2 + t_3\sigma_3) \quad (\text{S1})$$

where $t_\mu \in \mathbb{R}$ ($\mu = 0, 1, 2, 3$), σ_0 is the 2×2 identity matrix $\begin{pmatrix} 1 & 0 \\ 0 & 1 \end{pmatrix}$, σ_j ($j = 1, 2, 3$) are the Pauli matrices given by

$$\sigma_1 = \begin{pmatrix} 0 & 1 \\ 1 & 0 \end{pmatrix}, \quad \sigma_2 = \begin{pmatrix} 0 & -i \\ i & 0 \end{pmatrix}, \quad \sigma_3 = \begin{pmatrix} 1 & 0 \\ 0 & -1 \end{pmatrix}. \quad (\text{S2})$$

t_0 represents the spin-independent part of the hopping strength, and t_j ($j = 1, 2, 3$) represents the spin-dependent part of the hopping strength. This form of $[t_{\alpha\leftarrow\alpha'}^c(\mathbf{R})]$ automatically preserves the spin-1/2 time-reversal symmetry. When $\alpha = \alpha'$ and $\mathbf{R} = \mathbf{0}$, $[t_{\alpha\leftarrow\alpha}^c(\mathbf{0})]$ represents an on-site potential which we require to take the form $m\sigma_0$ ($m \in \mathbb{R}$) to preserve the spin-1/2 time-reversal symmetry. To ensure the Hermiticity of the Hamiltonian, $\left(t_{(\alpha,\sigma)\leftarrow(\alpha',\sigma')}^c(\mathbf{R})\right)^* = t_{(\alpha',\sigma')\leftarrow(\alpha,\sigma)}^c(-\mathbf{R})$.

We here outline the procedure to construct a model respecting a certain space group symmetry. Consider a space group SG and a lattice with lattice translation \mathbb{T} , which is a normal subgroup of SG . The most general \mathbb{T} -symmetric tight-binding Hamiltonian takes the form

$$H = \sum_{\mathbf{R}'} \sum_{\mathbf{R}, (\alpha,\sigma), (\alpha',\sigma')} t_{(\alpha,\sigma)\leftarrow(\alpha',\sigma')}^c(\mathbf{R}) c_{\mathbf{R}'+\mathbf{R}, \alpha, \sigma}^\dagger c_{\mathbf{R}', \alpha', \sigma'}. \quad (\text{S3})$$

Consider a coset-decomposition

$$SG = g_1\mathbb{T} + g_2\mathbb{T} + \dots g_n\mathbb{T}, \quad (\text{S4})$$

where the representatives $g_1, \dots, g_n \in SG$ and they act on real space position vector \mathbf{r} ,

$$g_i = \{R_i|\mathbf{t}_i\}, \quad g_i\mathbf{r} = R_i\mathbf{r} + \mathbf{t}_i. \quad (\text{S5})$$

Here R_i and \mathbf{t}_i stands for rotational and translational part of the symmetry element. Denote the set of coset-representatives $\mathcal{C} = \{g_1, \dots, g_n\}$. Note \mathcal{C} needs not be a group.

The symmetric Hamiltonians should satisfy conditions

$$H = \frac{1}{|\mathcal{C}|} \sum_{g \in \mathcal{C}} gHg^{-1}, \quad (\text{S6})$$

$$H = \frac{1}{2} (H + \mathcal{T}H\mathcal{T}^{-1}), \quad (\text{S7})$$

$$H = \frac{1}{2} (H + H^\dagger). \quad (\text{S8})$$

By examining these constraints, we can derive the symmetric hopping terms including SOC terms for real space tight-binding models.

We list the parameters of our model with space group no. 173 ($P6_3$) in Supplementary Table S1, space group no. 176 ($P6_3/m$) in Supplementary Table S2, space group no. 180 ($P6_22$) in Supplementary Table S3, and space group no. 190 ($P\bar{6}2c$) in Supplementary Table S4.

(α, σ)	(α', σ')	n_1	n_2	n_3	$t_{(\alpha, \sigma) \leftarrow (\alpha', \sigma')}^c(\mathbf{R})$	# of related hoppings
(1, \uparrow)	(0, \uparrow)	0	0	-1	$1 + i$	8
(0, \uparrow)	(0, \uparrow)	-1	0	0	$0.5 + i$	24
(0, \uparrow)	(0, \uparrow)	-2	-1	0	$0.08i$	24
(0, \downarrow)	(0, \uparrow)	-2	-1	0	0.08	24
(0, \uparrow)	(0, \uparrow)	-1	-1	-1	0.16	24
(0, \downarrow)	(0, \uparrow)	-1	-1	-1	$0.16 + 0.16i$	24
(1, \uparrow)	(0, \uparrow)	-1	-1	0	0.16	24
(1, \downarrow)	(0, \uparrow)	-1	-1	0	$0.16 + 0.16i$	24

Supplementary Table S1. Independent tight-binding parameters for the model with space group no. 173 ($P6_3$).

(α, σ)	(α', σ')	n_1	n_2	n_3	$t_{(\alpha,\sigma)\leftarrow(\alpha',\sigma')}^c(\mathbf{R})$	# of related hoppings
(1, \uparrow)	(0, \uparrow)	0	0	-1	1.0	8
(1, \uparrow)	(0, \uparrow)	-1	-1	-1	$0.6i$	48
(1, \uparrow)	(0, \downarrow)	-1	-1	-1	0.6	48
(1, \uparrow)	(0, \uparrow)	-2	-1	-1	$0.6i$	48
(1, \uparrow)	(0, \downarrow)	-2	-1	-1	0.6	48

Supplementary Table S2. Independent tight-binding parameters for the model with space group no. 176 ($P6_3/m$).

(α, σ)	(α', σ')	n_1	n_2	n_3	$t_{(\alpha,\sigma)\leftarrow(\alpha',\sigma')}^c(\mathbf{R})$	# of related hoppings
(2, \uparrow)	(0, \uparrow)	0	0	-1	1.0	12
(0, \uparrow)	(0, \uparrow)	-1	-1	0	0.1	24
(0, \uparrow)	(0, \downarrow)	-1	-1	0	0.2	24
(1, \uparrow)	(1, \downarrow)	-1	-1	0	0.2	12

Supplementary Table S3. Independent tight-binding parameters for the model with space group no. 180 ($P6_22$).

Supplementary Note 2. PARTON FORMALISM

In this section, we review the parton formalism, which could be employed to study mixed-valence phenomena in Kondo-lattice systems, typically formulated microscopically as periodic Anderson models. We will also provide our numerical procedure, as well as the assumptions we made, in obtaining the saddle-point solutions of the periodic Anderson models⁵⁰.

We begin by writing down a periodic Anderson model with some generality. The itinerant c electrons and the localized f electrons form such a system. We will denote the unit cell by $\mathbf{R} = \sum_{j=1}^3 n_j \mathbf{a}_j$ ($n_j \in \mathbb{Z}$), the sub-lattice within the unit cell by $\alpha = 1 \dots n_{sub}$, and the spin by $\sigma = \uparrow, \downarrow$. We assume that both the c and f electrons are specified by \mathbf{R} , α , and σ . In other words, each sub-lattice hosts both spin-1/2 c and f orbitals. The periodic Anderson model we consider here can be written as Eq. (1).

In the infinite- U limit, the number of f electrons on each site (with fixed \mathbf{R} and α) can only be 0 or 1, leading to the non-holomorphic constraint $\sum_{\sigma} \langle f_{\mathbf{R},\alpha,\sigma}^{\dagger} f_{\mathbf{R},\alpha,\sigma} \rangle = \sum_{\sigma} \langle n_{\mathbf{R},\alpha,\sigma}^f \rangle \leq 1$. Hereafter, $\langle \dots \rangle$ is understood as the ground state expectation value at zero temperature or the

(α, σ)	(α', σ')	n_1	n_2	n_3	$t_{(\alpha,\sigma)\leftarrow(\alpha',\sigma')}^c(\mathbf{R})$	# of related hoppings
$(1, \uparrow)$	$(0, \uparrow)$	0	0	-1	1.0	8
$(0, \uparrow)$	$(0, \downarrow)$	-1	-1	0	0.2	24
$(1, \uparrow)$	$(0, \downarrow)$	-1	-1	-1	0.5	48
$(1, \uparrow)$	$(0, \uparrow)$	-1	-1	0	0.2	48

Supplementary Table S4. Independent tight-binding parameters for the model with space group no. 190 ($P\bar{6}2c$).

thermal average at finite temperature. To treat the constraint $\sum_{\sigma} \langle n_{\mathbf{R},\alpha,\sigma}^f \rangle \leq 1$, an auxiliary boson operator b and a Lagrange multiplier λ are introduced such that the periodic Anderson model in the infinite- U limit in the auxiliary boson representation is

$$\begin{aligned}
H_{\text{auxiliary-boson}} = & \sum_{\mathbf{R}, \mathbf{R}', \alpha, \sigma, \alpha', \sigma'} c_{\mathbf{R}'+\mathbf{R}, \alpha, \sigma}^{\dagger} t_{(\alpha, \sigma) \leftarrow (\alpha', \sigma')}^c(\mathbf{R}) c_{\mathbf{R}', \alpha', \sigma'} \\
& + E_f \sum_{\mathbf{R}, \alpha, \sigma} n_{\mathbf{R}, \alpha, \sigma}^f - \mu \sum_{\mathbf{R}, \alpha, \sigma} \left(n_{\mathbf{R}, \alpha, \sigma}^c + n_{\mathbf{R}, \alpha, \sigma}^f \right) \\
& + V \sum_{\mathbf{R}, \alpha, \sigma} \left(c_{\mathbf{R}, \alpha, \sigma}^{\dagger} (b^{\dagger} f_{\mathbf{R}, \alpha, \sigma}) + (f_{\mathbf{R}, \alpha, \sigma}^{\dagger} b) c_{\mathbf{R}, \alpha, \sigma} \right) \\
& + \lambda \sum_{\mathbf{R}, \alpha} \left(\left[\sum_{\sigma} f_{\mathbf{R}, \alpha, \sigma}^{\dagger} f_{\mathbf{R}, \alpha, \sigma} \right] + b^{\dagger} b - 1 \right), \tag{S9}
\end{aligned}$$

where in the c - f hybridization term with V the localized f electron operators $f_{\mathbf{R}, \alpha, \sigma}^{\dagger}$ and $f_{\mathbf{R}, \alpha, \sigma}$ are replaced by $f_{\mathbf{R}, \alpha, \sigma}^{\dagger} b$ and $b^{\dagger} f_{\mathbf{R}, \alpha, \sigma}$, respectively. At the saddle-point level, a solution can be obtained by considering the condensation of the auxiliary boson operator, which means effectively replacing b by $\langle b \rangle$. We may absorb the complex phase of $\langle b \rangle$ by the f electron operators such that we further replace $\langle b \rangle$ by r , where r is a real number. This leads to

$$\begin{aligned}
H_{\text{auxiliary-boson}}^{\text{saddle-point}} = & \sum_{\mathbf{R}, \mathbf{R}', \alpha, \sigma, \alpha', \sigma'} c_{\mathbf{R}'+\mathbf{R}, \alpha, \sigma}^{\dagger} t_{(\alpha, \sigma) \leftarrow (\alpha', \sigma')}^c(\mathbf{R}) c_{\mathbf{R}', \alpha', \sigma'} \\
& + E_f \sum_{\mathbf{R}, \alpha, \sigma} n_{\mathbf{R}, \alpha, \sigma}^f - \mu \sum_{\mathbf{R}, \alpha, \sigma} \left(n_{\mathbf{R}, \alpha, \sigma}^c + n_{\mathbf{R}, \alpha, \sigma}^f \right) \\
& + rV \sum_{\mathbf{R}, \alpha, \sigma} \left(c_{\mathbf{R}, \alpha, \sigma}^{\dagger} f_{\mathbf{R}, \alpha, \sigma} + f_{\mathbf{R}, \alpha, \sigma}^{\dagger} c_{\mathbf{R}, \alpha, \sigma} \right) \\
& + \lambda \sum_{\mathbf{R}, \alpha} \left(\left[\sum_{\sigma} f_{\mathbf{R}, \alpha, \sigma}^{\dagger} f_{\mathbf{R}, \alpha, \sigma} \right] + r^2 - 1 \right). \tag{S10}
\end{aligned}$$

In $H_{\text{auxiliary-boson}}^{\text{saddle-point}}$, the hybridization strength V is re-normalized by a factor of $r \in \mathbb{R}$. The term with the Lagrange multiplier λ is to implement the constraint $\sum_{\sigma} \langle f_{\mathbf{R},\alpha,\sigma}^{\dagger} f_{\mathbf{R},\alpha,\sigma} \rangle = \sum_{\sigma} \langle n_{\mathbf{R},\alpha,\sigma}^f \rangle \leq 1$ via $1 = \left[\sum_{\sigma} \langle f_{\mathbf{R},\alpha,\sigma}^{\dagger} f_{\mathbf{R},\alpha,\sigma} \rangle \right] + r^2$, which means that r^2 is equal to how much charge is lost from the localized f electron moment per site due to the interaction with the itinerant c electrons. The number of f electrons on each site is then equal to $1 - r^2$.

In order to solve for the excitation spectrum, a set of self-consistent equations is required in order to determine r , λ , and μ . The saddle-point solution for r and λ can be obtained by requiring

$$\left\langle \frac{\delta H_{\text{auxiliary-boson}}^{\text{saddle-point}}}{\delta \lambda} \right\rangle = 0, \quad \left\langle \frac{\delta H_{\text{auxiliary-boson}}^{\text{saddle-point}}}{\delta r} \right\rangle = 0, \quad (\text{S11})$$

which leads to the following self-consistent equations

$$r = \sqrt{1 - \frac{1}{n_{\text{sub}}} \sum_{\alpha,\sigma} \langle f_{\mathbf{R},\alpha,\sigma}^{\dagger} f_{\mathbf{R},\alpha,\sigma} \rangle}, \quad (\text{S12})$$

$$\lambda = \frac{-V}{r \cdot n_{\text{sub}}} \sum_{\alpha,\sigma} \text{Re} \langle c_{\mathbf{R},\alpha,\sigma}^{\dagger} f_{\mathbf{R},\alpha,\sigma} \rangle, \quad (\text{S13})$$

respectively. In obtaining the expressions of r and λ , we have assumed that the saddle-point solution preserves the original translation symmetry of H , such that $\langle f_{\mathbf{R},\alpha,\sigma}^{\dagger} f_{\mathbf{R},\alpha,\sigma} \rangle$ and $\langle c_{\mathbf{R},\alpha,\sigma}^{\dagger} f_{\mathbf{R},\alpha,\sigma} \rangle$ are independent of \mathbf{R} . We have also assumed that the saddle-point solution preserves the original space-group symmetry in H , including the spin-1/2 time-reversal symmetry. We have further assumed that all the sub-lattices are related to each other by the symmetry in the space group, otherwise one would need to consider different parameters r_{α} and λ_{α} ($\alpha = 1 \dots n_{\text{sub}}$), each of which has a self-consistent equation, for different sub-lattices.

$H_{\text{auxiliary-boson}}^{\text{saddle-point}}$ can also be written as

$$H_{\text{auxiliary-boson}}^{\text{saddle-point}} = \left(\sum_{\mathbf{k}} \Psi_{\mathbf{k}}^{\dagger} [H_{\text{eff}}(\mathbf{k})] \Psi_{\mathbf{k}} \right) + \lambda N_{\text{cell}} n_{\text{sub}} (r^2 - 1), \quad (\text{S14})$$

where

$$\Psi_{\mathbf{k}}^{\dagger} = \left(c_{\mathbf{k},1,\uparrow}^{\dagger} \ c_{\mathbf{k},1,\downarrow}^{\dagger} \ \cdots \ c_{\mathbf{k},n_{\text{sub}},\uparrow}^{\dagger} \ c_{\mathbf{k},n_{\text{sub}},\downarrow}^{\dagger} \ f_{\mathbf{k},1,\uparrow}^{\dagger} \ f_{\mathbf{k},1,\downarrow}^{\dagger} \ \cdots \ f_{\mathbf{k},n_{\text{sub}},\uparrow}^{\dagger} \ f_{\mathbf{k},n_{\text{sub}},\downarrow}^{\dagger} \right). \quad (\text{S15})$$

We have adopted the following conventions for the Bloch basis operators

$$c_{\mathbf{k},\alpha,\sigma}^{\dagger} = \frac{1}{\sqrt{N_{\text{cell}}}} \sum_{\mathbf{R}} e^{i\mathbf{k} \cdot (\mathbf{R} + \mathbf{r}_{\alpha}^c)} c_{\mathbf{R},\alpha,\sigma}^{\dagger}, \quad c_{\mathbf{k},\alpha,\sigma} = \frac{1}{\sqrt{N_{\text{cell}}}} \sum_{\mathbf{R}} e^{-i\mathbf{k} \cdot (\mathbf{R} + \mathbf{r}_{\alpha}^c)} c_{\mathbf{R},\alpha,\sigma}, \quad (\text{S16})$$

$$f_{\mathbf{k},\alpha,\sigma}^{\dagger} = \frac{1}{\sqrt{N_{\text{cell}}}} \sum_{\mathbf{R}} e^{i\mathbf{k} \cdot (\mathbf{R} + \mathbf{r}_{\alpha}^f)} f_{\mathbf{R},\alpha,\sigma}^{\dagger}, \quad f_{\mathbf{k},\alpha,\sigma} = \frac{1}{\sqrt{N_{\text{cell}}}} \sum_{\mathbf{R}} e^{-i\mathbf{k} \cdot (\mathbf{R} + \mathbf{r}_{\alpha}^f)} f_{\mathbf{R},\alpha,\sigma}, \quad (\text{S17})$$

and their relation to the position-space operators

$$c_{\mathbf{R},\alpha,\sigma}^\dagger = \frac{1}{\sqrt{N_{cell}}} \sum_{\mathbf{k}} e^{-i\mathbf{k}\cdot(\mathbf{R}+\mathbf{r}_\alpha^c)} c_{\mathbf{k},\alpha,\sigma}^\dagger, \quad c_{\mathbf{R},\alpha,\sigma} = \frac{1}{\sqrt{N_{cell}}} \sum_{\mathbf{k}} e^{i\mathbf{k}\cdot(\mathbf{R}+\mathbf{r}_\alpha^c)} c_{\mathbf{k},\alpha,\sigma}, \quad (\text{S18})$$

$$f_{\mathbf{R},\alpha,\sigma}^\dagger = \frac{1}{\sqrt{N_{cell}}} \sum_{\mathbf{k}} e^{-i\mathbf{k}\cdot(\mathbf{R}+\mathbf{r}_\alpha^f)} f_{\mathbf{k},\alpha,\sigma}^\dagger, \quad f_{\mathbf{R},\alpha,\sigma} = \frac{1}{\sqrt{N_{cell}}} \sum_{\mathbf{k}} e^{i\mathbf{k}\cdot(\mathbf{R}+\mathbf{r}_\alpha^f)} f_{\mathbf{k},\alpha,\sigma}, \quad (\text{S19})$$

where \mathbf{r}_α^c and \mathbf{r}_α^f are the positions of the c orbitals and f orbitals, respectively, on the α sub-lattice within the unit cell. Note that the positions of the basis states do not depend on the spin index σ . In our model, we have also assumed $\mathbf{r}_\alpha^c = \mathbf{r}_\alpha^f$. The effective Bloch Hamiltonian matrix is

$$[H_{eff}(\mathbf{k})] = \begin{pmatrix} [H^c(\mathbf{k})] - \mu\mathbb{I} & rV\mathbb{I} \\ rV\mathbb{I} & (E_f - \mu + \lambda)\mathbb{I} \end{pmatrix}, \quad (\text{S20})$$

where $[H^c(\mathbf{k})]$ is the Bloch Hamiltonian matrix constructed from the hopping strengths $t_{(\alpha,\sigma)\leftarrow(\alpha',\sigma')}^c(\mathbf{R})$ for the c electron through

$$[H^c(\mathbf{k})]_{(\alpha,\sigma),(\alpha',\sigma')} = \sum_{\mathbf{R}} t_{(\alpha,\sigma)\leftarrow(\alpha',\sigma')}^c(\mathbf{R}) e^{-i\mathbf{k}\cdot(\mathbf{R}+\mathbf{r}_\alpha^c-\mathbf{r}_{\alpha'}^c)}, \quad (\text{S21})$$

and \mathbb{I} is an identity matrix with an appropriate shape.

We now describe the numerical procedure for determining (μ, r, λ) . To begin, let us first cast the self-consistent equations using the eigenvalues and eigenvectors of $[H_{eff}(\mathbf{k})]$:

$$[H_{eff}(\mathbf{k})]|u_{n,\mathbf{k}}\rangle = \epsilon_{n,\mathbf{k}}|u_{n,\mathbf{k}}\rangle, \quad (\text{S22})$$

where

$$|u_{n,\mathbf{k}}\rangle = \left(u_{n,\mathbf{k}}^{c,1,\uparrow} \quad u_{n,\mathbf{k}}^{c,1,\downarrow} \quad \dots \quad u_{n,\mathbf{k}}^{c,n_{sub},\uparrow} \quad u_{n,\mathbf{k}}^{c,n_{sub},\downarrow} \quad u_{n,\mathbf{k}}^{f,1,\uparrow} \quad u_{n,\mathbf{k}}^{f,1,\downarrow} \quad \dots \quad u_{n,\mathbf{k}}^{f,n_{sub},\uparrow} \quad u_{n,\mathbf{k}}^{f,n_{sub},\downarrow} \right)^T. \quad (\text{S23})$$

The self-consistent equations can be written as

$$r = \sqrt{1 - \frac{1}{n_{sub}} \frac{1}{N_{cell}} \sum_{\alpha,\sigma} \sum_{\mathbf{k}} \langle f_{\mathbf{k},\alpha,\sigma}^\dagger f_{\mathbf{k},\alpha,\sigma} \rangle} \quad (\text{S24})$$

$$\lambda = \frac{-V}{r \cdot n_{sub}} \frac{1}{N_{cell}} \sum_{\alpha,\sigma} \sum_{\mathbf{k}} \text{Re} \langle c_{\mathbf{k},\alpha,\sigma}^\dagger f_{\mathbf{k},\alpha,\sigma} \rangle \quad (\text{S25})$$

where we have used the assumption $\mathbf{r}_\alpha^c = \mathbf{r}_\alpha^f$ and that the translation symmetry is preserved. In terms of the eigenvalues and eigenvectors of $[H_{eff}(\mathbf{k})]$, the self-consistent equations can then be

written as

$$r = \sqrt{1 - \frac{1}{n_{sub}} \frac{1}{N_{cell}} \sum'_{n,\mathbf{k}} \sum_{\alpha,\sigma} |u_{n,\mathbf{k}}^{f,\alpha,\sigma}|^2}, \quad (\text{S26})$$

$$\lambda = \frac{-V}{r \cdot n_{sub}} \frac{1}{N_{cell}} \text{Re} \left(\sum'_{n,\mathbf{k}} \sum_{\alpha,\sigma} (u_{n,\mathbf{k}}^{c,\alpha,\sigma})^* u_{n,\mathbf{k}}^{f,\alpha,\sigma} \right), \quad (\text{S27})$$

where thereafter the summation $\sum'_{n,\mathbf{k}}$ is over all the occupied eigenvectors $|u_{n,\mathbf{k}}\rangle$. We will impose the filling constraint such that each sub-lattice in the unit cell has the fermion number expectation value (or thermal average) equal to 1:

$$\sum_{\sigma} \left(\left\langle c_{\mathbf{R},\alpha,\sigma}^{\dagger} c_{\mathbf{R},\alpha,\sigma} \right\rangle + \left\langle f_{\mathbf{R},\alpha,\sigma}^{\dagger} f_{\mathbf{R},\alpha,\sigma} \right\rangle \right) = 1. \quad (\text{S28})$$

Note the right-hand side of the above equation is independent of \mathbf{R} , since we have assumed that the translation symmetry is preserved. Since we also assume that different sub-lattices are related to each other by the symmetry in the space group, we have that $\left\langle c_{\mathbf{R},\alpha,\sigma}^{\dagger} c_{\mathbf{R},\alpha,\sigma} \right\rangle = \left\langle c_{\mathbf{R},\alpha',\sigma}^{\dagger} c_{\mathbf{R},\alpha',\sigma} \right\rangle$ and $\left\langle f_{\mathbf{R},\alpha,\sigma}^{\dagger} f_{\mathbf{R},\alpha,\sigma} \right\rangle = \left\langle f_{\mathbf{R},\alpha',\sigma}^{\dagger} f_{\mathbf{R},\alpha',\sigma} \right\rangle$ with $\alpha \neq \alpha'$, which allows us to cast the filling constraint into

$$\sum_{\alpha,\sigma} \left(\left\langle c_{\mathbf{R},\alpha,\sigma}^{\dagger} c_{\mathbf{R},\alpha,\sigma} \right\rangle + \left\langle f_{\mathbf{R},\alpha,\sigma}^{\dagger} f_{\mathbf{R},\alpha,\sigma} \right\rangle \right) = n_{sub}. \quad (\text{S29})$$

This means that the total filling of the system is n_{sub} per unit cell. Written using the eigenvalues and eigenvalues of $[H_{eff}(\mathbf{k})]$, the filling constraint becomes

$$\begin{aligned} \frac{1}{N_{cell}} \sum'_{n,\mathbf{k}} \sum_{\alpha,\sigma} \left(|u_{n,\mathbf{k}}^{c,\alpha,\sigma}|^2 + |u_{n,\mathbf{k}}^{f,\alpha,\sigma}|^2 \right) &= \frac{1}{N_{cell}} \sum'_{n,\mathbf{k}} 1 \\ &= n_{sub}, \end{aligned} \quad (\text{S30})$$

which means

$$\sum'_{n,\mathbf{k}} 1 = n_{sub} N_{cell}. \quad (\text{S31})$$

This allows us to consistently determine the chemical potential μ , below which are occupied eigenvectors, and which is used to define the summation $\sum'_{n,\mathbf{k}}$. Since the number of \mathbf{k} points used in the numerical calculation is N_{cell} , we have that the number of occupied eigenvectors below the chemical potential is equal to $n_{sub} N_{cell}$.

We will determine (μ, r, l) iteratively in the following manner. In the i^{th} step, we use a set of (μ_i, r_i, λ_i) to construct $[H_{eff}(\mathbf{k})]$ and obtain its eigenvalues $\epsilon_{n,\mathbf{k}}$ and eigenvectors $|u_{n,\mathbf{k}}\rangle$. We then obtain a new chemical potential μ_{i+1} that satisfies the filling constraint, and from which we also

can obtain the eigenvectors that are occupied. Next, we use the occupied eigenvectors to obtain a new set of r and λ via

$$\tilde{r}_i = \sqrt{1 - \frac{1}{n_{sub}} \frac{1}{N_{cell}} \sum'_{n,\mathbf{k}} \sum_{\alpha,\sigma} |u_{n,\mathbf{k}}^{f,\alpha,\sigma}|^2}, \quad (\text{S32})$$

$$\tilde{\lambda}_i = \frac{-V}{\tilde{r}_i \cdot n_{sub}} \frac{1}{N_{cell}} \text{Re} \left(\sum'_{n,\mathbf{k}} \sum_{\alpha,\sigma} (u_{n,\mathbf{k}}^{c,\alpha,\sigma})^* u_{n,\mathbf{k}}^{f,\alpha,\sigma} \right). \quad (\text{S33})$$

Note that since the value of λ depends on r , one may also obtain $\tilde{\lambda}_i$ via

$$\tilde{\lambda}_i = \frac{-V}{r_i \cdot n_{sub}} \frac{1}{N_{cell}} \text{Re} \left(\sum'_{n,\mathbf{k}} \sum_{\alpha,\sigma} (u_{n,\mathbf{k}}^{c,\alpha,\sigma})^* u_{n,\mathbf{k}}^{f,\alpha,\sigma} \right), \quad (\text{S34})$$

using r_i instead of \tilde{r}_i . We then check if μ_{i+1} , \tilde{r}_i , and $\tilde{\lambda}_i$ are close enough to μ_i , r_i , and λ_i with certain convergent criteria, which may differ from systems to systems. If yes, then the iteration stops and $(\mu_{i+1}, \tilde{r}_i, \tilde{\lambda}_i)$ is the final result of (μ, r, l) . If not, we perform a mixing and obtain

$$r_{i+1} = (1 - \gamma)r_i + \gamma\tilde{r}_i, \quad (\text{S35})$$

$$\lambda_{i+1} = (1 - \gamma)\lambda_i + \gamma\tilde{\lambda}_i, \quad (\text{S36})$$

and proceed to the next $(i + 1)^{\text{th}}$ iteration step using the updated parameters $(\mu_{i+1}, r_{i+1}, \lambda_{i+1})$. The parameter γ controls how smoothly we would like r and l to be updated. For example, one may choose $\gamma = 0.2$ to ensure that r_{i+1} and λ_{i+1} do not deviate significantly from r_i and λ_i . The iteration will continue until the convergence is reached.

Once the convergence is reached, we use the final results of μ , r , λ to construct $[H_{eff}(\mathbf{k})]$. The eigen-spectrum of this $[H_{eff}(\mathbf{k})]$ is the excitation spectrum of the periodic Anderson model solved using the parton saddle-point calculation. In Supplementary Table S5 we provide the parton saddle-point parameters that we obtain self-consistently for our periodic Anderson models.

As a recap, we have made use of the following assumptions in the derivation and practical implementation of the parton saddle-point calculation. First, we assume that both the c and f electrons carry the same labels \mathbf{R} , α , and σ . Second, we assume that both the c and f electrons are s orbitals (or other orbitals) such that an isotropic hybridization between them is symmetry-allowed. Third, we assume that all the sub-lattices are related to each other by some symmetries in the space group. Fourth, we assume that the mean-field solution preserves the original space group symmetry of the interacting Hamiltonian. Fifth, we assume that the model is solved with the periodic boundary condition and with finite number of unit cells.

Model's Space Group	E_f	V	μ	r	λ
no. 173 ($P6_3$)	-30.0	20.0	-19.09	0.5378	16.802
no. 176 ($P6_3/m$)	-30.0	20.0	-20.06	0.5692	16.400
no. 180 ($P6_222$)	-4.0	2.0	-3.00	0.5730	1.5048
no. 190 ($P\bar{6}2c$)	-6.0	3.0	-5.00	0.6281	1.8523

Supplementary Table S5. Parton saddle-point parameters μ , r , λ obtained self-consistently for our hexagonal periodic Anderson models with space groups no. 173 ($P6_3$), no. 176 ($P6_3/m$), no. 180 ($P6_222$), and no. 190 ($P\bar{6}2c$). All parameters except r are in unit of nearest hopping amplitude t .

Supplementary Note 3. EXTENDED RESULT FOR THE ANDERSON LATTICE MODEL WITH THE CHIRAL SPACE GROUP NO. 173

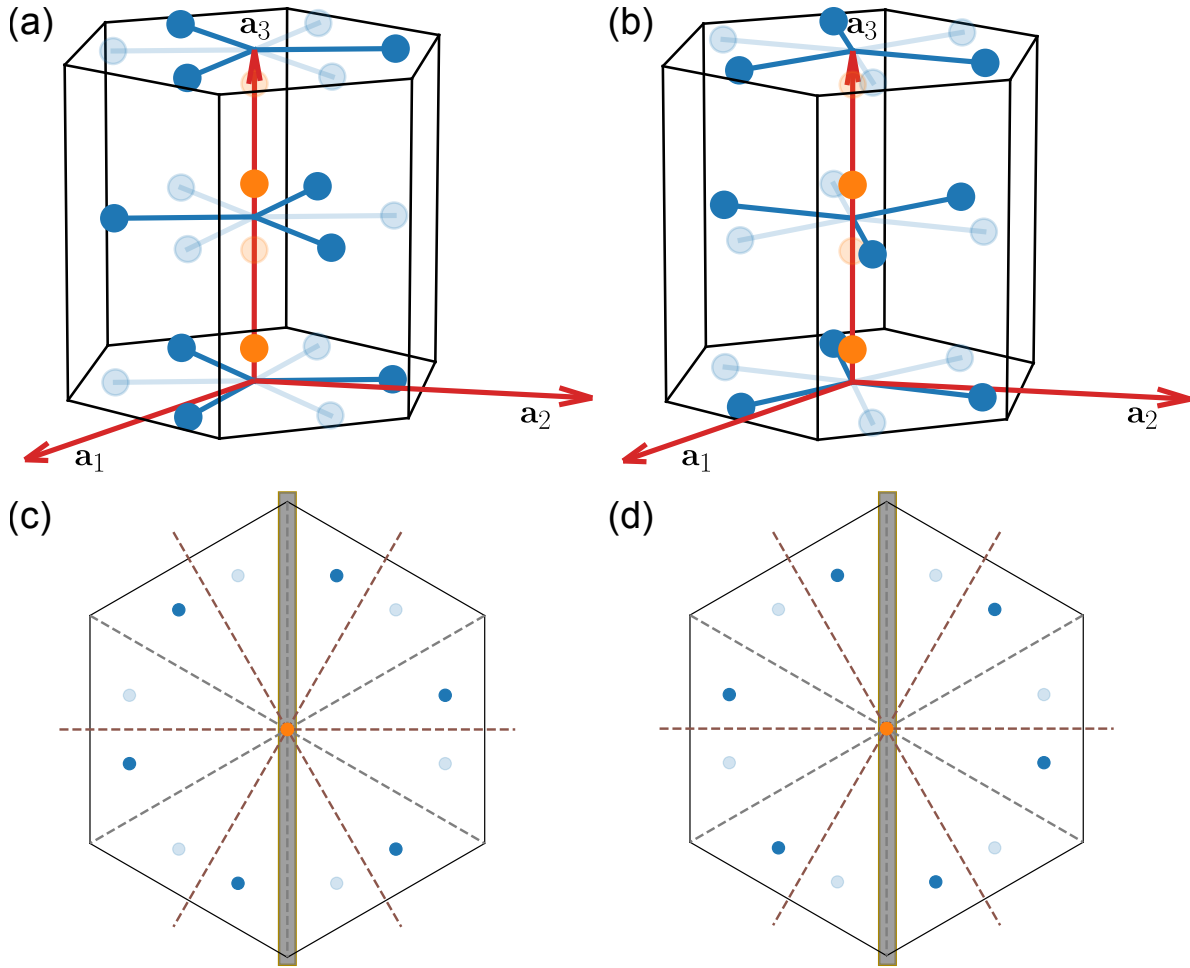
We now describe the space-group symmetries of the hexagonal space groups and provide extended results for the corresponding models that are shown in the main text.

The chiral hexagonal space group $P6_3$ is generated by the hexagonal lattice translations and the screw rotation symmetry $\{C_{6z}|0, 0, 1/2\}$. In Supplementary Fig. S1 we show how the chiral crystal in this group breaks inversion and mirror symmetries. Supplementary Fig. S1(a,c) and (b,d) correspond to crystals of opposite chiralities in this space group, and they are related by a mirror reflection symmetry.

In Supplementary Fig. S2(a) we show the low-energy heavy-fermion sector with a predominant f -electron character of the excitation spectrum of our hexagonal periodic Anderson model with the chiral space group no. 173 ($P6_3$). For this chiral WKSM phase, in Supplementary Fig. S2(b) we show the distribution of the hourglass-type heavy-fermion Weyl points in the 3D Brillouin zone (BZ) and their corresponding topological chiral charges, which take values of +3 and -1 verified using the numerical method in Supplementary Note 7.

Supplementary Note 4. EXTENDED RESULT FOR THE ANDERSON LATTICE MODEL WITH THE CHIRAL SPACE GROUP NO. 180

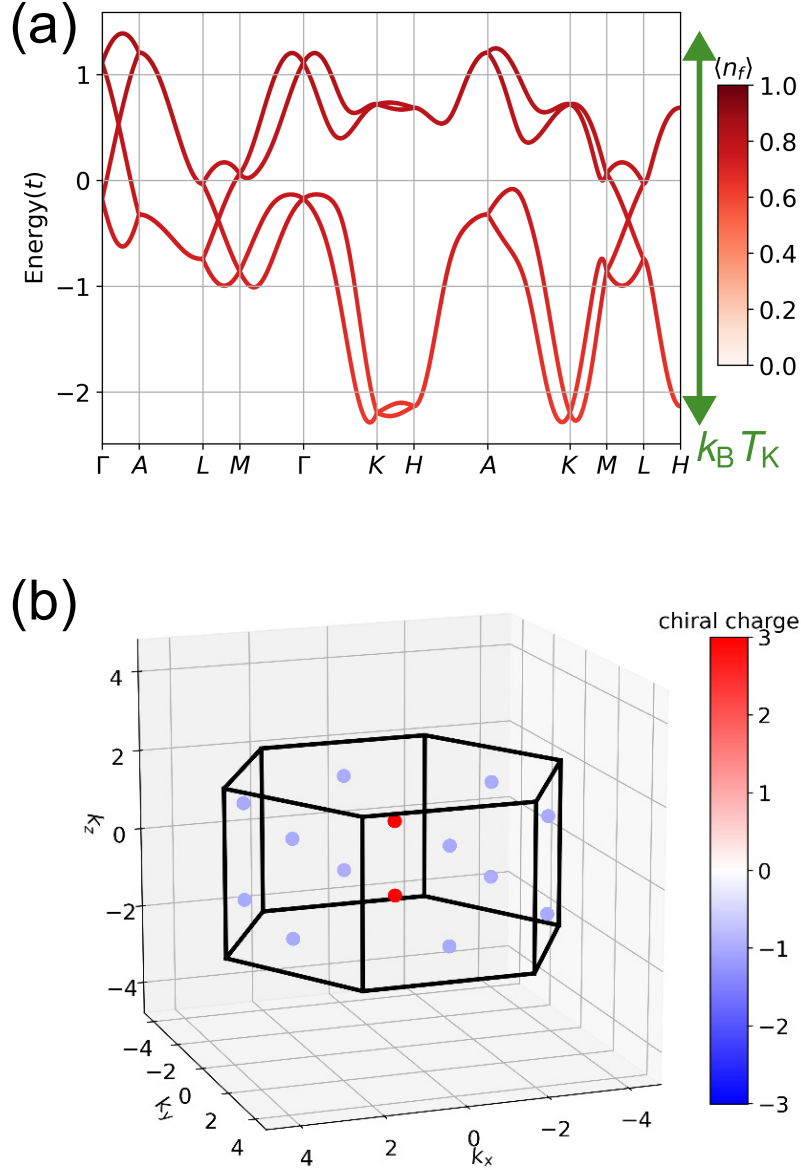
The chiral hexagonal space group $P6_222$ contains screw rotation $\{C_{6z}|0, 0, 1/3\}$ and two 180° rotations with rotation axes on the xy plane. In Supplementary Fig. S3(a,c) we show how the chiral crystal in this group breaks inversion and mirror symmetries. Supplementary Fig. S1(b,d)



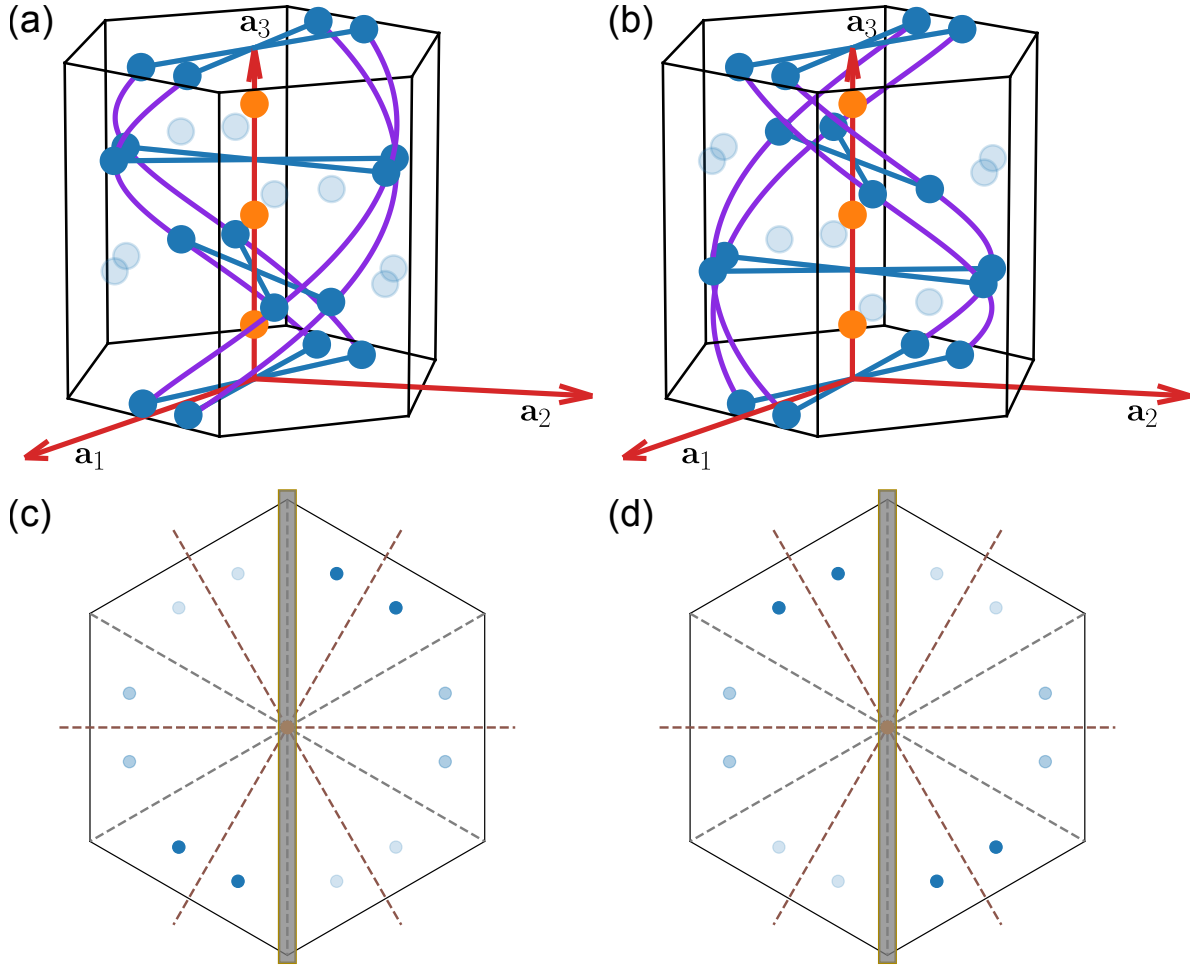
Supplementary Fig. S1. (a) Unit cell in chiral space group no. 173. Solid dots are the atoms and transparent dots are their inversion symmetric positions. If inversion is restored by placing atoms at these inversion-related positions, the space group symmetry rise to no. 176. (b) Unit cell in chiral space group no. 173 with mirrored atomic configuration of (a). (c) Top view of the unit cell in (a) showing broken mirror symmetries. Dashed lines indicate the potential mirror symmetries in hexagonal lattice. Solid dots are the atoms and transparent dots are their mirror symmetric positions. (d) Top view of (b). The mirror symmetry that maps between left panels with right panels is illustrated as the vertical gray bars in (c) and (d).

corresponds to the crystal of opposite chirality in space group no. 181, and it is related to the crystal in (a,c) by a mirror reflection symmetry.

In Supplementary Fig. S4, we show the Weyl points on the high-symmetry lines $\Gamma - A$ and $K - H$ in our periodic Anderson model with the chiral space group no. 180 ($P6_222$).



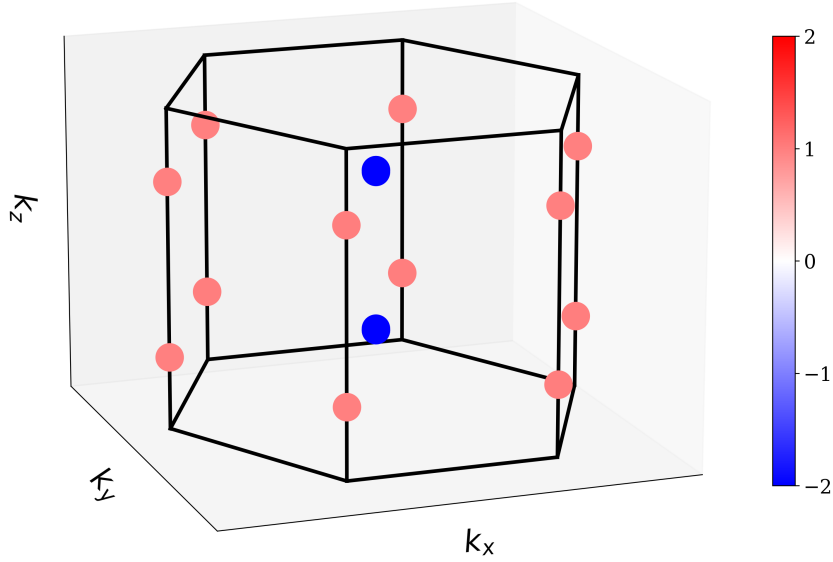
Supplementary Fig. S2. (a) The excitation spectrum of the hexagonal periodic Anderson model with space group no. 173 ($P6_3$). The Kondo scale $k_B T_K$ is also denoted. The color map indicates the portion of the f electron for a given excitation. Due to the presence of $\{C_{2z}\mathcal{T}|0, 0, 1/2\}$ symmetry, where \mathcal{T} is the spin-1/2 time-reversal operation, all the energy bands on the top or bottom BZ boundary [Fig. 1(b) in main text], *e.g.* along $A - L$ and $H - A$ high-symmetry lines, are twofold-degenerate. We also provide a derivation of such twofold degeneracy in Supplementary Note 9. (b) The distribution of hourglass-type Weyl points together with their topological charges (the color map) in the three-dimensional BZ. Due to the presence of spin-1/2 time-reversal symmetry, given a Weyl point at momentum \mathbf{k}_* with a topological charge C , there will be another Weyl point at momentum $-\mathbf{k}_*$ with the same topological charge C .



Supplementary Fig. S3. (a) Unit cell in chiral space group no. 180. Solid dots are the atoms and transparent dots are their inversion-related positions. Applying screw operation $\{C_{6z}|0, 0, \frac{1}{3}\}$ to atoms generates a right-handed trajectory. The violet curves represent this helical structure. (b) Unit cell in chiral space group no. 181. Applying screw operation $\{C_{6z}^{-1}|0, 0, \frac{1}{3}\}$ to atoms generates a left-handed trajectory, as illustrated by the violet curves. (c) Top view of the middle layer in (a) showing broken mirror symmetries. Dashed lines indicate the potential mirror symmetries in hexagonal lattice. Solid dots are the atoms and transparent dots are their mirror symmetric positions. (d) Top view of the middle layer in (b). The mirror symmetry that maps between left panels with right panels is illustrated as the vertical gray bars in (c) and (d).

Supplementary Note 5. ANDERSON LATTICE MODEL WITH THE ACHIRAL TOPOLOGICAL KONDO SEMIMETALS FOR THE ACHIRAL SPACE GROUP NO. 176

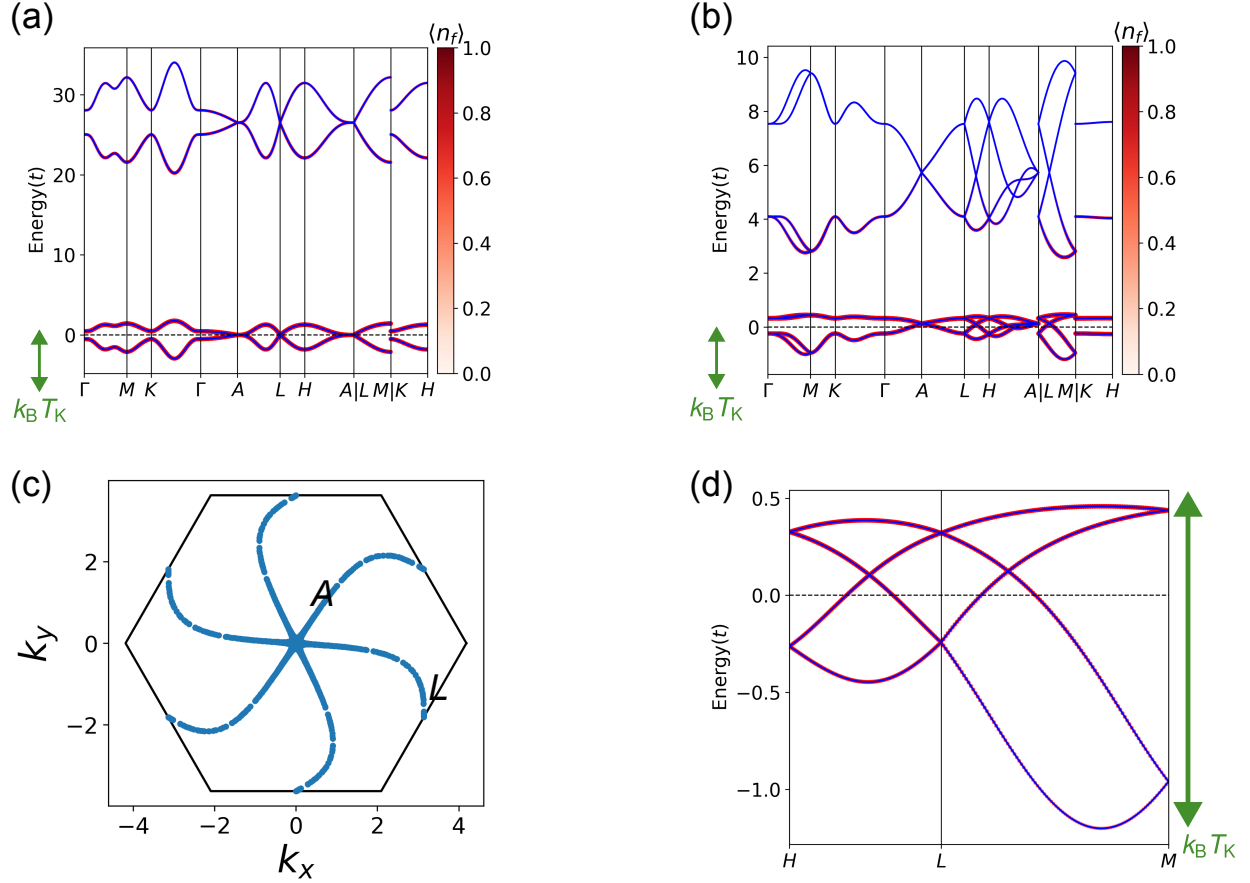
In the following section, we present model calculations for the two achiral space groups that are discussed in the main text.



Supplementary Fig. S4. Weyl points and their chiral charges in the hexagonal periodic Anderson model with space group no. 180 ($P6_222$).

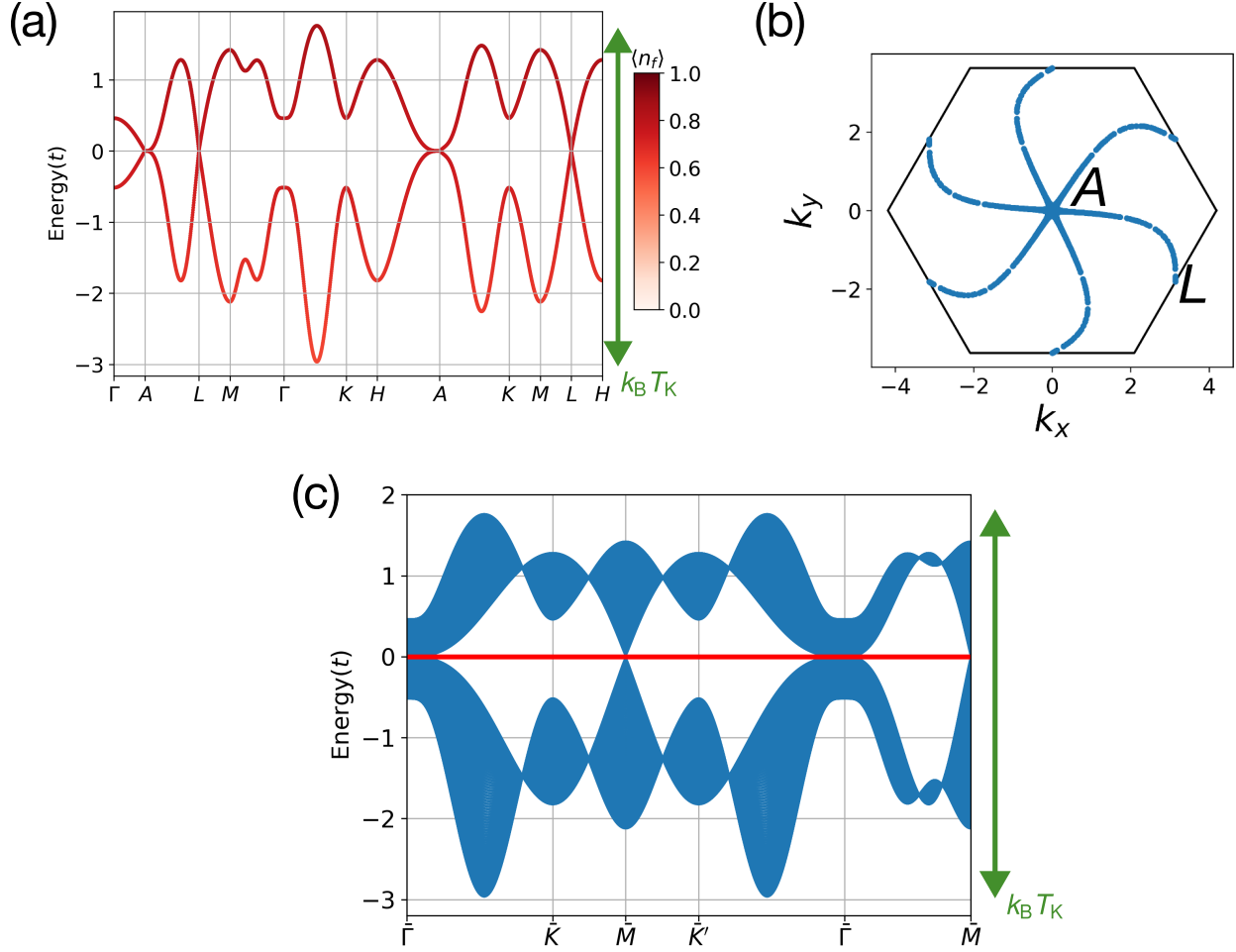
The achiral hexagonal space group $P6_3/m$ is generated by the hexagonal lattice translations, the screw rotation symmetry $\{C_{6z}|0, 0, 1/2\}$ and inversion symmetry. The excitation spectrum of the hexagonal periodic Anderson model with space group no. 176 ($P6_3/m$) is shown in Supplementary Fig. S5(a). In the low-energy heavy-fermion sector, the excitations have a predominant f -electron character. Due to the presence of inversion \mathcal{I} and spin-1/2 time-reversal \mathcal{T} symmetry, every band is twofold-degenerate. On the top (or bottom) BZ boundary, we identify fourfold-degenerate, *i.e.* Dirac, nodal lines forming a sixfold-symmetric pattern, as shown in Supplementary Fig. S5(b). In the Supplementary Note 8 and 9, we further derive the quantized non-Abelian Berry phases in space group $P6_3/m$ and show the existence of drumhead surface states^{35,36} bound by the Dirac nodal lines. We therefore demonstrate the Dirac-Kondo semimetal phase in the paramagnetic state of a system with the achiral hexagonal space group no. 176 ($P6_3/m$). We further emphasize that the Dirac-Kondo semimetal in the strongly-correlated setting serves as a vintage point to investigate the broad landscape of correlated topological phases by symmetry breaking¹⁵.

In Supplementary Fig. S6(a) we show the low-energy heavy-fermion sector of the excita-



Supplementary Fig. S5. (a) The excitation spectrum of the hexagonal periodic Anderson model with achiral space group no. 176 ($P6_3/m$) and (b) the excitation spectrum of the hexagonal periodic Anderson model with achiral space group no. 190 ($P\bar{6}2c$). The color map indicates the portion of the f electron for a given excitation. In (c) we show the Dirac nodal lines on the top (or bottom) BZ boundary corresponding to (a). In (d) we show the enlarged view of the band crossings consistent with the existence of low-energy heavy Weyl nodal lines in (b). The Kondo scale is denoted as T_K .

tion spectrum of our hexagonal periodic Anderson model with the achiral space group no. 176 ($P6_3/m$). The low-energy heavy-fermion sector has a predominant f -electron character. We also show the fourfold-degenerate, *i.e.* Dirac, nodal lines with a sixfold-symmetric pattern on the top (or bottom) BZ boundary in Supplementary Fig. S6(b). We further find that when the system is cut into a slab with a finite size along \mathbf{a}_3 , there are heavy-fermion surface states bound by the projected in-plane momenta of the Dirac nodal lines, as shown in Supplementary Fig. S6(c). These surface states could be established based on the quantized non-Abelian Berry phases in Supplementary Note 8.



Supplementary Fig. S6. (a) The excitation spectrum of the hexagonal periodic Anderson model with space group no. 176 ($P6_3/m$). The Kondo scale $k_B T_K$ is also denoted. The color map indicates the portion of the f electron for a given excitation. (b) The fourfold-degenerate, *i.e.* Dirac, nodal lines on the top or bottom boundary of the BZ [Fig. 1(b) in main text]. (c) The slab band structure demonstrating the existence of surface states bound by the projected momenta of the Dirac nodal lines. The bulk continuum is colored by blue and the surface states are colored by red.

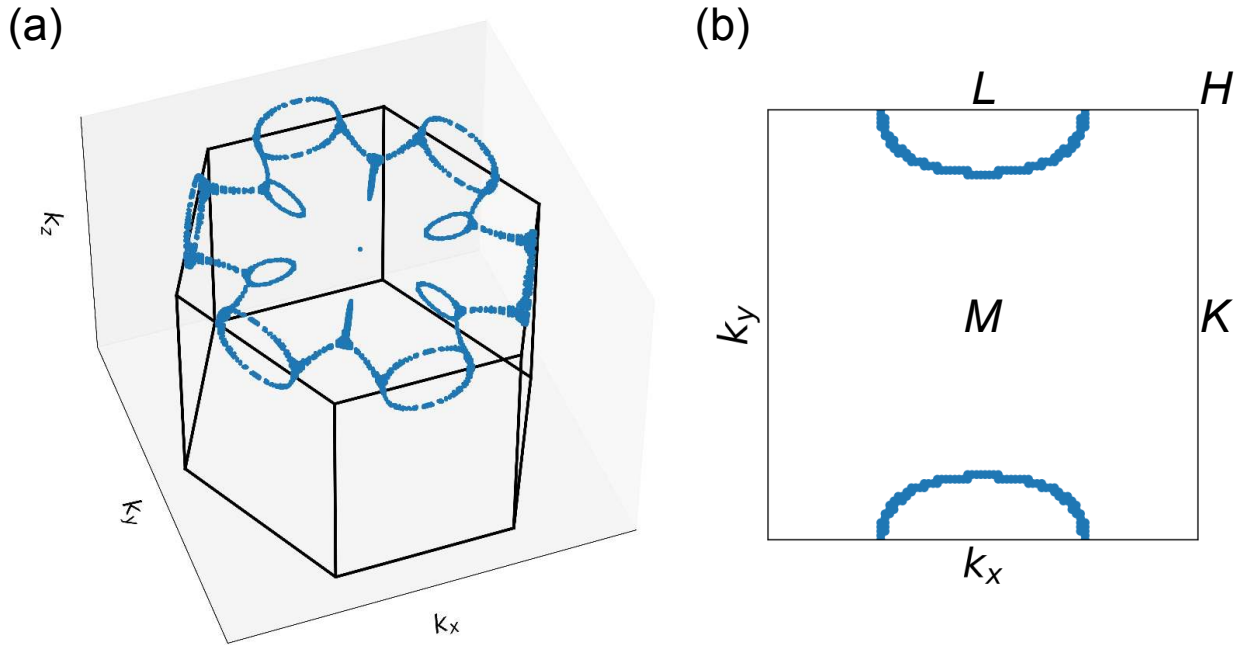
Supplementary Note 6. ACHIRAL TOPOLOGICAL KONDO SEMIMETALS FOR THE ACHIRAL SPACE GROUP NO. 190 ($P\bar{6}2c$)

The achiral hexagonal space group $P\bar{6}2c$ contains roto-inversion $C_{6z}\mathcal{I}$ and glide mirror symmetries such as $\{m_{1,-1,0}|0,0,1/2\}$, where $m_{1,-1,0}$ indicates the mirror reflection that flips the position-space vector $\mathbf{a}_1 - \mathbf{a}_2$.

The excitation spectrum of the periodic Anderson model with space group no. 190 ($P\bar{6}2c$) is

shown in Supplementary Fig. S5(c). The signature of the Weyl nodal line can be seen from the hourglass-type band crossing along $M - L$ in Supplementary Fig. S5(d)³⁰. Through the space-group symmetry, such symmetry-enforced Weyl nodal lines also appear on the other side-surfaces of the BZ.

In Supplementary Fig. S7(a), we show the Weyl nodal lines in our periodic Anderson model with the achiral space group no. 190 ($P\bar{6}2c$). There are three different Weyl nodal lines: (i) Weyl nodal lines on the BZ boundary containing M, L, K, H high-symmetry points, which are shown in Supplementary Fig. S7(b). They are enforced by the nonsymmorphic symmetries in this group. (ii) Weyl nodal lines on $k_3 = \pi$ plane, these are accidental crossings protected by $\{m_z|00\frac{1}{2}\}$. (iii) Weyl nodal lines on $k_1 = k_2$ plane, these are accidental crossings protected by the glide symmetry $\{m_{1\bar{1}0}|00\frac{1}{2}\}$. Interestingly, these three types of Weyl nodal lines coexist and are linked to each other in our model.



Supplementary Fig. S7. (a) Weyl nodal line in the excitation spectrum of our periodic Anderson model with space group no. 190 ($P\bar{6}2c$). (b) Symmetry enforced Weyl nodal line on the $M - K - H - L$ plane.

Supplementary Note 7. NUMERICAL METHODS FOR COMPUTING TOPOLOGICAL CHARGES OF WEYL POINTS

In this section, we provide the details of the two numerical methods and one symmetry indicator method that we use to compute the topological charges of Weyl points, which yield consistent results.

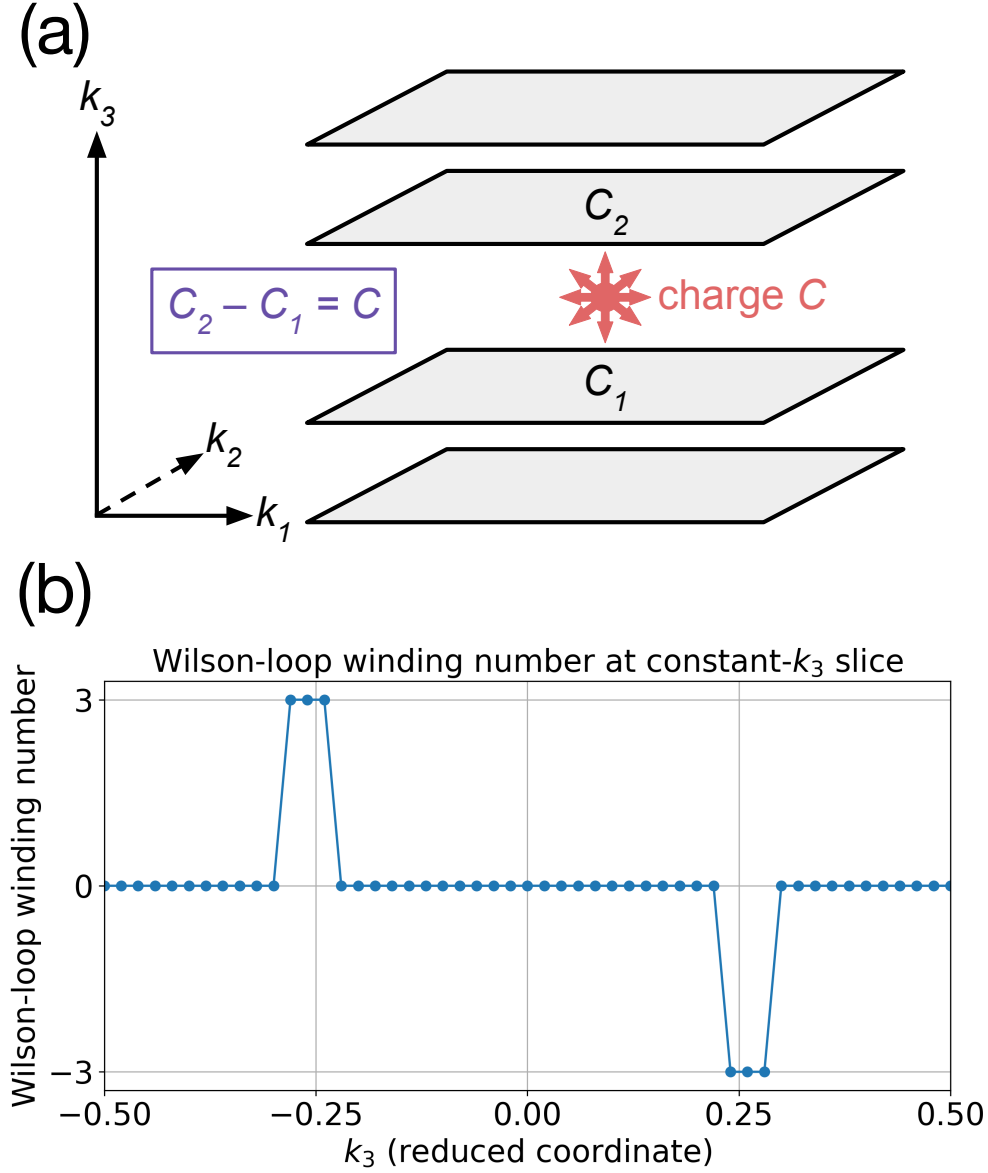
1. Discrete jump of Chern number

The Brillouin zone of a 3D system can be thought of as a collection of 2D planes in the (k_1, k_2) -momentum space with a constant k_3 value, where k_3 varies from -0.5 to 0.5 (in the reduced coordinate), see Supplementary Fig. S8. Provided that the energy gaps of the \mathbf{k} points on a 2D plane are opened, one could compute the Chern number of that 2D plane. Hence, one could evaluate the Chern number as a function of k_3 , as k_3 moves from -0.5 to 0.5 . Before and after the 2D plane passes through some \mathbf{k} points on which the energy gaps are closed, the Chern number of the 2D plane may experience a discrete change, see Supplementary Fig. S8. Specifically, the Chern number of a 2D plane in the momentum space can be computed as the winding number of the Wilson-loop spectrum.

In our hexagonal periodic Anderson model with space group no. 173 ($P6_3$), we have computed the Chern number for the lowest two bands as a function of k_3 in Supplementary Fig. S8, in which we identify various discrete jumps of magnitude 3. This is consistent with the distribution of the Weyl points in the 3D Brillouin zone in Supplementary Fig. S2, where there are three Weyl points with -1 chiral charge all on the same k_3 -constant plane, and there is one Weyl point with $+3$ chiral charge on another k_3 -constant plane.

2. Direct computation of Berry flux

In addition to using the discrete jump of the Chern number of 2D planes in the 3D Brillouin zone as the 2D plane slides through the entire 3D Brillouin zone to infer the topological charges of Weyl points, one could also compute the topological charge directly. This method usually requires that one already has an estimate about where the target Weyl point is located in the Brillouin zone, which can be done by (1) a numerical minimization procedure, or (2) an exhaustive search over grids in 3D Brillouin zone, to identify \mathbf{k} points with small gaps. The definition of the topological



Supplementary Fig. S8. (a) 3D Brillouin zone viewed as slices of 2D planes. If there is a Weyl point with topological charge C between two constant- k_3 planes, then the Chern numbers of the two planes will differ by C . (b) Chern number (Wilson-loop winding number) as a function of k_3 for our hexagonal periodic Anderson model with space group no. 173 ($P6_3$). There are discrete jumps of magnitude 3 which are consistent with the presence of (i) a single Weyl point carrying a topological charge of +3 and (ii) three Weyl points with the same k_3 coordinate and each carrying a topological charge of -1.

charge for a Weyl point is through a surface integral

$$C = \frac{1}{2\pi} \int_S d^2\mathbf{k} \cdot \boldsymbol{\Omega}(\mathbf{k}), \quad (\text{S37})$$

where S is the surface enclosing the Weyl point and $\Omega(\mathbf{k})$ is the Berry curvature. Such a surface integral over a closed surface S with the Berry curvature being the integrand yields the total Berry flux emitted by the Weyl point enclosed by the surface S . In order to compute this integral, one could enclose the target Weyl point by a cube, divide the surfaces of the cube into small plaquettes, compute and sum over the Berry phases for all the small plaquettes.

Suppose we sort the band index n for a given \mathbf{k} via $E_{n,\mathbf{k}} \leq E_{n+1,\mathbf{k}}$ with $n = 1$ being the lowest-energy band index. In our hexagonal periodic Anderson model with space group no. 173 ($P6_3$), using this method of direct computation we verify that the Weyl points (between $n = 2$ and $n = 3$ bands) located along the $\Gamma - A$ line each carries a topological chiral charge of $+3$, and that the Weyl points (between $n = 2$ and $n = 3$ bands) located along the $M - L$ line each carries a topological chiral charge of -1 , leading to Fig. 2 in the main text. We further verify that exactly at the time-reversal-invariant momenta Γ and M the Kramers degeneracies (between $n = 1$ and $n = 2$ bands) are in fact Kramers-Weyl points carrying a topological chiral charge of -1 and $+1$, respectively.

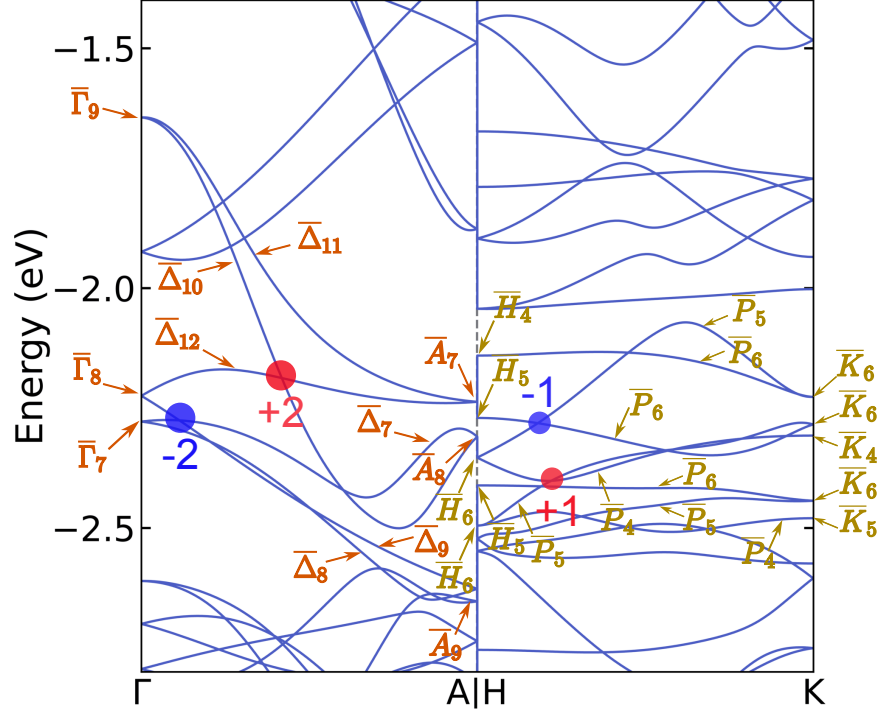
3. Symmetry indicator for chiral charges

Symmetry eigenvalues of the Bloch states at the band crossing point can be used to determine the chiral charge of a Weyl point³². We adopt this method to determine the chiral charges of the Weyl points in the DFT band structure of CePt₂B. CePt₂B has the chiral space group $P6_222$ that contains the screw symmetry $\{C_{6z}|0, 0, 1/3\}$. Along the $\Gamma - A$ high-symmetry line, we could label the Bloch state by its $\{C_{6z}|0, 0, 1/3\}$ eigenvalue, which is $\exp(i\frac{\pi}{3}j_z + ik_z/3)$, with $j_z = \frac{1}{2}, \frac{3}{2}, \frac{5}{2}, -\frac{5}{2}, -\frac{3}{2}, -\frac{1}{2}$. This corresponds to the irreducible representation (irrep) labels $\overline{\Delta}_{11}, \overline{\Delta}_8, \overline{\Delta}_9, \overline{\Delta}_{12}, \overline{\Delta}_7, \overline{\Delta}_{10}$, respectively. Along the $K - H$ high-symmetry line, we could label the Bloch state by its $\{C_{3z}|0, 0, 2/3\}$ eigenvalue, which is $\exp(i\frac{\pi}{3}j_z + 2ik_z/3)$, with $j_z = \frac{1}{2}, \frac{3}{2}, -\frac{1}{2}$. This corresponds to the irreducible representation labels $\overline{P}_6, \overline{P}_4, \overline{P}_5$, respectively.

The crossing of two irreps at $k_0 = (0, 0, k_z)$ ($\Gamma - A$) or $k_0 = (\frac{1}{3}, \frac{1}{3}, k_z)$ ($K - H$) with $j_z(k_0 - \delta k_z)$ and $j_z(k_0 + \delta k_z)$ has Weyl charge³²

$$C = j_z(k_0 + \delta k_z) - j_z(k_0 - \delta k_z) \quad (\text{S38})$$

In Supplementary Fig. S9, we label the DFT band structure of CePt₂B along $\Gamma - A$ by such irreducible representation labels. For example, there is a crossing point between the bands labeled



Supplementary Fig. S9. Irreps of CePt₂B DFT bands along high symmetry line Δ ($\Gamma - A$) and P ($K - H$).

as $\bar{\Delta}_{12}$ and $\bar{\Delta}_{10}$, meaning that these two bands carry $\{C_{6z}|0, 0, 1/3\}$ eigenvalues $j_z = -\frac{5}{2}$ and $j_z = -\frac{1}{2}$, respectively. Hence, the ratio between the $\{C_{6z}|0, 0, 1/3\}$ eigenvalues at this band crossing point is $2 \pmod 6$. The chiral charges of all other band crossings highlighted in Supplementary Fig. S9 are also determined in this way. We verify that the Weyl charges between given two adjacent band indices sum to zero.

Supplementary Note 8. QUANTIZED NON-ABELIAN BERRY PHASES IN SPACE GROUP NO. 176 ($P6_3/m$) WITH SPIN-1/2 TIME-REVERSAL SYMMETRY

In this section, we show that a crystalline system with space group no. 176 ($P6_3/m$) and spin-1/2 time-reversal symmetry exhibits quantized non-Abelian Berry phases, which could be used to establish the presence of surface states when the corresponding hexagonal crystal is cut finite along the a_3 direction.

1. Derivation of quantized non-Abelian Berry phases

The modern development of electronic structure theory has established the connection between Berry phase and electronic polarization, which is closely related to the presence of surface states and surface charges. For our multi-band hexagonal crystal systems, we define the k_3 -directed Wilson-loop matrix $[\mathcal{W}_{k_1, k_2}^{\mathbf{G}_3}]$ whose matrix elements are given by (see Supplementary Fig. S10 for a schematic diagram of $[\mathcal{W}_{k_1, k_2}^{\mathbf{G}_3}]$)

$$[\mathcal{W}_{k_1, k_2}^{\mathbf{G}_3}]_{mn} = \langle u_{m, \mathbf{k} + \mathbf{G}_3} | \left(\prod_{\mathbf{q}}^{(\mathbf{k} + \mathbf{G}_3 \leftarrow \mathbf{k})} [P(\mathbf{q})] \right) | u_{n, \mathbf{k}} \rangle, \quad (\text{S39})$$

where $[P(\mathbf{k})]$ is the matrix projection operator onto the vector space spanned by the N_{occ} occupied eigenvectors of the Bloch Hamiltonian matrix, namely

$$[P(\mathbf{k})] = \sum_{n \in occ} |u_{n, \mathbf{k}}\rangle \langle u_{n, \mathbf{k}}|, \quad (\text{S40})$$

and $|u_{n, \mathbf{k}}\rangle$ is the eigenvector of the Bloch Hamiltonian matrix. Specifically, the eigenvector $|u_{n, \mathbf{k}}\rangle$ satisfies the periodic gauge such that $|u_{n, \mathbf{k} + \mathbf{G}}\rangle = [V(\mathbf{G})]^{-1} |u_{n, \mathbf{k}}\rangle = [V(\mathbf{G})]^\dagger |u_{n, \mathbf{k}}\rangle$. For the case of our effective Bloch Hamiltonian matrix $[H_{eff}(\mathbf{k})]$ in the auxiliary-boson representation at the saddle-point level we have

$$[V(\mathbf{G})] = \begin{pmatrix} [\tilde{V}(\mathbf{G})] & 0 \\ 0 & [\tilde{V}(\mathbf{G})] \end{pmatrix}, \quad (\text{S41})$$

with $[\tilde{V}(\mathbf{G})]_{(\alpha, \sigma), (\alpha', \sigma')} = e^{i\mathbf{G} \cdot \mathbf{r}_\alpha} \delta_{\alpha, \alpha'} \delta_{\sigma, \sigma'}$. The eigenspectrum of $[\mathcal{W}_{k_1, k_2}^{\mathbf{G}_3}]$ takes the unimodular form $e^{i\gamma_j(k_1, k_2)}$ for $j = 1 \dots N_{occ}$. The eigenphases $\gamma_j(k_1, k_2) \in \mathbb{R}$, also known as the non-Abelian Berry phases, are well-defined module 2π . Importantly, $\frac{\gamma_j(k_1, k_2)}{2\pi} \mathbf{a}_3$ is the localized position along \mathbf{a}_3 of the hybrid Wannier function localized along \mathbf{a}_3 while extended along \mathbf{a}_1 and \mathbf{a}_2 . Intuitively, one could think of the eigenphases $\gamma_j(k_1, k_2)$ of the Wilson-loop matrix $[\mathcal{W}_{k_1, k_2}^{\mathbf{G}_3}]$ as equivalent to the position along \mathbf{a}_3 as a function of the remaining momentum components (k_1, k_2) . Hence, the symmetry transformation properties of the set of eigenphases $\{\gamma_j(k_1, k_2) \mid j = 1 \dots N_{occ}\}$ can be derived as follows, by using the fact that γ_j transforms in the same manner as the position along \mathbf{a}_3 .

We recall here that space group no. 176 ($P6_3/m$) contains inversion symmetry \mathcal{I} , screw rotation symmetry $\{C_{6z} | 0, 0, 1/2\}$, and we also assume spin-1/2 time-reversal symmetry \mathcal{T} . For spin-1/2 time-reversal symmetry \mathcal{T} , which flips the momentum while leaving the position invariant, we

have the symmetry constraint

$$\begin{aligned} & \{\gamma_j(k_1, k_2) \mid j = 1 \dots N_{occ}\} \\ & = \{\gamma_j(-k_1, -k_2) \mid j = 1 \dots N_{occ}\}. \end{aligned} \quad (\text{S42})$$

Hereafter, the equality between the set of eigenphases is well-defined module 2π . For inversion symmetry \mathcal{I} , which flips both the momentum and position, we have the symmetry constraint

$$\begin{aligned} & \{\gamma_j(k_1, k_2) \mid j = 1 \dots N_{occ}\} \\ & = \{-\gamma_j(-k_1, -k_2) \mid j = 1 \dots N_{occ}\}. \end{aligned} \quad (\text{S43})$$

For $\{C_{6z}|0, 0, 1/2\}$ symmetry, which rotates the momentum by C_{6z} , and rotates the position by C_{6z} followed by a fractional translation $\frac{1}{2}\mathbf{a}_3$, we have the symmetry constraint

$$\begin{aligned} & \{\gamma_j(k_1, k_2) + \pi \mid j = 1 \dots N_{occ}\} \\ & = \{\gamma_j(C_{6z}(k_1, k_2)) \mid j = 1 \dots N_{occ}\}, \end{aligned} \quad (\text{S44})$$

where the $+\pi$ on the left-hand side is due to the fractional translation $\frac{1}{2}\mathbf{a}_3$.

Our goal in below would be to combine the above symmetry constraints such that we obtain a set of constraints for $\{\gamma_j(k_1, k_2) \mid j = 1 \dots N_{occ}\}$ right on the same momentum (k_1, k_2) . From \mathcal{T} and $\{C_{6z}|0, 0, 1/2\}$ symmetries, we can derive

$$\begin{aligned} & \{\gamma_j(k_1, k_2) \mid j = 1 \dots N_{occ}\} \\ & = \{\gamma_j(-k_1, -k_2) \mid j = 1 \dots N_{occ}\} \\ & = \{\gamma_j(C_{6z}^3(k_1, k_2)) \mid j = 1 \dots N_{occ}\} \\ & = \{\gamma_j(C_{6z}^2(k_1, k_2)) + \pi \mid j = 1 \dots N_{occ}\} \\ & = \{\gamma_j(C_{6z}(k_1, k_2)) + 2\pi \mid j = 1 \dots N_{occ}\} \\ & = \{\gamma_j(k_1, k_2) + 3\pi \mid j = 1 \dots N_{occ}\}, \end{aligned} \quad (\text{S45})$$

which means

$$\begin{aligned} & \{\gamma_j(k_1, k_2) \mid j = 1 \dots N_{occ}\} \\ & = \{\gamma_j(k_1, k_2) + \pi \mid j = 1 \dots N_{occ}\}. \end{aligned} \quad (\text{S46})$$

This means that the set of eigenphases at any momentum (k_1, k_2) must be equal to (up to a module of 2π) itself plus π . Going further, we define the summed Berry phase as

$$\gamma(k_1, k_2) \equiv \sum_{j=1}^{N_{occ}} \gamma_j(k_1, k_2) \pmod{2\pi}. \quad (\text{S47})$$

From the symmetry constraints $\{\gamma_j(k_1, k_2) \mid j = 1 \dots N_{occ}\} = \{\gamma_j(k_1, k_2) + \pi \mid j = 1 \dots N_{occ}\}$ we first obtain the following result

$$\gamma(k_1, k_2) = \gamma(k_1, k_2) + \pi N_{occ} \pmod{2\pi}. \quad (\text{S48})$$

We can then deduce that N_{occ} can not be equal to an odd integer. This means that the Wilson loop matrix $[\mathcal{W}_{k_1, k_2}^{\mathbf{G}_3}]$ is only well-defined when N_{occ} is equal to an even integer, otherwise there is a contradiction. Hence, in the following derivation of quantized Berry phases in space group no. 176 ($P6_3/m$) we only consider an even integer N_{occ} .

One could also derive the constraint of $\gamma_j(k_1, k_2)$ at the same momentum due to \mathcal{IT} symmetry. The presence of \mathcal{IT} symmetry is guaranteed since both \mathcal{I} and \mathcal{T} are symmetries of the system. Note that $(\mathcal{IT})^2 = -1$ since $(\mathcal{IT})^2 = \mathcal{ITIT} = \mathcal{IIT\mathcal{T}} = \mathcal{I}^2\mathcal{T}^2 = -1$ due to $\mathcal{I}^2 = 1$ and $\mathcal{T}^2 = -1$. By combining the constraints from \mathcal{I} and \mathcal{T} symmetries we have

$$\{\gamma_j(k_1, k_2) \mid j = 1 \dots N_{occ}\} \quad (\text{S49})$$

$$= \{-\gamma_j(-k_1, -k_2) \mid j = 1 \dots N_{occ}\} \quad (\text{S50})$$

$$= \{-\gamma_j(k_1, k_2) \mid j = 1 \dots N_{occ}\}. \quad (\text{S51})$$

Hence, \mathcal{IT} symmetry leads to the constraint

$$\begin{aligned} & \{\gamma_j(k_1, k_2) \mid j = 1 \dots N_{occ}\} \\ & = \{-\gamma_j(k_1, k_2) \mid j = 1 \dots N_{occ}\}, \end{aligned} \quad (\text{S52})$$

which means that the summed Berry phase satisfies

$$\gamma(k_1, k_2) = -\gamma(k_1, k_2) \pmod{2\pi} \quad (\text{S53})$$

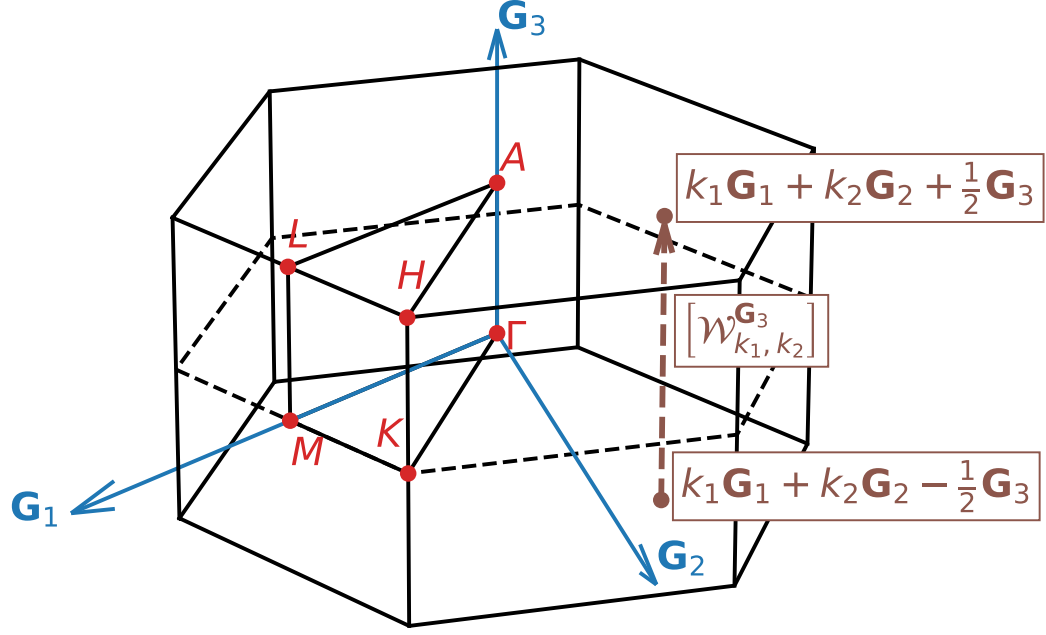
such that

$$\gamma(k_1, k_2) = n\pi \quad (\text{S54})$$

where $n \in \mathbb{Z}$. From $(\mathcal{IT})^2 = -1$, the Kramers theorem further implies that for a fixed (k_1, k_2) if there is an eigenphase γ , there will be another independent eigenphase $-\gamma$. In other words, $(\mathcal{IT})^2 = -1$ means that the eigenphases must form pairs of the form $\{-\gamma, \gamma\}$.

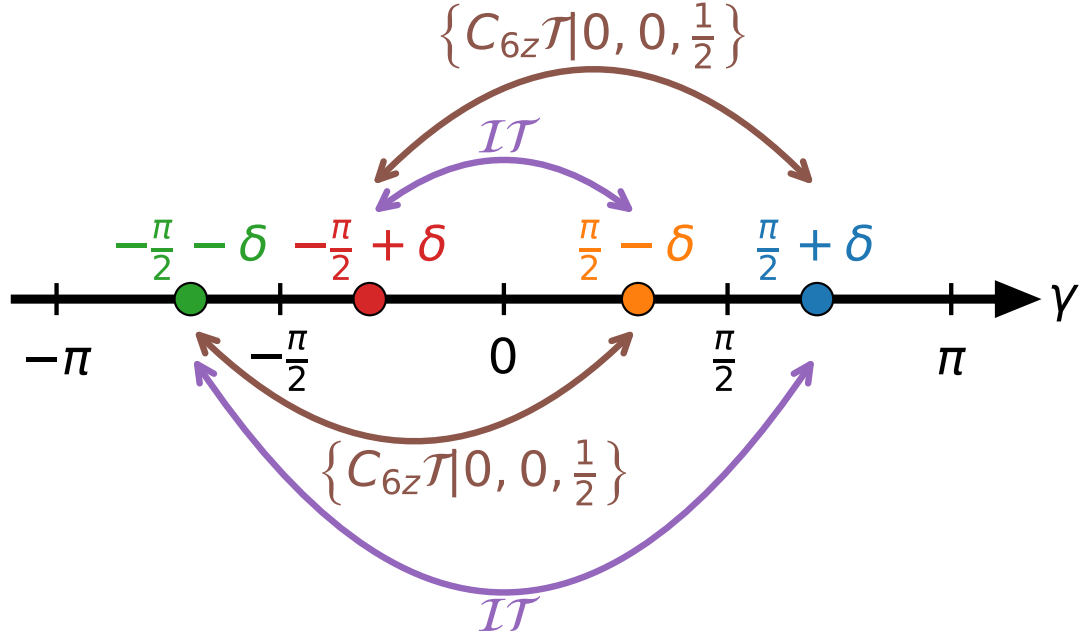
We could now combine all the constraints derived above and obtain

$$\begin{aligned} & \{\gamma_j(k_1, k_2) \mid j = 1 \dots N_{occ}\} \\ & = \{\gamma_j(k_1, k_2) + \pi \mid j = 1 \dots N_{occ}\} \\ & = \{-\gamma_j(k_1, k_2) \mid j = 1 \dots N_{occ}\}, \end{aligned} \quad (\text{S55})$$



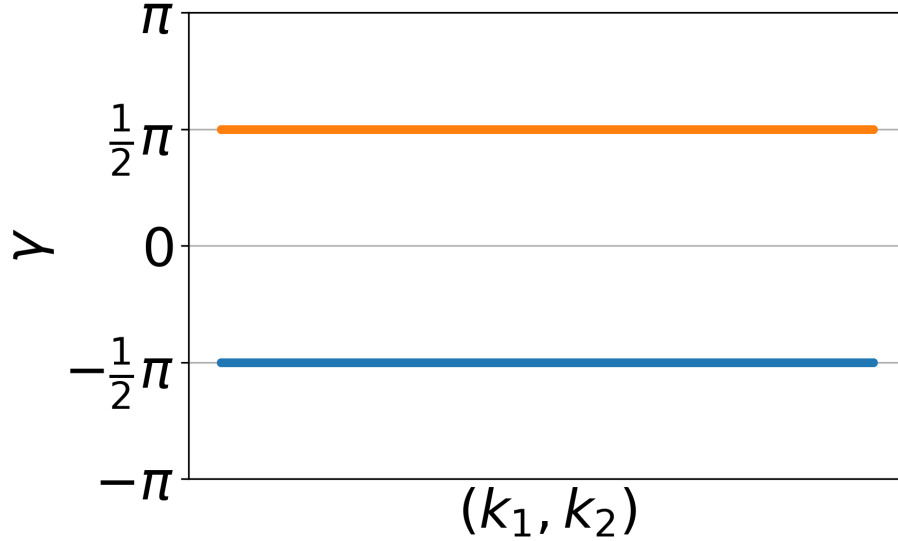
Supplementary Fig. S10. Schematic diagram of the Wilson loop $[\mathcal{W}_{k_1, k_2}^{\mathbf{G}_3}]$ for a non-contractible loop (the dashed arrow) in the Brillouin zone from \mathbf{k} to $\mathbf{k} + \mathbf{G}_3$. This Wilson loop $[\mathcal{W}_{k_1, k_2}^{\mathbf{G}_3}]$ is used to derive the quantized non-Abelian Berry phases in the space group no. 176 ($P6_3/m$) with the spin-1/2 time-reversal symmetry \mathcal{T} .

together with the constraint that eigenphases must form pairs of the form $\{-\gamma, \gamma\}$. Supplementary Fig. S11 demonstrates the most generic distribution of the eigenphases $\gamma_j(k_1, k_2)$ at a specific momentum (k_1, k_2) due to the above symmetry constraints and how each eigenphase is related to the other by a certain symmetry, including \mathcal{IT} and $\{C_{6z}\mathcal{T}|0, 0, 1/2\}$. Although Supplemen-



Supplementary Fig. S11. The most generic distribution of the Wilson-loop eigenphases $\gamma_j(k_1, k_2)$ at a specific momentum (k_1, k_2) from the symmetry constraints of the space group no. 176 ($P6_3/m$) with the spin-1/2 time-reversal symmetry \mathcal{T} . Starting from a generic value of the k_3 -directed Wilson-loop eigenphase $\frac{\pi}{2} + \delta$ at a specific momentum (k_1, k_2) , the \mathcal{IT} symmetry guarantees that $-\frac{\pi}{2} - \delta$ is also a k_3 -directed Wilson-loop eigenphase at the same momentum (k_1, k_2) . Building on this, the $\{C_{6z}\mathcal{T}|0, 0, 1/2\}$ symmetry further guarantees that $-\frac{\pi}{2} + \delta$ and $\frac{\pi}{2} - \delta$ are also k_3 -directed Wilson-loop eigenphases at the same momentum (k_1, k_2) .

tary Fig. S11 tentatively shows eigenphases $-\frac{\pi}{2} - \delta$, $-\frac{\pi}{2} + \delta$, $\frac{\pi}{2} - \delta$, and $\frac{\pi}{2} + \delta$ on the general ground at a specific momentum (k_1, k_2) , we emphasize that it is possible that the set of eigenphases only contains two elements as $\{-\frac{\pi}{2}, \frac{\pi}{2}\}$, because $\{-\frac{\pi}{2}, \frac{\pi}{2}\}$ still satisfies all the above symmetry constraints. Specifically, this is consistent with the case where $\delta = 0$, and is the only case satisfying all the symmetry constraints when the number of eigenphases is equal to 2. Hence, we note here that if $N_{occ} = 2$, then $\{\gamma_j(k_1, k_2) \mid j = 1, 2\}$ must equal $\{-\frac{\pi}{2}, \frac{\pi}{2}\}$ and is (k_1, k_2) -independent. On the other hand, when $N_{occ} = 4$, we will have $\{\gamma_j(k_1, k_2) \mid j = 1 \dots 4\} = \{-\frac{\pi}{2} - \delta(k_1, k_2), -\frac{\pi}{2} + \delta(k_1, k_2), \frac{\pi}{2} - \delta(k_1, k_2), \frac{\pi}{2} + \delta(k_1, k_2)\}$ where $\delta(k_1, k_2)$ is (k_1, k_2) -dependent. Based on Supplementary Fig. S11, we conclude that when $N_{occ} = 2 \times$ an odd integer there must



Supplementary Fig. S12. Non-Abelian Berry phase (k_3 -directed Wilson-loop) spectrum as a function of (k_1, k_2) for the lowest two bands in the low-energy sector of the excitation spectrum for our hexagonal periodic Anderson model with space group no. 176 ($P6_3/m$). (k_1, k_2) points are sampled uniformly in the 2D BZ. Importantly, we remove the results of non-Abelian Berry phase when $(k_1, k_2) = (0, 0)$, $(0.5, 0)$, $(0, 0.5)$ and $(0.5, 0.5)$ in the reduced coordinate, since their k_3 -directed Wilson loops pass through the Dirac nodal line, making the corresponding Wilson loop matrices ill-defined. After removing those (k_1, k_2) points that make the k_3 -directed Wilson loop matrices ill-defined, we see that the non-Abelian Berry phase spectrum contains only values of $-\frac{\pi}{2}$ and $\frac{\pi}{2}$.

be two non-Abelian Berry phases (out of the in total N_{occ} eigenphases) taking values of (k_1, k_2) -independent $\{-\frac{\pi}{2}, \frac{\pi}{2}\}$, while when $N_{occ} = 2 \times$ an even integer then all N_{occ} non-Abelian Berry phases are in general not quantized and (k_1, k_2) -dependent.

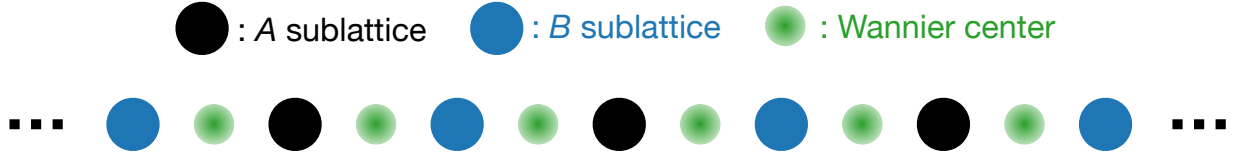
As a final remark, we note that a system with space group no. 176 ($P6_3/m$) and spin-1/2 time-reversal symmetry must have fourfold degenerate nodal lines at the top (or equivalently the bottom) boundary of the BZ³⁰. Hence, when the occupied space and (k_1, k_2) are chosen such that the path going from \mathbf{k} to $\mathbf{k} + \mathbf{G}_3$ in the definition of the Wilson loop matrix passes through gap-closing points from the fourfold degenerate nodal lines, then the Wilson loop matrix is no longer well-defined, as it requires that the matrix projection operator is well-defined along the path. In such a situation, the non-Abelian Berry phases can not be obtained. Our above results hence apply to the situation when the Wilson loop matrix is well-defined. In Supplementary Fig. S12, we

numerically demonstrate the quantized non-Abelian Berry phases $\{-\frac{\pi}{2}, \frac{\pi}{2}\}$ we derived above.

2. Surface states from Wannier centers

In this section, we illustrate how the quantized non-Abelian Berry phases with values $-\frac{\pi}{2}$ and $\frac{\pi}{2}$ in space group no. 176 ($P6_3/m$) with spin-1/2 time-reversal symmetry could be used to establish the presence of surface states.

When a hexagonal crystal structure is cut into finite size along \mathbf{a}_3 , the resulting finite-size slab is still extended along \mathbf{a}_1 and \mathbf{a}_2 . Hence, the BZ of the slab structure is specified by (k_1, k_2) . Let us specifically focus on a given value of (k_1, k_2) , at which the Bloch Hamiltonian of the slab describes an effective 1D system finite along \mathbf{a}_3 . The eigenphases of the Wilson-loop matrix $[\mathcal{W}_{k_1, k_2}^{\mathbf{G}_3}]$ are then the non-Abelian Berry phases of that effective 1D system, and hence specifies where its Wannier centers are located. With this in mind, we can now explore the consequence of the (k_1, k_2) -independent Wilson-loop eigenphases $\{-\frac{\pi}{2}, \frac{\pi}{2}\}$. For simplicity, we will specialize to the case where the number of occupied bands is 2 and the system contains two sub-lattices, one at $\mathbf{0}$ and the other at $\frac{1}{2}\mathbf{a}_3$. Our analysis will carry over to any (k_1, k_2) , provided that the occupied energy bands along (k_1, k_2, k_3) to $(k_1, k_2, k_3) + \mathbf{G}_3$ are gapped from the other bands such that the Wilson-loop matrix $[\mathcal{W}_{k_1, k_2}^{\mathbf{G}_3}]$ is well-defined. The set of non-Abelian Berry phases $\{-\frac{\pi}{2}, \frac{\pi}{2}\}$ of the effective 1D system means that the 1D Wannier centers are localized at $\{-\frac{1}{4}\mathbf{a}_3, \frac{1}{4}\mathbf{a}_3\}$. This means that the Wannier centers are always located between the two sub-lattices, as illustrated in Supplementary Fig. S13. Hence, when we cut the system into finite size along \mathbf{a}_3 , there is always a Wannier center that is exposed outside the sample, leading to the presence of boundary states. Such boundary states are then the surface states at momentum (k_1, k_2) where the $[\mathcal{W}_{k_1, k_2}^{\mathbf{G}_3}]$ is well-defined – namely those (k_1, k_2) points that do not correspond to the projected momenta of the fourfold-degenerate nodal line. From this, we can further state that such surface states are bound by the projected momenta of the fourfold-degenerate nodal line. We emphasize that this is a new type of drumhead surface state, as it is a consequence of the fourfold-degenerate (Dirac) nodal line.



as

$$\begin{aligned}
& \langle \psi_{k_1, k_2, 0.5} | \{C_{2z} \mathcal{T} | 0, 0, 1/2 \} \psi_{k_1, k_2, 0.5} \rangle \\
&= \langle \{C_{2z} \mathcal{T} | 0, 0, 1/2 \} \psi_{k_1, k_2, 0.5} | (\{C_{2z} \mathcal{T} | 0, 0, 1/2 \})^2 \psi_{k_1, k_2, 0.5} \rangle^* \\
&= \langle \{C_{2z} \mathcal{T} | 0, 0, 1/2 \} \psi_{k_1, k_2, 0.5} | \{E | 0, 0, 1 \} \psi_{k_1, k_2, 0.5} \rangle^* \\
&= -\langle \{C_{2z} \mathcal{T} | 0, 0, 1/2 \} \psi_{k_1, k_2, 0.5} | \psi_{k_1, k_2, 0.5} \rangle^* \\
&= -\langle \psi_{k_1, k_2, 0.5} | \{C_{2z} \mathcal{T} | 0, 0, 1/2 \} \psi_{k_1, k_2, 0.5} \rangle
\end{aligned} \tag{S56}$$

where we have used the fact that $\{C_{2z} \mathcal{T} | 0, 0, 1/2 \}$ is an anti-unitary symmetry,

$$\begin{aligned}
& (\{C_{2z} \mathcal{T} | 0, 0, 1/2 \})^2 \\
&= \{C_{2z} \mathcal{T} | 0, 0, 1/2 \} \{C_{2z} \mathcal{T} | 0, 0, 1/2 \} \\
&= \{C_{2z} \mathcal{T} C_{2z} \mathcal{T} | 0, 0, 1 \} \\
&= \{(C_{2z})^2 \mathcal{T}^2 | 0, 0, 1 \} \\
&= \{\bar{E} \bar{E} | 0, 0, 1 \} \\
&= \{E | 0, 0, 1 \},
\end{aligned} \tag{S57}$$

with \bar{E} being the spin-1/2 2π rotation, E being the identity, and $\{E | 0, 0, 1 \} |\psi_{k_1, k_2, 0.5} \rangle = -|\psi_{k_1, k_2, 0.5} \rangle$.

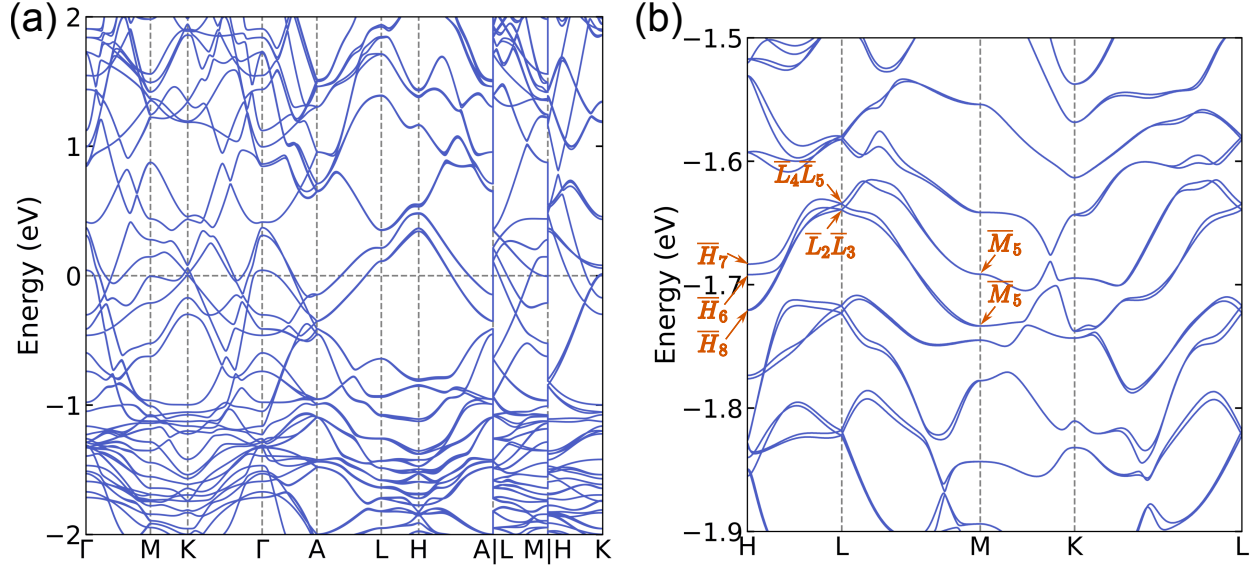
This implies

$$\langle \psi_{k_1, k_2, 0.5} | \{C_{2z} \mathcal{T} | 0, 0, 1/2 \} \psi_{k_1, k_2, 0.5} \rangle = 0, \tag{S58}$$

meaning that $\{C_{2z} \mathcal{T} | 0, 0, 1/2 \} |\psi_{k_1, k_2, 0.5} \rangle$ and $|\psi_{k_1, k_2, 0.5} \rangle$ are orthogonal states with the same crystal momentum $(k_1, k_2, 0.5)$ and energy. Hence, due to the $\{C_{2z} \mathcal{T} | 0, 0, 1/2 \}$ symmetry, the energy bands with crystal momentum $(k_1, k_2, 0.5)$ is twofold degenerate for a system with space group no. 173 ($P6_3$) and spin-1/2 time-reversal symmetry.

Supplementary Note 10. DFT RESULTS FOR Ce_2NiGe_3

Supplementary Fig. S14(a) provides the DFT band structure of Ce_2NiGe_3 , where the effect of spin-orbit couplings is included. The degeneracies and nodal lines that happen away from Fermi energy are consistent with our symmetry analysis. Supplementary Fig. S14(b) shows a zoomed-in plot of the hourglass shaped crossings (part of the symmetry enforced Weyl-nodal line) near -2eV along high symmetry lines $H-L-M-K-L$. The irreducible representations are also analyzed, which agrees with the symmetry analysis³⁰.



Supplementary Fig. S14. (a) DFT band structures (with spin-orbit couplings) of Ce_2NiGe_3 with the achiral space group no. 190 ($P\bar{6}2c$), and (b) the corresponding zoomed-in band structure along high symmetry lines $H - L - M - K - L$. The Weyl-nodal lines near L point is consistent with symmetry requirement.

Supplementary Note 11. PROCEDURE FOR SEARCHING CANDIDATE MATERIALS

In this section, we provide an expanded description of the procedure we used to search for candidate materials of topological Kondo semimetals in hexagonal crystal systems.

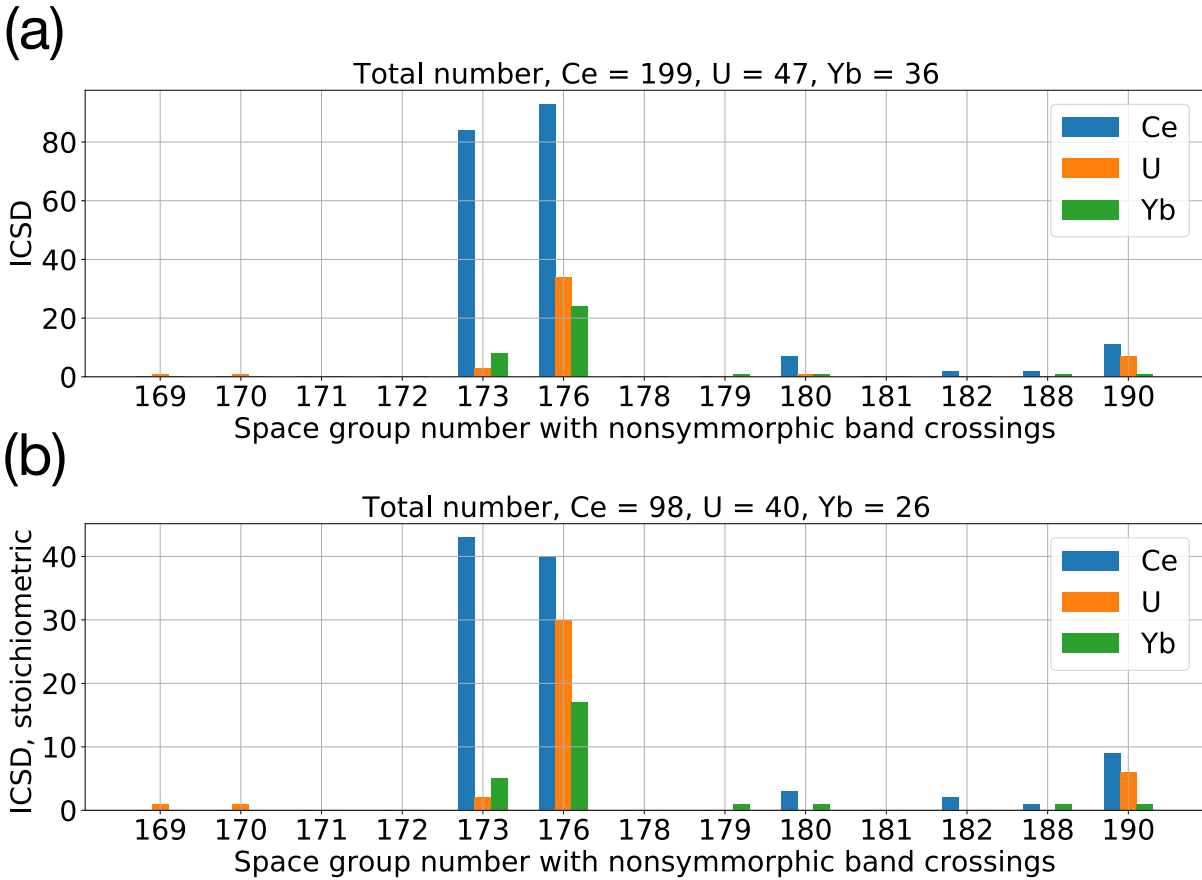
In our procedure, we start by obtaining cerium-, uranium-, and ytterbium-based materials with hexagonal space groups that support band-crossing features³⁰ in ICSD. We next perform a literature search on those materials about their measured physical properties, which can be categorized as follows:

1. Electrical resistivity (ρ): Measurements of ρ can establish if a material has a semimetallic-type resistivity and, in some cases, if the material exhibits Kondo physics. If $\rho(T)$ is nearly independent of T , or does not show a significant difference between high and low T , where T is the temperature, then the system exhibits a semimetallic-type resistivity. This can be quantified by evaluating the residual resistivity ratio (RRR) $\equiv \frac{\rho(\text{high } T)}{\rho(\text{low } T)}$. A material with the semimetallic-type resistivity would exhibit an order $O(1)$ RRR. On the other hand, a system with band-crossing features could also be a metal, where the Fermi-liquid type resistivity exhibits a T^2 -behavior. Alternatively, if $\rho(T)$ decreases as T decreases, we may also associate the system with metallic-type resistivity. On the other hand, Kondo physics can

lead to various features in $\rho(T)$. The Kondo-lattice coherence can lead to a local maximum in $\rho(T)$. The magnetic contribution to the resistivity, denoted as $\rho_{\text{mag}}(T)$, also exhibits a $-\ln(T)$ -behavior at relatively high temperatures due to the Kondo effect.

2. **Magnetic properties:** Magnetic measurements such as the temperature dependence of the magnetic susceptibility (χ) can establish whether the magnetic coupling in the material is of the antiferromagnetic type or of the ferromagnetic type, and if the material has magnetic orders. Magnetic transitions typically appear as anomalies in $\chi(T)$. Since we focus on the paramagnetic states with spin-1/2 time-reversal symmetry, materials with low magnetic transition temperatures, or no magnetic orders observed in the experiments, are favorable. From $\chi(T)$, the paramagnetic Curie temperature (θ_p) can be determined through the Curie-Weiss law $\chi(T) = \chi_0 + \frac{C}{T-\theta_p}$ where both χ_0 and C are constants⁶⁰. The constant C can be further used to determine the effective magnetic moment μ_{eff} . A negative [positive] value of θ_p indicates antiferromagnetic (ferromagnetic) interactions.
3. **Specific heat (C_p):** Specific-heat measurements can establish if the material is a heavy-fermion compound that has a moderate or strong correlations, which typically lead to an enhanced value of the Sommerfeld coefficient γ . The Sommerfeld coefficient γ is defined as the linear coefficient of C_p on T . It is the magnetic contribution to the specific heat, denoted as C_{mag} , that is used to determine the Sommerfeld coefficient via the linear-in- T coefficient.
4. **Kondo temperature (T_K):** T_K denotes the temperature scale for the initial onset of Kondo screening as the temperature is lowered. The information of T_K can be extracted from measurements such as electrical resistivity, specific heat or thermopower.

In Supplementary Fig. S15, we show the amount of cerium-, uranium-, and ytterbium-based compounds in the Inorganic Crystal Structure Database (ICSD) that have hexagonal space groups with topological band crossings identified in Ref. 30. We see that space groups no. 173 ($P6_3$), no. 176 ($P6_3/m$), no. 180 ($P6_222$), and no. 190 ($P\bar{6}2c$) are relatively abundant. In the following sections, we provide the details of the primary candidate materials and other materials that are candidate materials we identified through the search procedure described above. In Supplementary Table S6 we provide the notations of relevant physical properties in our studies.



Supplementary Fig. S15. The amount of material entries in the Inorganic Crystal Structure Database (ICSD) that (1) contain either cerium (Ce), uranium (U), or ytterbium (Yb) element, and (2) has a hexagonal space group that exhibits topological band crossings enforced by nonsymmorphic symmetries as classified in Ref. 30. (a) includes both stoichiometric and non-stoichiometric compounds while (b) includes only the stoichiometric ones.

Supplementary Note 12. PRIMARY CANDIDATE MATERIALS

1. CePt_2B

CePt_2B ^{37,38} has the chiral space group no. 180 ($P6_222$) and could be a potential candidate for the paramagnetic chiral WKSM with Weyl points³⁰, provided that the temperature is above the magnetic transition temperature and below (or around) the characteristic temperature T_K . We now summarize the supporting physical properties of CePt_2B reported in Ref. 38, see also Supplementary Fig. S16 for the experimental figures we copied from Ref. 38. The magnetic transition

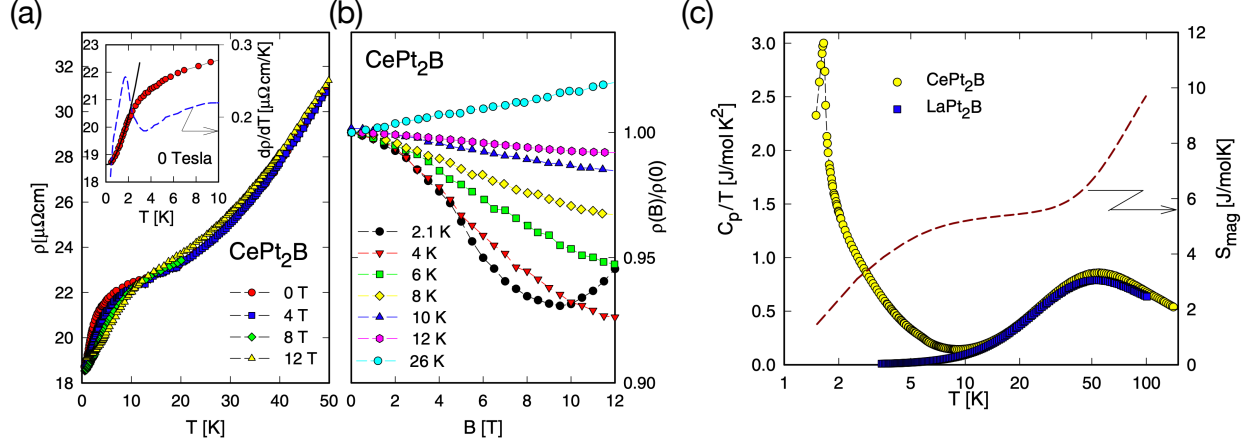
Temperature	T
Magnetic susceptibility	χ
Paramagnetic Curie temperature or Curie-Weiss temperature	θ_p
Neél temperature (anti-ferromagnetic transition temperature)	T_N
Curie temperature (ferromagnetic transition temperature)	T_C
Bohr magneton	μ_B
(Experimentally-determined) effective magnetic moment	μ_{eff}
Specific heat	C_p
Magnetic contribution to the specific heat	C_{mag}
Sommerfeld coefficient	γ
Electrical resistivity	ρ
Magnetic contribution to the electrical resistivity	ρ_{mag}
Residual resistivity ratio	$\text{RRR} \equiv \frac{\rho(\text{high } T)}{\rho(\text{low } T)}$
Kondo temperature	T_K

Supplementary Table S6. Notations related to the physical properties.

temperature is reported as 2.1K from the observation of a λ -like anomaly in the C_p/T result. The characteristic temperature $T_K = 3.5 - 5\text{K}$ for CePt₂B is obtained from the results of specific heat and magnetic entropy. In addition, the measured electrical resistivity ρ of CePt₂B shows metallic behavior, where $\rho(T)$ decreases as T decreases, and ρ takes values around 20 – 30 $\mu\Omega\text{cm}$ from the lowest experimental temperature to 50K. Specifically, $\rho(T = 5\text{K}) \approx 22 \mu\Omega\text{cm}$ for CePt₂B. Regarding the electron correlation in CePt₂B, the experimental value of C_p/T is large ($> 100 \text{ mJ/K}^2 \text{ mol}$), which we here interpret as a potential indication of heavy-fermion behavior. Finally, as stated in Ref. 38, the magnetoresistance $\rho(B)/\rho(0)$, where B is the applied magnetic field, of CePt₂B exhibits the qualitative form of the Kondo model^{14,61}.

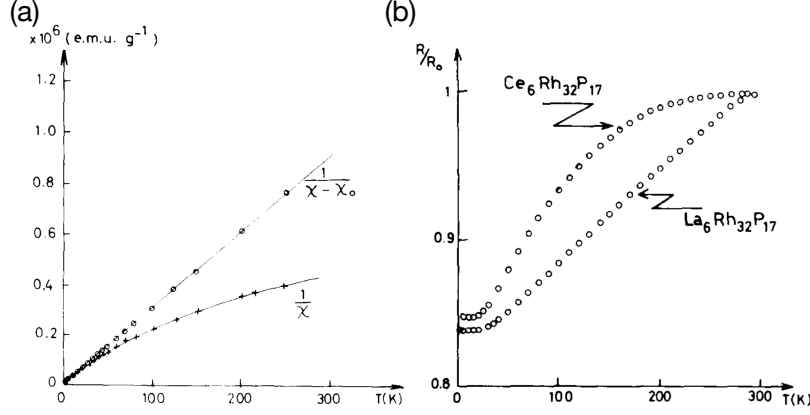
2. Ce₆Rh₃₂P₁₇

Ce₆Rh₃₂P₁₇⁴⁷ has the achiral space group no. 176 ($P6_3/m$) and it could be a potential candidate for the paramagnetic Dirac-Kondo semimetal with fourfold degenerate nodal lines on the BZ boundary³⁰. In Supplementary Fig. S17 we provide the experimental figures copied from



Supplementary Fig. S16. (a) Electrical resistivity as a function of temperature at different applied field strengths, (b) magnetoresistance as a function of applied field at different temperatures, and (c) specific heat divided by temperature as a function of temperature together with the magnetic entropy as a function of temperature for CePt_2B copied from Ref. 38.

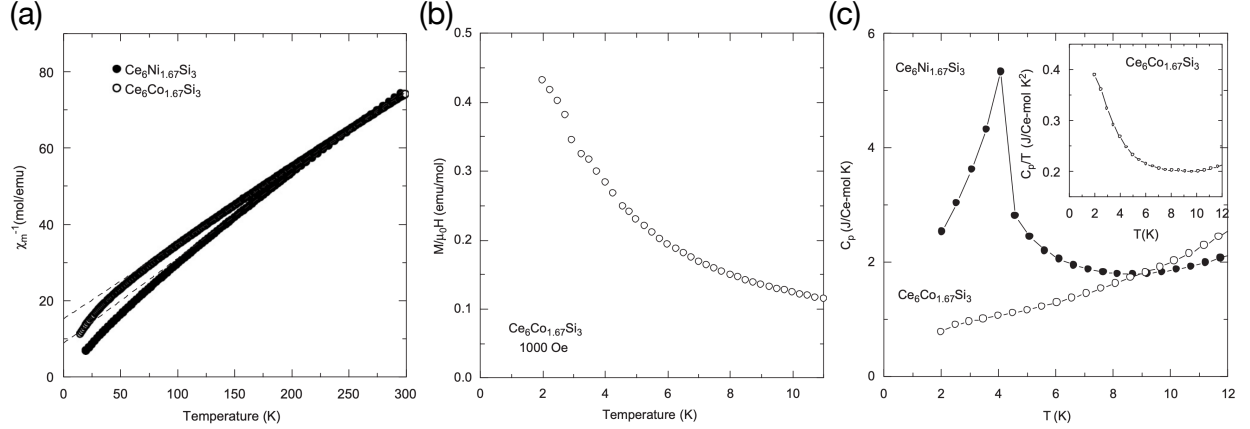
Ref. 47. The measurements of the magnetic susceptibility yield the effective magnetic moment $\mu_{\text{eff}} = 1.43\mu_B$ and the paramagnetic Curie temperature $\theta_p = -2\text{K}$. The negative value of θ_p suggests that $\text{Ce}_6\text{Rh}_{32}\text{P}_{17}$ has anti-ferromagnetic coupling. There is no signature of magnetic transition in the magnetic measurements reported in Ref. 47, which means that $\text{Ce}_6\text{Rh}_{32}\text{P}_{17}$ remains paramagnetic down to the lowest temperature of the experiments. The measured electrical resistivity $\rho(T)$ is $580000 \mu\Omega\text{cm}$ at $T = 293\text{K}$ and is $495000 \mu\Omega\text{cm}$ at $T = 2\text{K}$. Although these values of the electrical resistivity are relatively high, the ratio $\frac{\rho(T=293\text{K})}{\rho(T=2\text{K})} \approx 1.17$ indicates that the temperature dependence of $\rho(T)$ is of the semimetallic type, meaning that there is no significant difference between the high-temperature and low-temperature resistivities. Furthermore, $\rho(T)$ shows a small upturn around $T = 30\text{K}$ as the temperature is lowered, which indicates potential Kondo physics such as the Kondo scattering. We note that in ICSD, the P elements at the $4f$ and $2b$ positions in $\text{Ce}_6\text{Rh}_{32}\text{P}_{17}$ (ICSD Collection Code 52890) are reported to have half occupancy. Since the element with half occupancy is not Ce, we may expect that this will not affect the lattice-coherent behavior formed from the Ce elements.



Supplementary Fig. S17. The temperature dependence of (a) inverse magnetic susceptibility and (b) normalized electrical resistivity for $\text{Ce}_6\text{Rh}_{32}\text{P}_{17}$ copied from Ref. 47.

3. $\text{Ce}_6\text{Co}_{2-\delta}\text{Si}_3$ ($\delta = 0.33$)

The chemical formula of $\text{Ce}_6\text{Co}_{2-\delta}\text{Si}_3$ we consider in this work is $\text{Ce}_6\text{Co}_{1.67}\text{Si}_3$ ^{48,49}, which has the achiral space group no. 176 ($P6_3/m$) and it could be a potential candidate for the paramagnetic Dirac-Kondo semimetal with fourfold degenerate nodal lines on the BZ boundary³⁰. In Supplementary Fig. S18 we provide the experimental figures of $\text{Ce}_6\text{Co}_{1.67}\text{Si}_3$ copied from Ref. 48. The measurements of the magnetic susceptibility yield the effective magnetic moment $\mu_{\text{eff}} = 2.59\mu_B/\text{Ce}$ and the paramagnetic Curie temperature $\theta_p = -77\text{K}$. The relatively large negative value of θ_p indicates relatively strong anti-ferromagnetic couplings, suggesting that $\text{Ce}_6\text{Co}_{1.67}\text{Si}_3$ may be a Kondo compound. The magnetic measurements also show that there is no magnetic ordering at least above 1.8K, which is also supported by the specific-heat measurements showing no anomalies. This indicates that $\text{Ce}_6\text{Co}_{1.67}\text{Si}_3$ remains paramagnetic at least above 1.8K. The Sommerfeld coefficient γ is determined as $\gamma = 162 \text{ mJ/K}^2 \text{ Ce-mol}$ using the specific-heat data in the temperature range between $T = 10\text{K}$ and 22K , suggesting that $\text{Ce}_6\text{Co}_{1.67}\text{Si}_3$ is a moderate heavy-fermion compound. In addition, as reported in Ref. 48, the colour of $\text{Ce}_6\text{Co}_{1.67}\text{Si}_3$ is metallic light grey, which suggests that $\text{Ce}_6\text{Co}_{1.67}\text{Si}_3$ might be non-insulating. We note that in $\text{Ce}_6\text{Co}_{1.67}\text{Si}_3$ some Co elements have partial occupancy, as reported in Ref. 48. Since the element with partial occupancy is not Ce, we may expect that this will not affect the lattice-coherent behavior formed from the Ce elements.

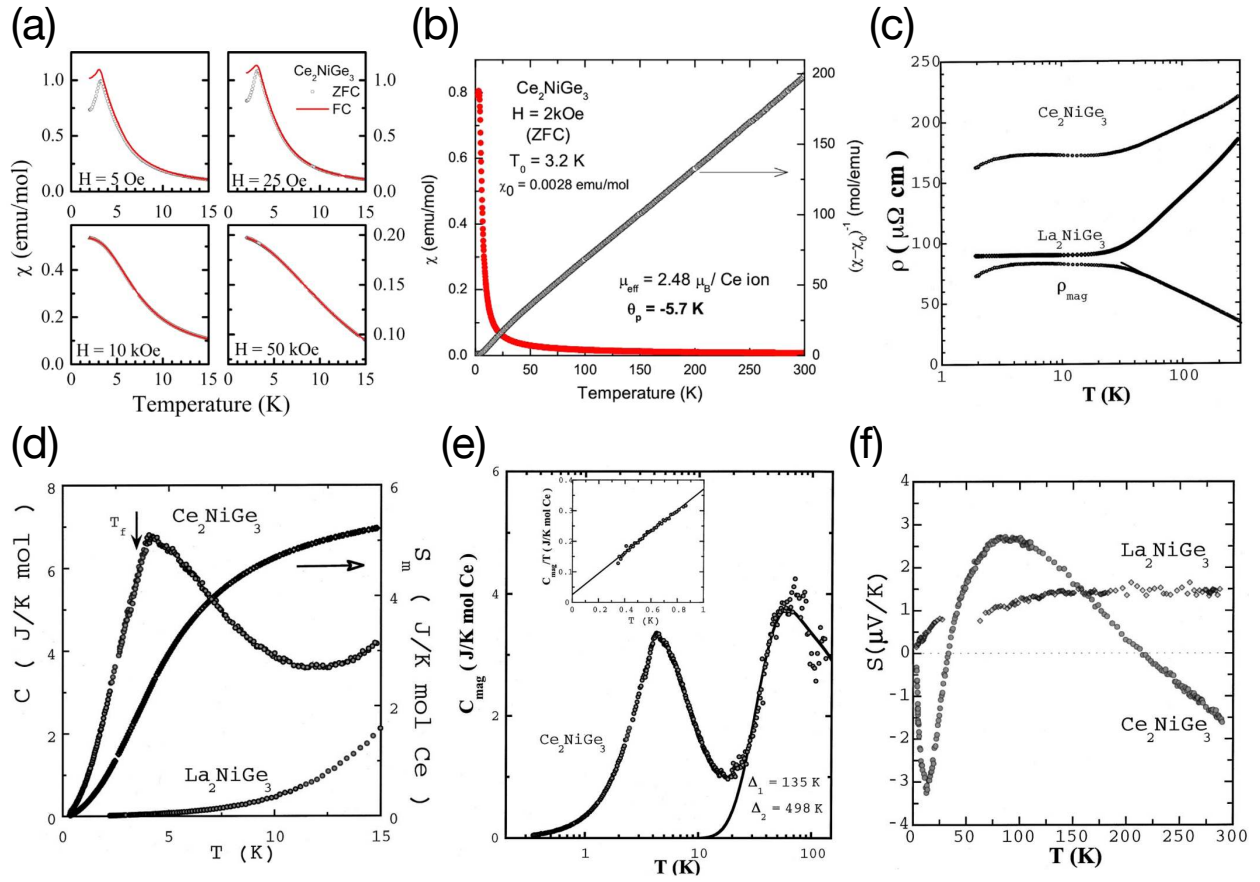


Supplementary Fig. S18. The temperature dependence of (a) inverse magnetic susceptibility, (b) magnetization divided by the applied field, and (c) specific heat (inset: C_p/T as a function of T) for $\text{Ce}_6\text{Co}_{1.67}\text{Si}_3$ ($\text{Ce}_6\text{Co}_{2-\delta}\text{Si}_3$ with $\delta = 0.33$) copied from Ref. 48.

4. Ce_2NiGe_3

Ce_2NiGe_3 ³⁹ has the achiral space group no. 190 ($P\bar{6}2c$) and it could be a potential candidate for the paramagnetic WKSM with Weyl nodal lines on the BZ boundary³⁰, provided that the temperature is above the magnetic transition temperature. The measurements of the magnetic susceptibility yield the effective magnetic moment $\mu_{\text{eff}} = 2.48\mu_B$ and the paramagnetic Curie temperature $\theta_p = -5.7\text{K}$. The negative value of $\theta_p = -5.7\text{K}$ suggests anti-ferromagnetic couplings in Ce_2NiGe_3 . The magnetic measurements further suggest an anti-ferromagnetic ordering at $T_N = 3.2\text{K}$. This means that above $T_N = 3.2\text{K}$ Ce_2NiGe_3 could be in the paramagnetic state, see also Supplementary Fig. S19 for the experimental figures we copied from Ref. 39.

Although Ref. 42 reports that Ce_2NiGe_3 crystallizes in the hexagonal AlB_2 -type structure, we here include the physical properties of Ce_2NiGe_3 reported in Ref. 42, as they further supports that Ce_2NiGe_3 could be a paramagnetic WKSM, see also Supplementary Fig. S19 for the experimental figures we copied from Ref. 42. Specifically, the $\rho(T)$ data reported in Ref. 42 indicates that $\rho(T = 2\text{K})$ is about $160 \mu\Omega\text{cm}$, $\rho(T = 10\text{K})$ is about $170 \mu\Omega\text{cm}$, $\rho(T = 100\text{K})$ is about $200 \mu\Omega\text{cm}$, and $\rho(T = 200\text{K})$ is about $210 \mu\Omega\text{cm}$, which indicate a semimetallic-type resistivity as $\frac{\rho(T=200\text{K})}{\rho(T=10\text{K})} \approx 1.24$. In addition, the magnetic contribution to the resistivity $\rho_{\text{mag}}(T)$, which is obtained in Ref. 42 by subtracting the $\rho(T)$ data of La_2NiGe_3 from the $\rho(T)$ data of Ce_2NiGe_3 , shows $-\ln T$ -behaviors from the room temperature to $T = 50\text{K}$ and from $T = 20\text{K}$ to $T = 5\text{K}$,



Supplementary Fig. S19. (a)&(b) Magnetic susceptibility of Ce_2NiGe_3 copied from Ref. 39. The temperature dependence of (c) electrical resistivity and magnetic resistivity, (d) specific heat and magnetic entropy, (e) magnetic specific heat (inset: C_{mag}/T as a function of T), and (f) thermoelectric power for Ce_2NiGe_3 copied from Ref. 42.

suggesting the Kondo effect in the paramagnetic phase of Ce_2NiGe_3 . The Sommerfeld coefficient is obtained as $\gamma = 25 \text{ mJ/K}^2 \text{ Ce-mol}$ in Ref. 42 using the data below $T = 1\text{K}$ of the magnetic contribution to the specific heat $C_{\text{mag}}(T)$, which is obtained in Ref. 42 by subtracting the $C_p(T)$ data of La_2NiGe_3 from the $C_p(T)$ data of Ce_2NiGe_3 . The thermoelectric power of Ce_2NiGe_3 is also reported in Ref. 42, showing a positive peak and a negative peak together with a sign change, which are significantly different behaviors compared with La_2NiGe_3 .

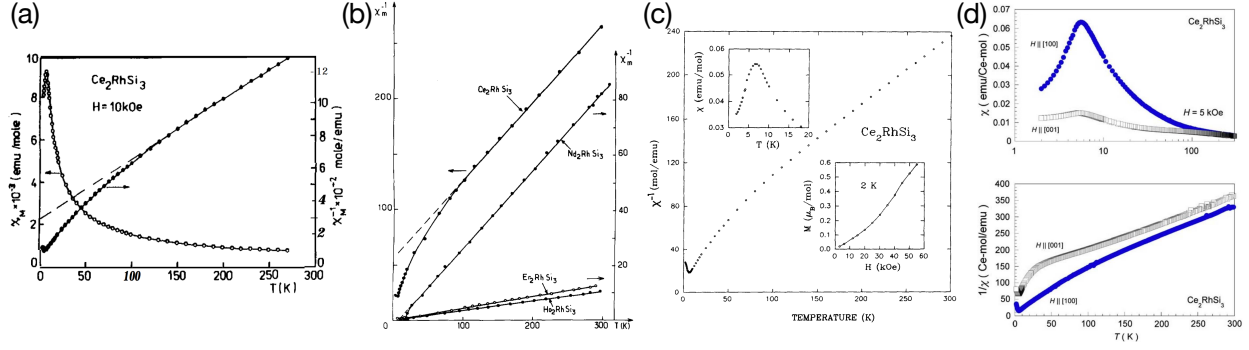
5. Ce₂RhSi₃

Ce₂RhSi₃^{40,41} has the achiral space group no. 190 ($P\bar{6}2c$) and it could be a potential candidate for the paramagnetic WKSM with Weyl nodal lines on the BZ boundary³⁰, provided that the temperature is above the magnetic transition temperature. The measurements of the magnetic susceptibility in the temperature range 100 – 300K yield the effective magnetic moment $\mu_{\text{eff}} = 2.4\mu_{\text{B}}/\text{Ce}$ and the paramagnetic Curie temperature $\theta_p = -80\text{K}$. In addition, in the temperature range 8 – 20K, $\mu_{\text{eff}} = 1.54\mu_{\text{B}}/\text{Ce}$ and $\theta_p = -6.5\text{K}$. The magnetic measurements further suggest an anti-ferromagnetic ordering at $T_{\text{N}} = 6.8\text{K}$. This means that above T_{N} Ce₂RhSi₃ could be in the paramagnetic state.

Although Ce₂RhSi₃ could crystallize in other hexagonal structures^{43–46}, in the following we include physical properties reported in some of these references, as they further support our prediction that Ce₂RhSi₃ could be a paramagnetic WKSM. Importantly, some of these references also report the Sommerfeld coefficients γ and the estimates of the Kondo temperature T_{K} . Hence, above T_{N} and below (or around) T_{K} , Ce₂RhSi₃ could be in the paramagnetic Kondo-driven heavy-fermion phase. In Supplementary Fig. S20, Supplementary Fig. S21, Supplementary Fig. S22, and Supplementary Fig. S23 we provide experimental figures for Ce₂RhSi₃ copied from the literature.

We begin with Ref. 44. Magnetic susceptibility measurements yield $\mu_{\text{eff}} = 2.48\mu_{\text{B}}$ and $\theta_p = -65\text{K}$ in the temperature range 100 – 300K, and $\theta_p = -10\text{K}$ in the temperature range 10 – 40K. The antiferromagnetic transition temperature is reported as $T_{\text{N}} = 6\text{K}$. The electrical resistivity of Ce₂RhSi₃ is also reported to be about 800 $\mu\Omega\text{cm}$ in the temperature range 8 – 20K and $\frac{\rho(300\text{K})}{\rho(20\text{K})} \approx 1.48$, suggesting a semimetallic-type resistivity. Furthermore, the Sommerfeld coefficient is extracted as $\gamma = 100 \text{ mJ/K}^2 \text{ mol}$ from the specific-heat data, suggesting heavy-fermion behavior.

Next, we consider Ref. 45. It reports $\mu_{\text{eff}} = 2.57\mu_{\text{B}}/\text{Ce}$ and $\theta_p = -79\text{K}$ for the applied field $H \parallel [100]$ and $\mu_{\text{eff}} = 2.68\mu_{\text{B}}/\text{Ce}$ and $\theta_p = -127\text{K}$ for $H \parallel [001]$ from the magnetic susceptibility above 100K. The antiferromagnetic transition temperature of Ce₂RhSi₃ is also extracted as $T_{\text{N}} = 4.5$ or 5K . The electrical resistivity of Ce₂RhSi₃ is consistent with a semimetal, with no significant difference between high-temperature and low-temperature values. In addition, the magnetic contribution ρ_{mag} to the electrical resistivity, which is obtained by subtracting ρ of La₂RhSi₃ from ρ of Ce₂RhSi₃, exhibits $-\ln T$ -behaviors from room temperature to 100K and from 20K to 5K, suggesting Kondo physics. Below T_{N} , the Sommerfeld coefficient is determined as $\gamma = 290$



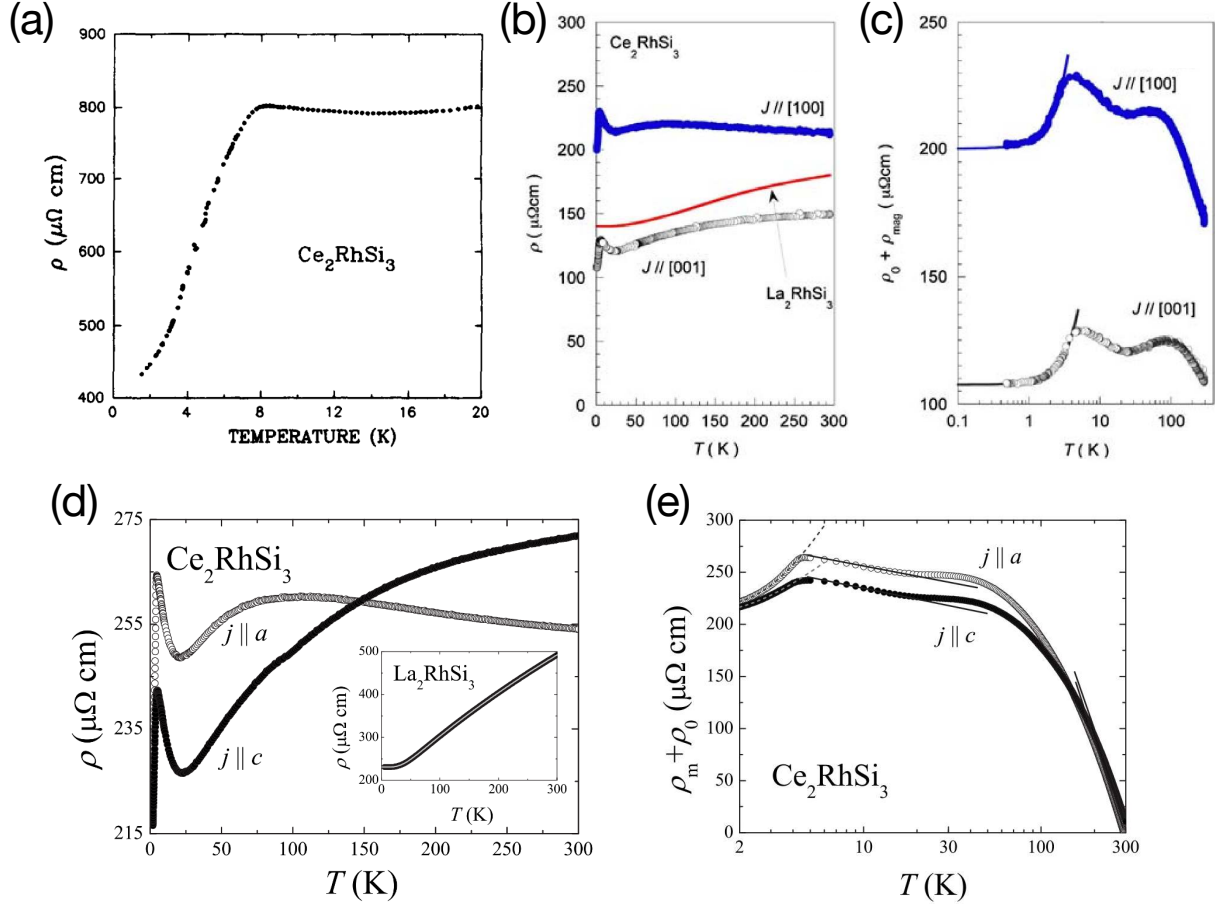
Supplementary Fig. S20. Temperature dependence of the magnetic susceptibility and/or the inverse magnetic susceptibility for Ce_2RhSi_3 copied from (a) Ref. 41, (b) Ref. 43, (c) Ref. 44, and (d) Ref. 45. In (d), the applied magnetic field is along either [100] or [001].

mJ/K^2 Ce-mol, which suggests that Ce_2RhSi_3 is a heavy-fermion system. At T_N , the magnetic entropy is extracted as $0.56R \ln 2$, which suggests that a moderate Kondo effect could be present in Ce_2RhSi_3 . Importantly, the Kondo temperature is estimated as $T_K = 12\text{K}$, which is the mean value of different estimates.

Finally, we have Ref. 46 for Ce_2RhSi_3 . Magnetic susceptibility measurements yield $\mu_{\text{eff}}^c = 2.55\mu_B$, $\theta_p^c = -102\text{K}$, $\mu_{\text{eff}}^a = 2.6\mu_B$, and $\theta_p^a = -78\text{K}$ above 200K, where the superscripts a and c mean that the applied magnetic field is along the a and c axes, respectively. The magnetic transition temperature is reported as $T_N = 4.5\text{K}$. The X-ray photoemission spectroscopy measurements suggest that the Ce ions are trivalent. The electrical resistivity at room temperature is reported as $\rho^a = 254 \mu\Omega\text{cm}$ and $\rho^c = 272 \mu\Omega\text{cm}$, and at 2K as $\rho^a = 222 \mu\Omega\text{cm}$ and $\rho^c = 217 \mu\Omega\text{cm}$, which could be classified as the semimetallic-type resistivity. ρ^a and ρ^c mean the electrical resistivity measured along the a and c axes. $-\ln T$ -behaviors are also observed in the magnetic contribution to the electrical resistivity. In addition, as reported in Ref. 46, the magnetoresistivity of Ce_2RhSi_3 demonstrates a data collapse corresponding to the scaling behavior of Kondo systems^{14,61}. Below 3K, the Sommerfeld coefficient is extracted as $\gamma = 580 \text{mJ/K}^2 \text{mol}$ using the data of $C_p(\text{Ce}_2\text{RhSi}_3) - C_p(\text{La}_2\text{RhSi}_3)$. The Kondo temperature T_K is estimated to be 9K or 9.5K.

Supplementary Note 13. ADDITIONAL CANDIDATE MATERIALS

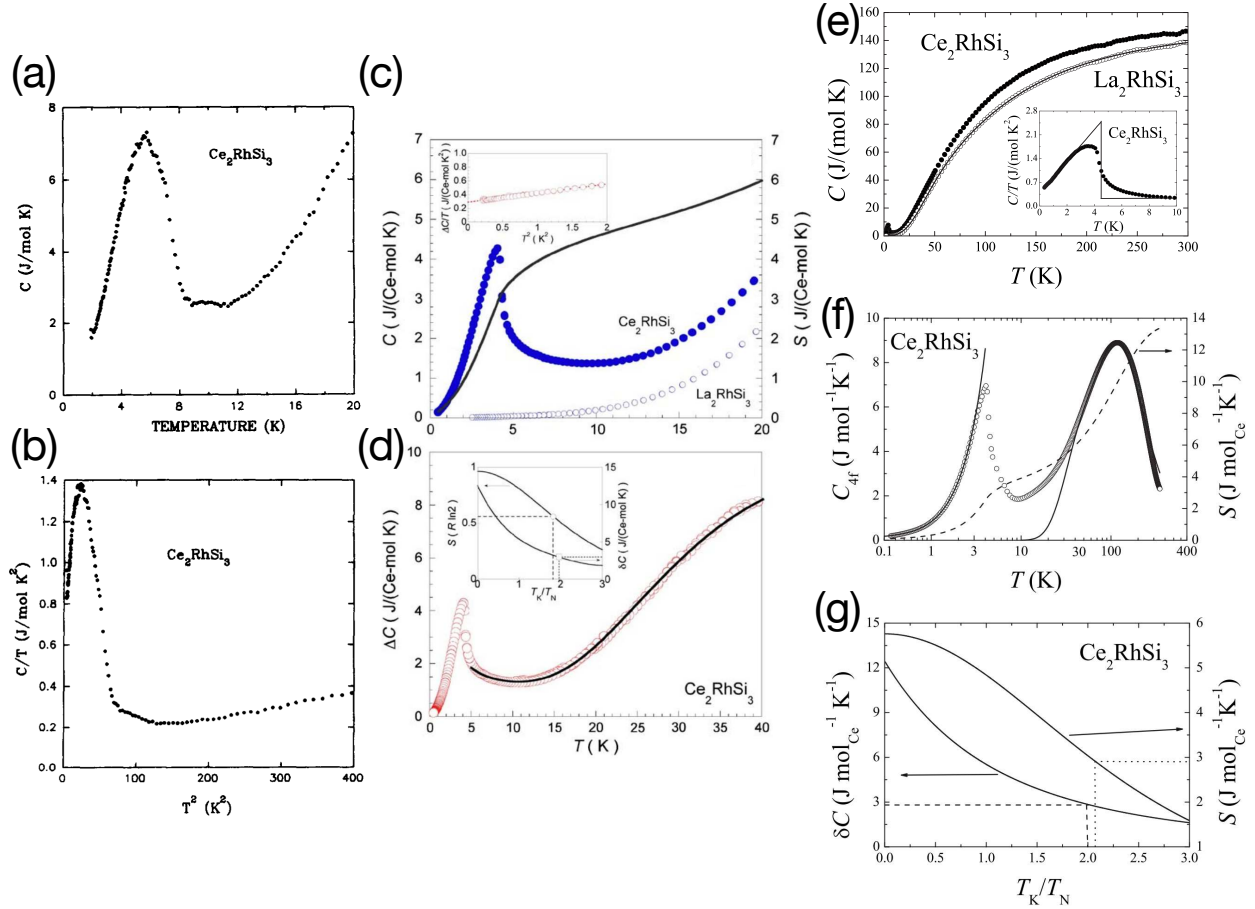
In this section, we provide additional candidate materials where their properties are summarized in Supplementary Table S7.



Supplementary Fig. S21. Temperature dependence of the electrical resistivity for Ce_2RhSi_3 copied from (a) Ref. 44, (b) Ref. 45, and (d) Ref. 46. Temperature dependence of the magnetic contribution to the electrical resistivity for Ce_2RhSi_3 copied from (c) Ref. 45 and (e) Ref. 46. In (b), (c), (d), and (e), the current flows along the a ([100]) and c ([001]) axes.

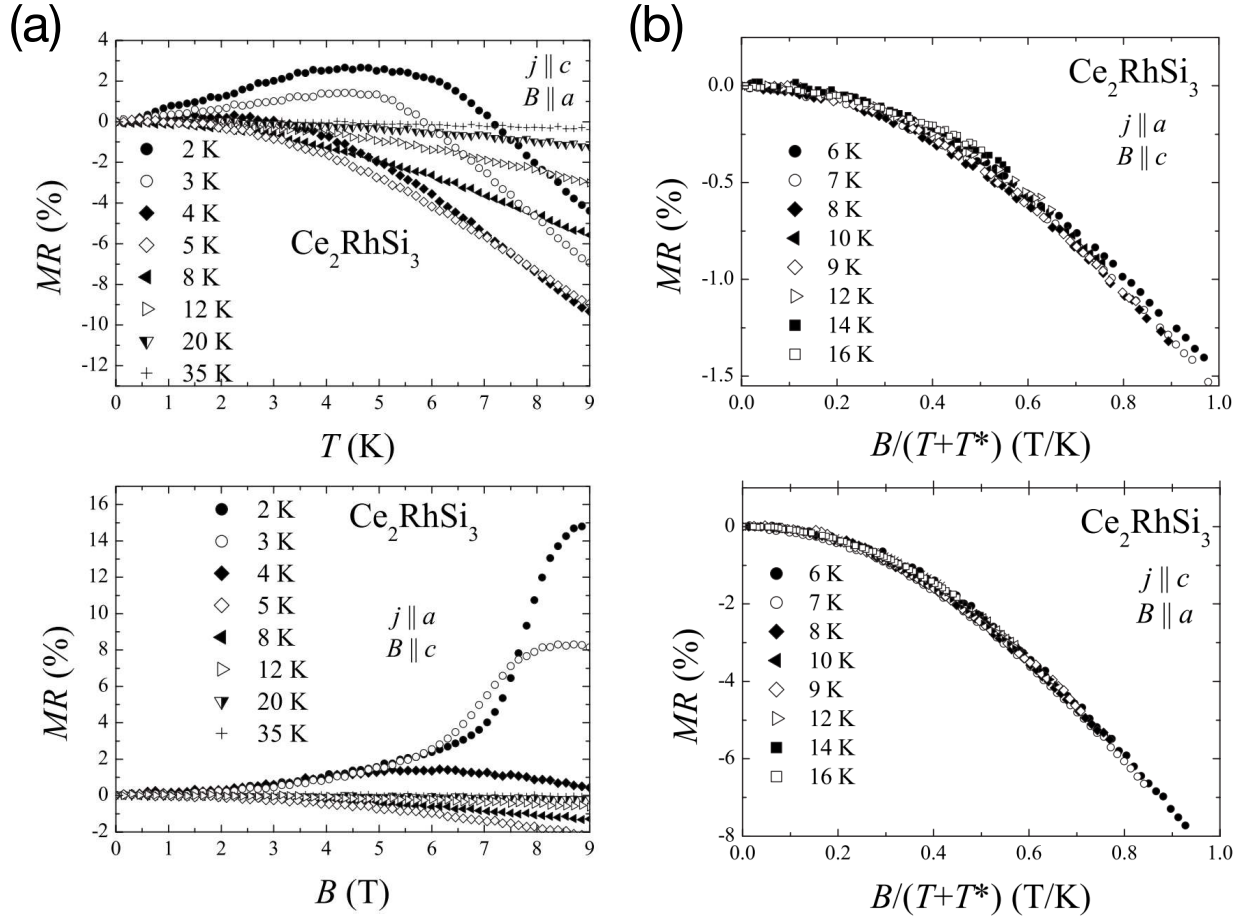
1. $\text{Ce}_6\text{Ni}_{2-\delta}\text{Si}_3$ ($\delta = 0.33$)

The chemical formula of $\text{Ce}_6\text{Ni}_{2-\delta}\text{Si}_3$ we consider in this work is $\text{Ce}_6\text{Ni}_{1.67}\text{Si}_3$ ⁴⁸, which has the achiral space group no. 176 ($P6_3/m$) and it could be a potential candidate for the paramagnetic Dirac-Kondo semimetal with fourfold degenerate nodal lines on the BZ boundary³⁰, provided that the temperature is above the magnetic transition temperature. The measurements of the magnetic susceptibility yield the effective magnetic moment $\mu_{\text{eff}} = 2.45\mu_{\text{B}}/\text{Ce}$ and the paramagnetic Curie temperature $\theta_p = -36\text{K}$. The negative value of θ_p indicates anti-ferromagnetic couplings. The magnetic measurements further suggest a magnetic ordering below $T = 3.8(2)\text{K}$, while further experiments are required to determine the nature of this magnetic ordering. This means that above



Supplementary Fig. S22. (a) Specific heat as a function of temperature, and (b) specific heat divided by temperature (T) as a function of T^2 for Ce_2RhSi_3 copied from Ref. 44. (c) Specific heat and (d) magnetic contribution to the specific heat ΔC as a function of temperature for Ce_2RhSi_3 copied from Ref. 45. ΔC is obtained by subtracting the specific heat of La_2RhSi_3 from the specific heat of Ce_2RhSi_3 . The inset of (c) is $\Delta C/T$ as a function of T^2 . (e) Specific heat and (f) $C_{4f} \equiv$ specific heat of Ce_2RhSi_3 minus specific heat of La_2RhSi_3 as a function of temperature for Ce_2RhSi_3 copied from Ref. 46. The inset of (d) and the panel (g) are the procedure used in Ref. 45 and Ref. 46, respectively, to estimate the Kondo temperature, based on the magnetic entropy and the jump of specific heat at T_N .

$T = 3.8(2)\text{K}$ $\text{Ce}_6\text{Ni}_{1.67}\text{Si}_3$ could be in the paramagnetic state. The Sommerfeld coefficient γ is determined as $\gamma = 144 \text{ mJ/K}^2 \text{ Ce-mol}$ using the specific-heat data in the temperature range between $T = 10\text{K}$ and 22K , suggesting that $\text{Ce}_6\text{Ni}_{1.67}\text{Si}_3$ is a moderate heavy-fermion compound. In addition, the specific-heat data exhibit a peak around $T = 4.1(2)\text{K}$, which is consistent with the magnetic ordering temperature $T = 3.8(2)\text{K}$ from the magnetic measurements. Using the



Supplementary Fig. S23. (a) Transverse magnetoresistivity $MR = \frac{\rho(B) - \rho(0)}{\rho(0)}$, where $\rho(B)$ is the electrical resistivity as a function of the applied magnetic field B , and (b) Kondo scaling behavior of $MR^{14,61}$ copied from Ref. 46. $j \parallel a$ and $j \parallel c$ mean the current flows along a and c axes, respectively. $B \parallel a$ and $B \parallel c$ mean the applied magnetic field is along a and c axes, respectively. T^* denotes the characteristic temperature in the scaling behavior.

magnetic entropy extracted from the specific-heat data, Ref. 48 also suggests that $\text{Ce}_6\text{Ni}_{1.67}\text{Si}_3$ may have a moderate Kondo effect. In addition, as reported in Ref. 48, the colour of $\text{Ce}_6\text{Ni}_{1.67}\text{Si}_3$ is metallic light grey, which suggests that $\text{Ce}_6\text{Ni}_{1.67}\text{Si}_3$ might be non-insulating. We note that in $\text{Ce}_6\text{Ni}_{1.67}\text{Si}_3$ some Ni elements have partial occupancy, as reported in Ref. 48. Since the element with partial occupancy is not Ce, we may expect that this will not affect the lattice-coherent behavior formed from the Ce elements.

Additional candidate material

Material	SG #	SG	Magnetic transition T	T_K	Resistivity	γ	Crossing
$\text{Ce}_6\text{Ni}_{1.67}\text{Si}_3$	176	$P6_3/m$	3.8(2)K			144 mJ/K ² Ce-mol	DNL
$\text{Ce}_5\text{Ni}_{1.85}\text{Si}_3$	176	$P6_3/m$	$T_N = 4.8(2)\text{K}$				DNL
$\text{Ce}_5\text{Ni}_2\text{Si}_3$	176	$P6_3/m$	$T_N = 7.3\text{K}$	31K	Semimetallic	600 mJ/K ² Ce-mol	DNL
$\text{Ce}_{20}\text{Ni}_{42}\text{As}_{31}$	176	$P6_3/m$	\times		Semimetallic		DNL
$\text{Ce}_{20}\text{Ni}_{42}\text{P}_{30}$	176	$P6_3/m$	32K	67K	Semimetallic		DNL

Supplementary Table S7. Summary of the physical properties of additional candidate materials $\text{Ce}_6\text{Ni}_{1.67}\text{Si}_3$ ⁴⁸, $\text{Ce}_5\text{Ni}_{1.85}\text{Si}_3$ ⁴⁸, $\text{Ce}_5\text{Ni}_2\text{Si}_3$ ^{62,63}, $\text{Ce}_{20}\text{Ni}_{42}\text{As}_{31}$ ⁶⁴, and $\text{Ce}_{20}\text{Ni}_{42}\text{P}_{30}$ ^{65,66}. “SG” means “space group”. A “ \times ” mark in magnetic transition T means no magnetic transition is reported. “DNL” means “Dirac nodal line”. We refer readers to Supplementary Note 13 for detailed descriptions of the additional candidate materials, such as how different physical properties are determined.

2. $\text{Ce}_5\text{Ni}_{2-\delta}\text{Si}_3$ ($\delta = 0.15$)

The chemical formula of $\text{Ce}_5\text{Ni}_{2-\delta}\text{Si}_3$ we consider in this work is $\text{Ce}_5\text{Ni}_{1.85}\text{Si}_3$ ⁴⁸, which has the achiral space group no. 176 ($P6_3/m$) and it could be a potential candidate for the paramagnetic Dirac-Kondo semimetal with fourfold degenerate nodal lines on the BZ boundary³⁰, provided that the temperature is above the magnetic transition temperature. The measurements of the magnetic susceptibility yield the effective magnetic moment $\mu_{\text{eff}} = 2.51\mu_B/\text{Ce}$ and the paramagnetic Curie temperature $\theta_p = -43\text{K}$. The negative value of θ_p indicates anti-ferromagnetic couplings. The magnetic measurements further suggest an anti-ferromagnetic ordering at $T_N = 4.8(2)\text{K}$ as a kink in the temperature dependence of the magnetization divided by the applied field. This means that above $T_N = 4.8(2)\text{K}$ $\text{Ce}_5\text{Ni}_{1.85}\text{Si}_3$ could be in the paramagnetic state. In addition, as reported in Ref. 48, the colour of $\text{Ce}_5\text{Ni}_{1.85}\text{Si}_3$ is metallic light grey, which suggests that $\text{Ce}_5\text{Ni}_{1.85}\text{Si}_3$ might be non-insulating. We note that in $\text{Ce}_5\text{Ni}_{1.85}\text{Si}_3$ some Ni elements have partial occupancy, as reported in Ref. 48. Since the element with partial occupancy is not Ce, we may expect that this will not affect the lattice-coherent behavior formed from the Ce elements.

3. $\text{Ce}_5\text{Ni}_2\text{Si}_3$

$\text{Ce}_5\text{Ni}_2\text{Si}_3$ ^{62,63} has the achiral space group no. 176 ($P6_3/m$) and it could be a potential candidate for the paramagnetic Dirac-Kondo semimetal with fourfold degenerate nodal lines on the BZ boundary³⁰, provided that the temperature is above the magnetic transition temperature. The measurements of the magnetic susceptibility yield the effective magnetic moment $\mu_{\text{eff}} = 2.42\mu_B/\text{Ce}$ and the paramagnetic Curie temperature $\theta_p = -61.3\text{K}$. The relatively large negative value of θ_p indicates relatively strong anti-ferromagnetic couplings, suggesting that $\text{Ce}_5\text{Ni}_2\text{Si}_3$ might be a Kondo compound. The magnetic measurements further suggest an anti-ferromagnetic ordering at $T_N = 7.3\text{K}$. This means that above $T_N = 7.3\text{K}$ $\text{Ce}_5\text{Ni}_2\text{Si}_3$ could be in the paramagnetic state. The Sommerfeld coefficient, also known as the electronic specific heat coefficient, is $\gamma = 600 \text{ mJ/K}^2 \text{ Ce-mol}^{63}$, which is a relatively enhanced value suggesting heavy-fermion behavior in a Kondo system. We note here that this value of γ is obtained via the data of the magnetic contribution to the specific heat $C_{\text{mag}}(T)$, which is obtained by subtracting the specific-heat data of $\text{La}_5\text{Ni}_2\text{Si}_3$ from the specific data of $\text{Ce}_5\text{Ni}_2\text{Si}_3$ ⁶³, and the expression $\gamma = \frac{C_{\text{mag}}(T)}{T}$ with $T \rightarrow 0$ is used. The electrical resistivity $\rho(T)$ takes value between $245 \mu\Omega\text{cm}$ and $260 \mu\Omega\text{cm}$ in the experimental temperature range, suggesting semimetallic-type resistivity. In addition, the magnetic contribution to the resistivity $\rho_{\text{mag}}(T)$, which is obtained by subtracting the $\rho(T)$ data of $\text{La}_5\text{Ni}_2\text{Si}_3$ from the $\rho(T)$ data of $\text{Ce}_5\text{Ni}_2\text{Si}_3$, shows a $-\ln T$ -behavior in the high temperature regime, which may be attributed to the Kondo effect. In Ref. 62 and Ref. 63, the Kondo temperature of $\text{Ce}_5\text{Ni}_2\text{Si}_3$ is estimated as $T_K = 31\text{K}$.

4. $\text{Ce}_{20}\text{Ni}_{42}\text{As}_{31}$

$\text{Ce}_{20}\text{Ni}_{42}\text{As}_{31}$ ⁶⁴ has the achiral space group no. 176 ($P6_3/m$) and it could be a potential candidate for the paramagnetic Dirac-Kondo semimetal with fourfold degenerate nodal lines on the BZ boundary³⁰. $\text{Ce}_{20}\text{Ni}_{42}\text{As}_{31}$ remains paramagnetic down to 1.8K . Magnetic susceptibility measurements at high temperatures yield $\mu_{\text{eff}} = 2.55\mu_B$ and $\theta_p = -28\text{K}$. The electrical resistivity of $\text{Ce}_{20}\text{Ni}_{42}\text{As}_{31}$ does not vary significantly as a function of temperature, and the value of the electrical resistivity is about $300 \mu\Omega\text{cm}$ at room temperature. Hence, we could classify $\text{Ce}_{20}\text{Ni}_{42}\text{As}_{31}$ as having a semimetallic-type resistivity. In addition, the magnetic resistivity has $-\ln T$ behaviors in two different temperature regimes, the first one at $T > 100 \text{ K}$ and the second one at $T = 5 - 15\text{K}$.

The observed $-\ln T$ behaviors in the magnetic resistivity could suggest the presence of Kondo effect. The magnetic resistivity further shows a maximum around 53K. Finally, we note that the empirical formula of this compound is $\text{Ce}_{20}\text{Ni}_{39}\text{As}_{30}$.

5. $\text{Ce}_{20}\text{Ni}_{42}\text{P}_{30}$

$\text{Ce}_{20}\text{Ni}_{42}\text{P}_{30}$ ^{65,66} has the achiral space group no. 176 ($P6_3/m$), and within a certain temperature range it could be a potential candidate for the paramagnetic Dirac-Kondo semimetal with fourfold degenerate nodal lines on the BZ boundary³⁰. The measurements of the magnetic susceptibility yield the effective magnetic moment $\mu_{\text{eff}} = 1\mu_{\text{B}}$ and the paramagnetic Curie temperature $\theta_p = 29\text{K}$ for $T < 200\text{K}$. On the other hand, $\mu_{\text{eff}} = 2\mu_{\text{B}}$ and $\theta_p = -386\text{K}$ for $T > 200\text{K}$. In addition, a magnetic transition at 32K is observed, while the determination of the nature of the magnetic order requires further studies. This suggests that above $T = 32\text{K}$ $\text{Ce}_{20}\text{Ni}_{42}\text{P}_{30}$ is in the paramagnetic state. The measurements of the electrical resistivity reveal the potential Kondo physics of $\text{Ce}_{20}\text{Ni}_{42}\text{P}_{30}$. The Kondo temperature of $\text{Ce}_{20}\text{Ni}_{42}\text{P}_{30}$ is estimated as $T_{\text{K}} = 67\text{K}$ ⁶⁵. In addition, the experimental data of $\rho(T)$ does not change significantly as a function of temperature, indicating a semimetallic-type resistivity. The magnetic contribution $\rho_{\text{mag}}(T)$ to the resistivity $\rho(T)$ is also extracted experimentally by subtracting the $\rho(T)$ data of $\text{Sm}_{20}\text{Ni}_{42}\text{P}_{30}$ from the $\rho(T)$ data of $\text{Ce}_{20}\text{Ni}_{42}\text{P}_{30}$. In particular, $\rho_{\text{mag}}(T)$ exhibits a T^2 -behavior when $T < 32\text{K}$ and a $-\ln T$ -behavior when $T > 100\text{K}$. The $-\ln T$ -behavior of $\rho_{\text{mag}}(T)$ is consistent with the Kondo theory. Although there is a magnetic transition at $T = 32\text{K}$, we expect that between the magnetic transition temperature $T = 32\text{K}$ and the Kondo temperature $T_{\text{K}} = 67\text{K}$, $\text{Ce}_{20}\text{Ni}_{42}\text{P}_{30}$ can be a potential candidate of the Kondo-driven paramagnetic state with fourfold degenerate nodal lines on the BZ boundary.

Supplementary Note 14. OTHER CANDIDATE MATERIALS

In this section, we provide other candidate materials that have either relatively limited experimental information or experimental information that conflicts with the properties of topological Kondo semimetal phases. We provide this list of other candidate materials in the hope that it could inspire further studies on these materials. Although they might not host topological Kondo semimetal phases, their space-group symmetry could still render them interesting materials for

Other candidate material

Material	SG #	SG	T_C	T_N	Resistivity	γ
Ce-based material						
$Ce_3CuSnSe_7$	173	$P6_3$		5K	Non-metallic [Supplementary Note 15 2]	
$Ce_3Ge_{1.47}Se_7$	173	$P6_3$	\times		Possibly insulating	
$Ce_3Mg_{0.5}SiS_7$	173	$P6_3$	\times		Possibly insulating	
$Ce_{18}W_{10}O_{57}$	190	$P\bar{6}2c$	\times		Possibly insulating	
U-based material						
$Cu_2U_3S_7$	173	$P6_3$	\times			
$Cu_2U_3Se_7$	173	$P6_3$		13K		
$U_6Ni_{20}P_{13}$	176	$P6_3/m$		$41 \pm 4K$		
U_7Te_{12}	176	$P6_3/m$	$48 - 73K$		Semimetallic	$48 \text{ mJ/K}^2 \text{ mol}$
Yb-based material						
$Ba_3YbB_9O_{18}$	176	$P6_3/m$	\times		Possibly insulating	
$YbBO_3$	176	$P6_3/m$	\times		Possibly insulating	

Supplementary Table S8. Summary of the physical properties of other candidate materials $Ce_3CuSnSe_7$ ^{67,68}, $Ce_3Ge_{1.47}Se_7$ ⁶⁹, $Ce_3Mg_{0.5}SiS_7$ ⁷⁰, $Ce_{18}W_{10}O_{57}$ ⁷¹, $Cu_2U_3S_7$ ⁷², $Cu_2U_3Se_7$ ⁷², $U_6Ni_{20}P_{13}$ ^{73,74}, U_7Te_{12} ⁷⁵⁻⁷⁹. “SG” means “space group”. T_C and T_N denote the ferromagnetic and antiferromagnetic transition temperatures, respectively. A “ \times ” mark in the magnetic transition temperatures mean no magnetic order is reported. We note that for $Ce_3CuSnSe_7$ our experimental analysis in Supplementary Note 15 2 verifies the presence of magnetic transition and characterizes $Ce_3CuSnSe_7$ as a non-metallic compound. We note that for both $U_6Ni_{20}P_{13}$ and U_7Te_{12} , in addition to space group no. 176 ($P6_3/m$)^{73,75-77}, there are also studies reporting group no. 174 ($P\bar{6}$) for $U_6Ni_{20}P_{13}$ ⁷⁴ and U_7Te_{12} ^{78,79}. We have also included in this table the physical properties of $U_6Ni_{20}P_{13}$ and U_7Te_{12} present in these references^{74,78,79} reporting space group no. 174 ($P\bar{6}$). We refer readers to Supplementary Note 14 for more information on the other candidate materials.

future studies.

1. $\text{Ce}_3\text{CuSnSe}_7$

$\text{Ce}_3\text{CuSnSe}_7$ ^{67,68} has the chiral space group no. 173 ($P6_3$). From the magnetic susceptibility measurements, the effective magnetic moment $\mu_{\text{eff}} = 2.46(3)\mu_{\text{B}}$ and the paramagnetic Curie temperature $\theta_p = -18(1)\text{K}$ for $\text{Ce}_3\text{CuSnSe}_7$. The negative value of θ_p suggests that $\text{Ce}_3\text{CuSnSe}_7$ has anti-ferromagnetic coupling. The magnetic susceptibility measurements further suggest an anti-ferromagnetic transition at $T_{\text{N}} = 5\text{K}$. Due to the lack of experimental information on the specific heat and the Sommerfeld coefficient, we are not able to verify whether $\text{Ce}_3\text{CuSnSe}_7$ is a heavy-fermion compound. Also, the lack of experimental electrical resistivity in the literature makes it difficult to establish whether $\text{Ce}_3\text{CuSnSe}_7$ is a semimetal. Finally, the lack of experimental information about the above physical properties also makes it challenging to determine whether $\text{Ce}_3\text{CuSnSe}_7$ exhibits Kondo physics. Thus motivated, we perform experimental analyses on $\text{Ce}_3\text{CuSnSe}_7$ and report our results in Supplementary Note 15 2, from which we establish that $\text{Ce}_3\text{CuSnSe}_7$ is an insulator.

2. $\text{Ce}_3\text{Ge}_{1.47}\text{Se}_7$

$\text{Ce}_3\text{Ge}_{1.47}\text{Se}_7$ ⁶⁹ has the chiral space group no. 173 ($P6_3$). The measurements of magnetic susceptibility yield the effective magnetic moment $\mu_{\text{eff}} = 2.40(8)\mu_{\text{B}}/\text{Ce}$ and the paramagnetic Curie temperature $\theta_p = -12.9(7)\text{K}$. Although there is no magnetic transition in $\text{Ce}_3\text{Ge}_{1.47}\text{Se}_7$ down to 1.72K, it is highly possible that $\text{Ce}_3\text{Ge}_{1.47}\text{Se}_7$ is an insulator.

3. $\text{Ce}_3\text{Mg}_{0.5}\text{SiS}_7$

$\text{Ce}_3\text{Mg}_{0.5}\text{SiS}_7$ ⁷⁰ has the chiral space group no. 173 ($P6_3$). The measurements of magnetic susceptibility yield the effective magnetic moment $\mu_{\text{eff}} = 2.33\mu_{\text{B}}/\text{Ce}$ and the paramagnetic Curie temperature $\theta_p = -43.7\text{K}$. Although no antiferromagnetic transition is observed in $\text{Ce}_3\text{Mg}_{0.5}\text{SiS}_7$ down to 2K, it is highly possible that $\text{Ce}_3\text{Mg}_{0.5}\text{SiS}_7$ is an insulator.

4. $\text{Ce}_{18}\text{W}_{10}\text{O}_{57}$

$\text{Ce}_{18}\text{W}_{10}\text{O}_{57}$ ⁷¹ has the achiral space group no. 190 ($P\bar{6}2c$). The measurements of magnetic susceptibility yield the effective magnetic moment $\mu_{\text{eff}} = 10.73\mu_{\text{B}}/\text{formula unit}$ and the paramag-

netic Curie temperature $\theta_p = -71.14\text{K}$. Although $\text{Ce}_{18}\text{W}_{10}\text{O}_{57}$ does not order magnetically, it is highly possible that $\text{Ce}_{18}\text{W}_{10}\text{O}_{57}$ is an insulator.

5. $\text{Cu}_2\text{U}_3\text{S}_7$

$\text{Cu}_2\text{U}_3\text{S}_7$ ⁷² has the chiral space group no. 173 ($P6_3$). The measurements of magnetic susceptibility yield the effective magnetic moment $\mu_{\text{eff}} = 2.50\mu_{\text{B}}/\text{U}$ and the paramagnetic Curie temperature $\theta_p = -33\text{K}$. In addition, $\text{Cu}_2\text{U}_3\text{S}_7$ is paramagnetic down to 5K.

6. $\text{Cu}_2\text{U}_3\text{Se}_7$

$\text{Cu}_2\text{U}_3\text{Se}_7$ ⁷² has the chiral space group no. 173 ($P6_3$). The measurements of magnetic susceptibility yield the effective magnetic moment $\mu_{\text{eff}} = 2.64\mu_{\text{B}}/\text{U}$ and the paramagnetic Curie temperature $\theta_p = -28\text{K}$. In addition, $\text{Cu}_2\text{U}_3\text{Se}_7$ has an antiferromagnetic transition at $T_{\text{N}} = 13\text{K}$.

7. $\text{U}_6\text{Ni}_{20}\text{P}_{13}$

$\text{U}_6\text{Ni}_{20}\text{P}_{13}$ could crystallize in the achiral space group no. 176 ($P6_3/m$)⁷³ or the achiral space group no. 174 ($P\bar{6}$)⁷⁴. In Ref. 74 which reports space group $P\bar{6}$ for $\text{U}_6\text{Ni}_{20}\text{P}_{13}$, an antiferromagnetic transition at $T_{\text{N}} = 41 \pm 4\text{K}$ is observed, with $\mu_{\text{eff}} = 2.1 \pm 0.1\mu_{\text{B}}/\text{U}$ and $\theta_p = -37 \pm 4\text{K}$ from the magnetic susceptibility measurements.

8. U_7Te_{12}

U_7Te_{12} could crystallize in the achiral space group no. 176 ($P6_3/m$) or the achiral space group no. 174 ($P\bar{6}$). Specifically, the ICSD Collection Codes 16493, 601162, and 653139 report U_7Te_{12} as having space group $P6_3/m$, in which the corresponding journal references are Ref. 75, Ref. 76, and Ref. 77, respectively. On the other hand, Ref. 78 and Ref. 79 report U_7Te_{12} as having space group $P\bar{6}$. In Ref. 77, a ferromagnetic transition at $T = 73\text{K}$ is reported for U_7Te_{12} . Also, in Ref. 78, U_7Te_{12} is reported to have a ferromagnetic transition at $T = 54\text{K}$ and a semimetallic behavior. Such a semimetallic behavior in Ref. 78 could be deduced from $\rho(T = 77\text{K}) = 3.3 \times 10^{-3} \Omega\text{cm}$ and $\rho(T = 300\text{K}) = 3.5 \times 10^{-3} \Omega\text{cm}$, leading to $\frac{\rho(T=300\text{K})}{\rho(T=77\text{K})} \approx 1.06$. Finally, Ref. 79 reports a ferromagnetic transition at $T = 48\text{K}$, a semimetallic behavior, and the Sommerfeld

coefficient $\gamma = 48 \text{ mJ/K}^2 \text{ mol}$ for U_7Te_{12} . The Sommerfeld coefficient in Ref. 79 is determined using the specific-heat data below $T = 10\text{K}$.

9. $\text{Ba}_3\text{YbB}_9\text{O}_{18}$

$\text{Ba}_3\text{YbB}_9\text{O}_{18}$ ⁸⁰ has the achiral space group no. 176 ($P6_3/m$). The measurements of magnetic susceptibility yield the effective magnetic moment $\mu_{\text{eff}} = 4.73\mu_{\text{B}}$ and the paramagnetic Curie temperature $\theta_p = -90\text{K}$ in the temperature range $100 - 340\text{K}$. On the other hand, in the temperature range $5 - 10\text{K}$, $\mu_{\text{eff}} = 2.32\mu_{\text{B}}$ and $\theta_p = -0.12 \pm 0.02\text{K}$. Although there is no magnetic order in $\text{Ba}_3\text{YbB}_9\text{O}_{18}$ down to 1.9K , it is highly possible that $\text{Ba}_3\text{YbB}_9\text{O}_{18}$ is an insulator.

10. YbBO_3

YbBO_3 ⁸¹ has the achiral space group no. 176 ($P6_3/m$). The measurements of magnetic susceptibility yield the effective magnetic moment $\mu_{\text{eff}} = 4.53\mu_{\text{B}}$ and the paramagnetic Curie temperature $\theta_p = -62.6\text{K}$ in the temperature range above 150K . On the other hand, $\mu_{\text{eff}} = 3.2\mu_{\text{B}}$ and $\theta_p = -0.8\text{K}$ in the temperature range below 50K . Although there is no signature of magnetic order observed in YbBO_3 down to 0.4K , it is highly possible that YbBO_3 is an insulator.

Supplementary Note 15. NEW EXPERIMENTS ON CANDIDATE MATERIALS

Motivated by the experimental information on the candidate materials discussed in Supplementary Note 12, Supplementary Note 13, and Supplementary Note 14, we carried out crystal growth for selected compounds. We successfully synthesized pure phase Ce_2NiGe_3 and $\text{Ce}_3\text{CuSnSe}_7$, while attempts on $\text{Ce}_6\text{Co}_{2-\delta}\text{Si}_3$ ($\delta = 0.33$) and $\text{Ce}_6\text{Rh}_{32}\text{P}_{17}$ resulted only in samples with mixture of phases. Physical measurements were performed on the successfully synthesized phase-pure crystals. Specifically, we performed magnetization, specific heat, and electrical resistivity measurements between room temperatures and 1.8 K and in magnetic fields up to 9 T , using a Physical Property Measurement System (PPMS) by Quantum Design.

1. Ce₂NiGe₃

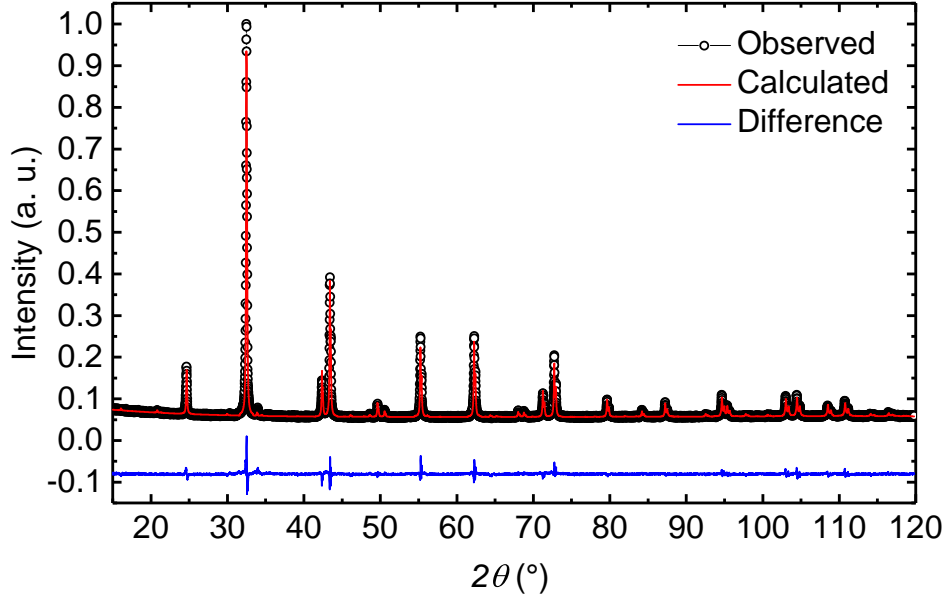
Motivated by the experimental information of Ce₂NiGe₃ from the literature in Supplementary Note 124, we synthesized polycrystalline samples of Ce₂NiGe₃ in order to study its physical properties. Earlier reports on the crystal structure of Ce₂NiGe₃ suggested that this compound crystallizes in the AlB₂ type structure (space group no. 191, $P6/mmm$)⁴². However, neutron diffraction studies on polycrystalline samples showed a better agreement with the Er₂RhSi₃ type structure (space group no. 190, $P\bar{6}2c$)³⁹, which is in agreement with the Rietveld refinement analysis of the powder X-ray diffraction (XRD) patterns of our samples, as seen in Supplementary Fig. S24. In Supplementary Fig. S25, we show the measured magnetic susceptibility of Ce₂NiGe₃, which confirms that there is a magnetic transition around 3.5K, consistent with Ref. 39. The magnetic susceptibility data are consistent with the Curie-Weiss behavior with a negative paramagnetic Curie temperature of $\theta_p = -7.8$ K, suggesting antiferromagnetic correlations and an effective moment $\mu_{\text{eff}} = 2.6\mu_B$ close to the full Ce³⁺ moment. We further perform more characterizations of Ce₂NiGe₃ and present our results in Supplementary Fig. S26. Our measurements on the electrical resistivity [Supplementary Fig. S26(a)] is consistent with Ref. 42, verifying that Ce₂NiGe₃ has a semimetallic-type resistivity. Our results on the magnetization [Supplementary Fig. S26(b)] and specific heat [Supplementary Fig. S26(c)] of Ce₂NiGe₃ are also consistent with the literature^{39,42}.

We now describe new experimental results for Ce₂NiGe₃. We begin with the magnetoresistivity, which is the longitudinal resistivity in the presence of an applied magnetic field. As shown in Supplementary Fig. S26(d), the magnetoresistivity of Ce₂NiGe₃ exhibits the qualitative behavior of a Kondo system^{14,61}.

The Hall resistivity of Ce₂NiGe₃ is linear-in-field at low fields, but tends to saturate at larger fields [Supplementary Fig. S26(e)]. Similar behavior is observed for the magnetization [Supplementary Fig. S26(b)], suggestive of an anomalous contribution to the Hall resistivity⁸²

$$\rho_{xy} = \rho_{xy}^N(B) + \rho_{xy}^A(M) = R_0 B + R_S \mu_0 M, \quad (\text{S59})$$

where ρ_{xy}^N and ρ_{xy}^A are the normal and anomalous components, R_0 and R_S are the normal and anomalous Hall coefficients, B is the applied magnetic field, and M is the magnetization. From ρ_{xy}^N , we estimate a carrier density of $n = 1/(eR_0) = 2.16 \times 10^{20} \text{ cm}^{-3}$ for Ce₂NiGe₃ at 2 K using a single-band model. The corresponding carrier densities at different temperatures are shown in Supplementary Fig. S26(f). The low carrier density extracted from Hall measurement also confirms its semimetallicity.



Supplementary Fig. S24. Powder XRD pattern for a Ce_2NiGe_3 sample. The open circles are the experimental data, the red curve is obtained from the Rietveld refinement for the Er_2RhSi_3 type structure (space group no. 190, $P\bar{6}2c$), and the blue curve is the difference between the experimental data and the Rietveld refinement.

Finally, we present our results on the anomalous Hall conductivity σ_{AHE} expressed as

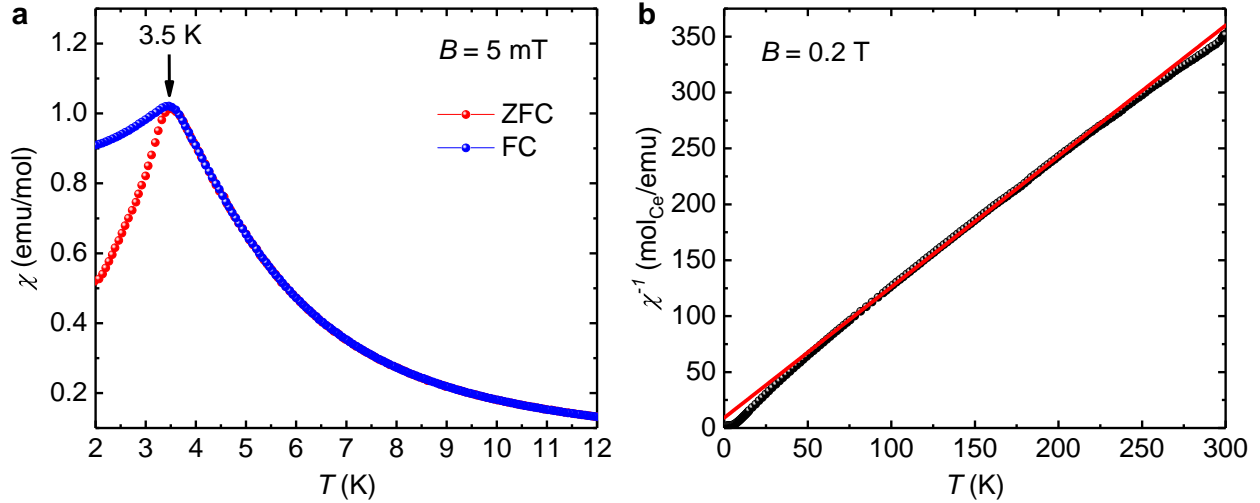
$$\sigma_{\text{AHE}} = \frac{\rho_{xy}^A}{(\rho_{xx})^2 + (\rho_{xy}^A)^2}. \quad (\text{S60})$$

From ρ_{xx} and ρ_{xy} [Supplementary Fig. S26(d,e)] we estimate that the anomalous Hall conductivity σ_{AHE} for Ce_2NiGe_3 reaches maximum values of the order of $10^2 \Omega^{-1}\text{cm}^{-1}$, while the longitudinal conductivity σ_{xx} is of the order $10^3 \Omega^{-1}\text{cm}^{-1}$ between 2 K and 10 K, suggesting a dominating intrinsic contribution to the anomalous Hall effect [Supplementary Fig. S27].

2. $\text{Ce}_3\text{CuSnSe}_7$

We synthesized polycrystalline samples of $\text{Ce}_3\text{CuSnSe}_7$ in order to study its physical properties. In Supplementary Fig. S28, we show our powder XRD analysis on $\text{Ce}_3\text{CuSnSe}_7$, which confirms that the crystal structure of our $\text{Ce}_3\text{CuSnSe}_7$ sample belongs to the chiral space group no. 173 ($P6_3$).

Previous magnetic susceptibility studies of $\text{Ce}_3\text{CuSnSe}_7$ revealed a sharp anomaly around 5 K

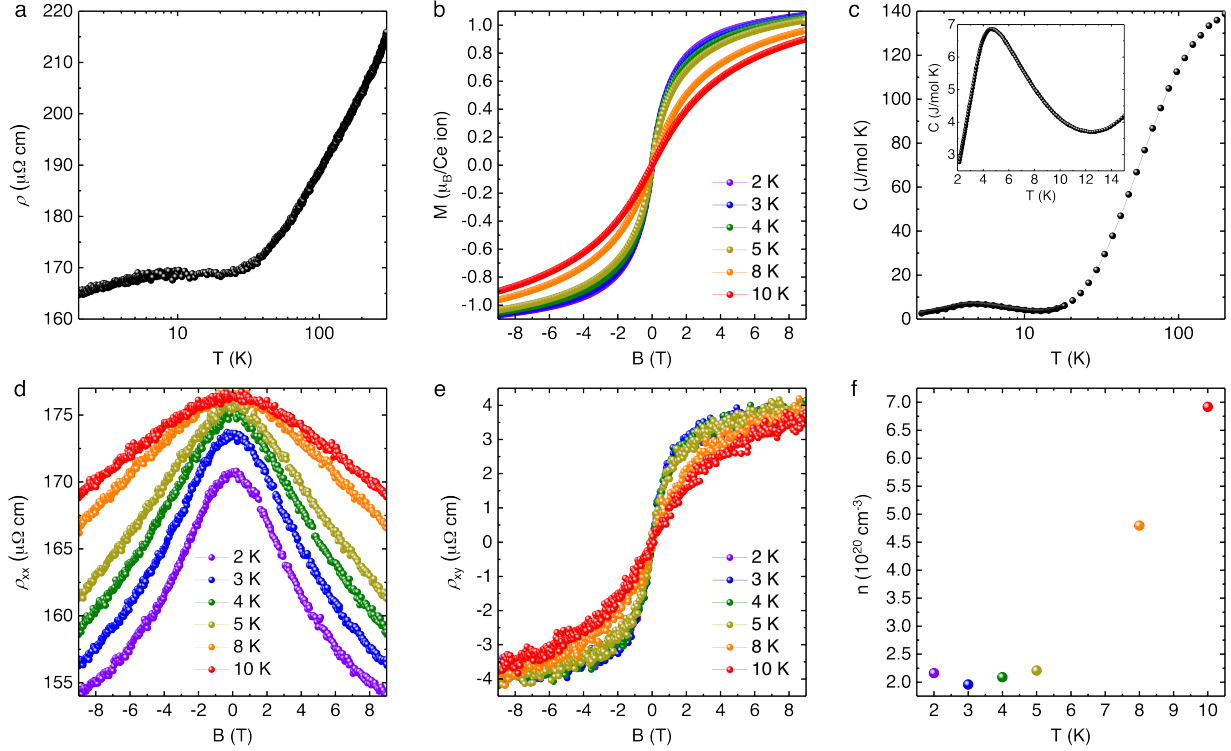


Supplementary Fig. S25. (a) Zero-field cooling (ZFC) and field cooling (FC) magnetic susceptibility curves of Ce_2NiGe_3 measured in a field of 5 mT. (b) Temperature dependence of χ^{-1} measured at 0.2 T and Curie-Weiss fits (red line).

and an upturn at lower temperatures, which was interpreted as evidence for antiferromagnetic order at 5 K and a more complex form of magnetism at lower temperatures⁶⁸. Our magnetic susceptibility data on $\text{Ce}_3\text{CuSnSe}_7$ also show an anomaly around 5 K and an upturn at lower temperatures [Supplementary Fig. S29], consistent with the above. At high temperatures, the data exhibit Curie-Weiss behavior, with a negative paramagnetic Curie temperature of $\theta_p = -45$ K suggestive of antiferromagnetic correlations and an effective moment of $\mu_{\text{eff}} = 2.8\mu_B$, which is not too different from a full Ce^{3+} moment.

The electrical resistivity of $\text{Ce}_3\text{CuSnSe}_7$ increases with decreasing temperature [Supplementary Fig. S30], evidencing a non-metallic state. Between 300 K and 150 K, the data are consistent with the Arrhenius law $\rho(T) = \rho_0 \exp(E_G/k_B T)$, with a band gap of $E_G = 0.57$ eV. A band gap of the same order, $E_G = 0.49$ eV, was found for a related $P6_3$ space group quaternary compound, $\text{La}_3\text{Fe}_{0.61}\text{SnSe}_7$ ⁹². For temperatures below 90 K, the resistivity is well described by the Mott variable range hopping (VRH) model, which is suitable for describing disordered semiconductors^{93–95}.

As we aim to find hexagonal Weyl-Kondo semimetal candidate materials, further investigations of the non-metallic compound $\text{Ce}_3\text{CuSnSe}_7$ are beyond the scope of this work. In general, future studies should address the complex magnetic behavior at lower temperatures and its relation to the VRH behavior of the electrical resistivity. Several reports of quaternary $R_3MM'X_7$ (R = rare earth, M and M' = metal or semimetal, and X = S, Se) compounds of space group $P6_3$



Supplementary Fig. S26. Physical properties of Ce_2NiGe_3 . (a) Temperature dependence of electrical resistivity. (b), (d), (e): Applied magnetic field dependence of magnetization, longitudinal resistivity, and Hall resistivity at different temperatures. (c) Temperature dependence of specific heat. (f) Temperature dependence of carrier density estimated from the linear portion of the curves in panel (e).

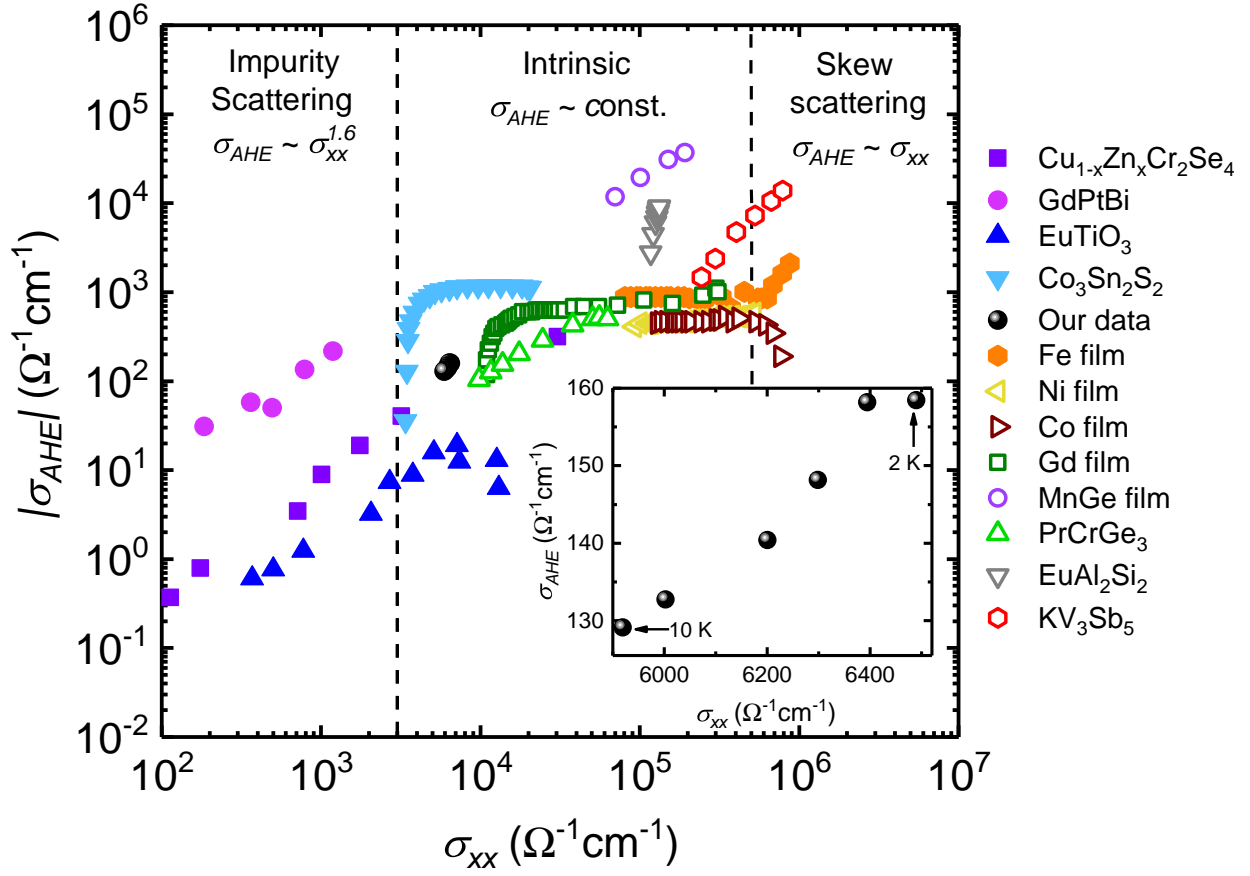
discuss partial occupancy of the M and M' sites, with implications for magnetic and electric properties^{92,96–101}.

Supplementary Note 16. GEOMETRIC FRUSTRATION IN HEXAGONAL CRYSTALS

We now explore the geometric frustration in our candidate materials. For example, in the lattice structure, the presence of triangular plaquettes promotes geometric frustration when the interactions are antiferromagnetic.

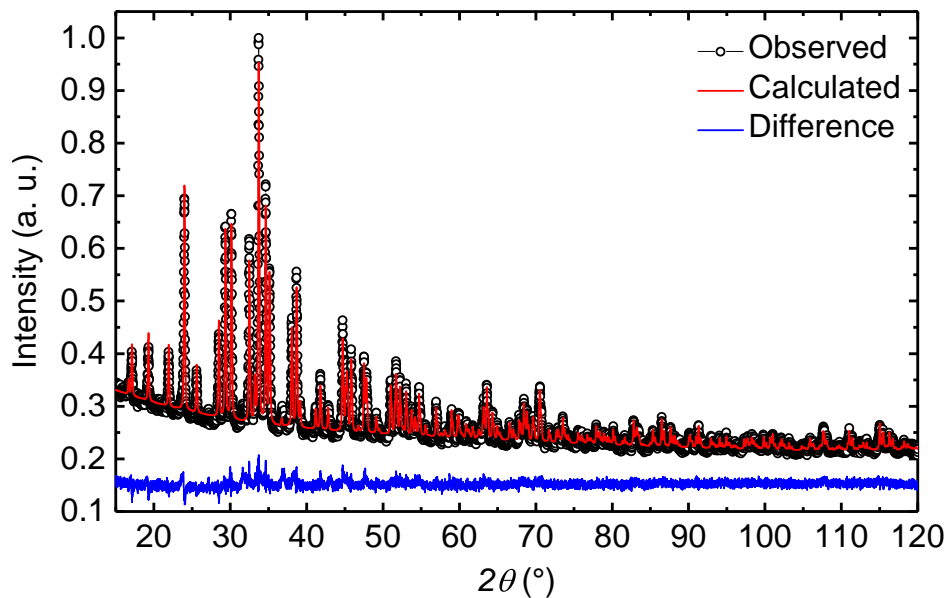
For CePt_2B , as shown in Supplementary Fig. S31(a,b), its Ce ions form a three-dimensional kagome-like lattice structure, where the abundance of triangular plaquettes indicates geometric frustration.

For Ce_2NiGe_3 , as shown in Supplementary Fig. S31(c,d), its Ce ions form a nearly-ideal kagome lattice structure, suggesting the presence of geometric frustration.

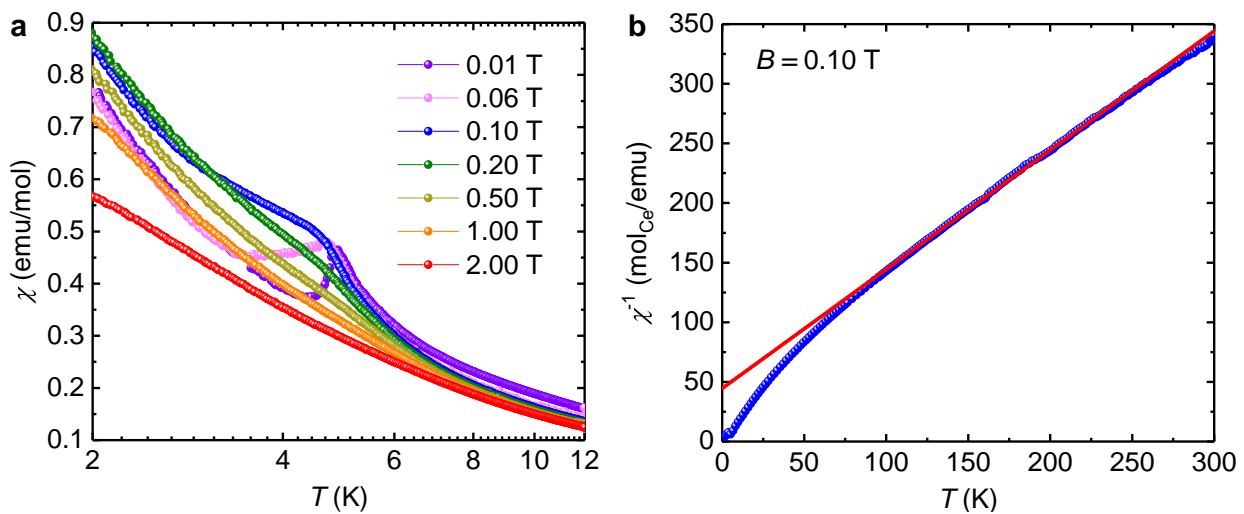


Supplementary Fig. S27. $|\sigma_{\text{AHE}}|$ versus σ_{xx} for literature data⁸³⁻⁹¹, including experimental results for Ce_2NiGe_3 from Eq. (S60), ρ_{xx} and ρ_{xy} curves [Supplementary Fig. S26(d-e)] from 2 K to 10 K. Inset: Magnified view of σ_{AHE} versus σ_{xx} , detailing the portion with our data points. The value of σ_{AHE} decreases monotonically with increasing temperature from 2 K to 10 K.

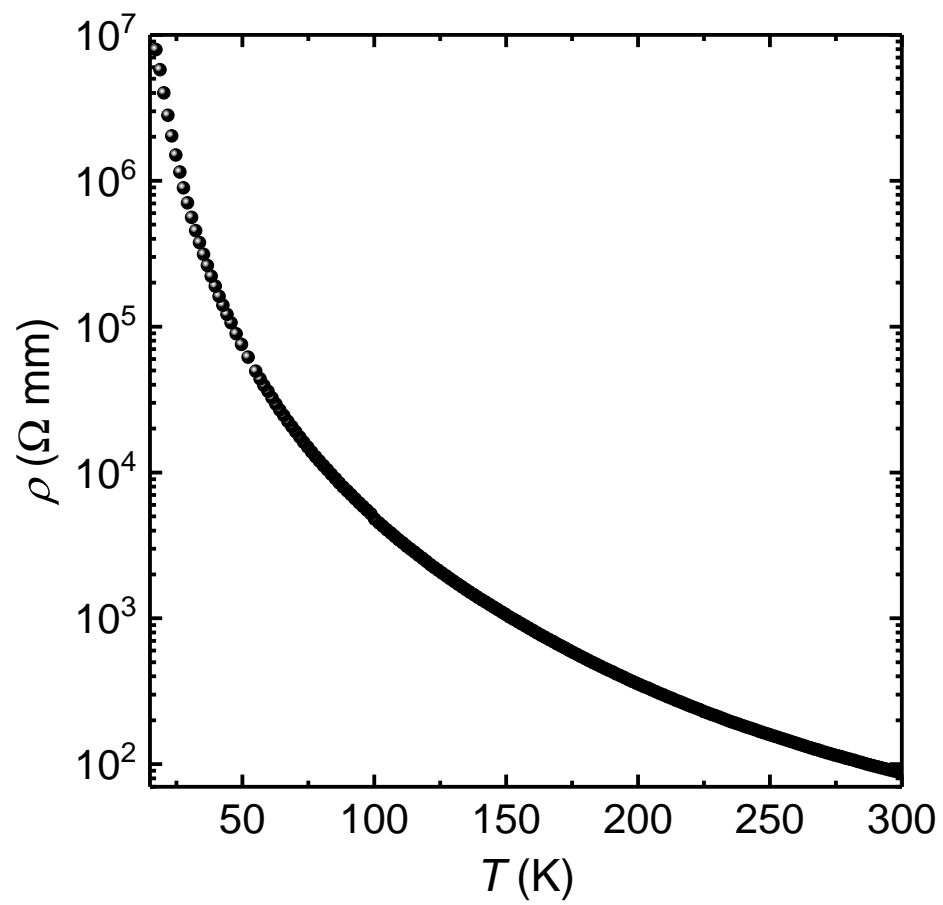
For $\text{Ce}_6\text{Co}_{2-\delta}\text{Si}_3$ with $\delta = 0.33$, namely $\text{Ce}_6\text{Co}_{1.67}\text{Si}_3$, as shown in Supplementary Fig. S31(e,f), its Ce ions form a lattice structure with abundant triangular plaquettes, suggesting geometric frustration.



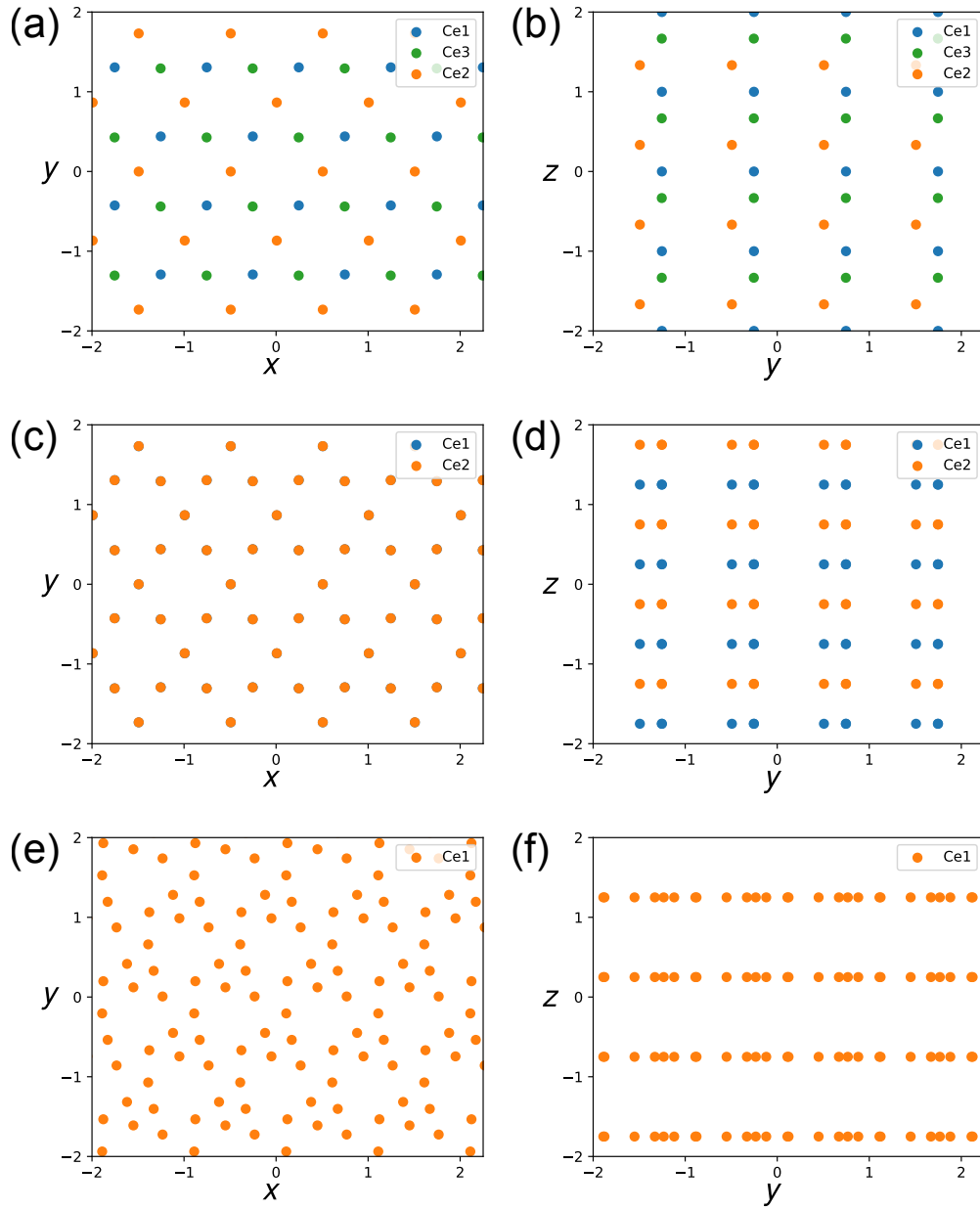
Supplementary Fig. S28. Powder XRD pattern for a $\text{Ce}_3\text{CuSnSe}_7$ sample. The open circles are the experimental data, the red curve is obtained from the Rietveld refinement, and the blue curve is the difference between the experimental data and the Rietveld refinement.



Supplementary Fig. S29. (a) Zero-field cooling (ZFC) magnetic susceptibility curves of $\text{Ce}_3\text{CuSnSe}_7$ measured in different magnetic fields. (b) Temperature dependence of χ^{-1} measured at 0.1 T and a Curie-Weiss fit (red line).



Supplementary Fig. S30. Temperature dependence of the electrical resistivity of $\text{Ce}_3\text{CuSnSe}_7$.



Supplementary Fig. S31. (a) Top view (along c -axis) of Ce sites in CePt_2B . (b) Side view (along a -axis) of Ce sites in CePt_2B . (c) Top view (along c -axis) of Ce sites in Ce_2NiGe_3 . (d) Side view (along a -axis) of Ce sites in Ce_2NiGe_3 . (e) Top view (along c -axis) of Ce sites in $\text{Ce}_6\text{Co}_{2-\delta}\text{Si}_3$ with $\delta = 0.33$. (f) Side view (along a -axis) of Ce sites in $\text{Ce}_6\text{Co}_{2-\delta}\text{Si}_3$ with $\delta = 0.33$. In these plots color represents different z -coordinates in the unit cell.